

UNIVERSITÉ DE GENÈVE
Département de Physique
de la Matière Condensée

FACULTÉ DES SCIENCES
Professeur D. van der Marel

Title

THÈSE

*présenté à la Faculté des Sciences de l'Université de Genève
pour obtenir le grade de docteur ès Sciences, mention physique*

par

Seyed Iman Mirzaei

de

Tehran (Iran)

Thèse n° XXXX

GENÈVE

Atelier de reproduction de la Section de Physique

2013

1. Reviewer: Name

2. Reviewer:

Day of the defense:

Signature from head of PhD committee:

Abstract

Acknowledgements

Contents

1	Theory	1
1.1	Light-matter interaction	1
1.1.1	Fresnel equations	6
1.2	Kramers-Kronig relations	7
1.3	Drude model of metals	10
1.3.1	Hagen-Rubens approximation	11
1.3.2	Drude-Lorentz model	11
1.4	Extended Drude model	12
1.5	Kubo formula	13
1.6	Fermi liquid	15
1.6.1	Memory function of a local Fermi liquid	15
2	Experimental	17
2.1	Introduction	17
2.2	Sample preparation	18
2.3	Optical measurements	19
2.3.1	Reflectivity	19
2.3.1.1	Optical setup	19
2.3.1.2	Optical cryostat	20
2.3.1.3	Reference measurement	20
2.3.1.4	Polarizer	21
2.3.1.5	Drift Corrections	21
2.3.2	Ellipsometry	26
2.3.2.1	Window and lens corrections (Ellipsometry)	28

CONTENTS

2.3.2.2	C-axis corrections	28
2.4	Data analysis	30
2.4.1	Optical conductivity	30
2.4.2	Extended Drude analysis	32
3	Optical properties of Iron pnictides	33
3.1	Introduction	33
3.2	Optical Properties of $\text{SmO}_{1-x}\text{F}_x\text{FeAs}$	34
3.3	Optical Properties of $\text{SrFe}_{2-x}\text{Co}_x\text{As}_2$	40
3.3.1	Sample Preparation	40
3.3.2	Optical measurements	41
3.3.2.1	Reflectivity	41
3.3.2.2	Drift Corrections	41
3.3.2.3	Ellipsometry	42
3.3.3	Data analysis	42
3.3.3.1	Complex optical constants	42
3.3.3.2	Extended Drude analysis	43
3.3.4	Comparing 122 family of pnictides and 11 family of chalcogenides	44
3.4	Quantum Criticality in $\text{SrFe}_{2-x}\text{Co}_x\text{As}_2$	46
3.4.1	Introduction	46
3.4.2	Quantum criticality	48
3.4.3	The case of 122 family	49
4	Optical properties of under-doped $\text{HgBa}_2\text{CuO}_{4+\delta}$	51
4.1	Introduction	51
4.2	Sample preparation	51
4.3	Optical measurements	53
4.3.1	Reflectivity	53
4.3.2	Ellipsometry	54
4.4	Drude-Lorentz analysis	55
4.5	Conduction band and bound charge contributions	56
4.6	Sheet conductance and spectral weight	58
4.6.1	High-energy spectral weight in superconducting state	61
4.7	Comparison with DC resistivity	62

4.8	Extended Drude analysis	64
5	Fermi-liquid behavior in under-doped cuprates	69
5.1	Introduction	69
5.2	Optical signatures of Fermi-liquid behavior in HgBa ₂ CuO _{4+δ}	70
6	Optical Data Analysis Using Strong Coupling Formalism	75
6.1	Introduction	75
6.2	Improvement in numerical calculations	77
6.3	Analysis of under-doped HgBa ₂ CuO _{4+δ}	80
6.4	Fermi-liquid susceptibility: A minimal model	81
6.5	Discussion	88
	Bibliography	91

Theory

1.1 Light-matter interaction

In this section, a short review of the most important concepts in electrodynamics of solids is presented. The text will closely follow the notations and concepts presented in chapter two of reference [1]. The units used in this chapter are the Gaussian (CGS) units.

All what we learn from the material properties through optical methods is based on our understanding of how light (or electromagnetic field) interacts with matter. We start the discussion with an overview of the general rules governing the electromagnetic waves in vacuum and then we will see how the presence of matter will affect those rules.

The character of light in vacuum can be -in general- formulated by four equations known as Maxwell's equations:

$$\nabla \times \mathbf{E}(\mathbf{r}, t) = -\frac{1}{c} \frac{\partial \mathbf{B}(\mathbf{r}, t)}{\partial t} \quad (1.1a)$$

$$\nabla \cdot \mathbf{B}(\mathbf{r}, t) = 0 \quad (1.1b)$$

$$\nabla \times \mathbf{B}(\mathbf{r}, t) = \frac{1}{c} \frac{\partial \mathbf{E}(\mathbf{r}, t)}{\partial t} + \frac{4\pi}{c} \mathbf{J}(\mathbf{r}, t) \quad (1.1c)$$

$$\nabla \cdot \mathbf{E}(\mathbf{r}, t) = 4\pi\rho(\mathbf{r}, t) \quad (1.1d)$$

With \mathbf{E} and \mathbf{B} being the electric and magnetic field vectors. $c = 2.99792458 \times 10^8 m s^{-1}$ is the speed of light in vacuum. \mathbf{J} and ρ are the current density and charge density.

1. THEORY

Since we are mostly interested in optical parameters expressed in the frequency and momentum domain, we write the Fourier transform of the Maxwell's equations for future reference:

$$\mathbf{q} \times \mathbf{E}(\mathbf{q}, \omega) = \frac{\omega}{c} \mathbf{B}(\mathbf{q}, \omega) \quad (1.2a)$$

$$\mathbf{q} \cdot \mathbf{B}(\mathbf{q}, \omega) = 0 \quad (1.2b)$$

$$i\mathbf{q} \times \mathbf{B}(\mathbf{q}, \omega) = -i\frac{\omega}{c} \mathbf{E}(\mathbf{q}, \omega) + \frac{4\pi}{c} \mathbf{J}(\mathbf{q}, \omega) \quad (1.2c)$$

$$i\mathbf{q} \cdot \mathbf{E}(\mathbf{q}, \omega) = 4\pi\rho(\mathbf{q}, \omega) \quad (1.2d)$$

In free space where the matter is absent and no current and charge are found ($\mathbf{J} = 0$ and $\rho = 0$), the maxwell equations lead to the general form of harmonic waves:

$$\mathbf{E}(\mathbf{r}, t) = \mathbf{E}_0 \exp(i(\mathbf{q} \cdot \mathbf{r} - \omega t)) \quad (1.3a)$$

$$\mathbf{B}(\mathbf{r}, t) = \mathbf{B}_0 \exp(i(\mathbf{q} \cdot \mathbf{r} - \omega t)) \quad (1.3b)$$

In presence of matter, the electric and magnetic components of light may induce electric dipoles, magnetic moments, currents and charges. We assume homogeneous field inside the matter keeping in mind that this is not true for wavelengths smaller than or on the order of lattice parameters.

The total charge and current density in the Maxwell equations is usually subdivided in external and internal components:

$$\rho_{total} = \rho_{ext} + \rho_{int} \quad (1.4)$$

$$J_{total} = J_{ext} + J_{int}$$

where the external component represents an external source and therefore has zero value inside the sample. Again, with the assumption of large enough wavelengths, we can consider the polarization charge as zero.

The total current can be divided into three parts: the free-carrier current \mathbf{J}_{cond} which results from the free-electron response to the electric component of light, the bound charge current \mathbf{J}_{bound} that is generated through time-dependent polarization $\frac{\partial P}{\partial t}$

and the magnetization rotation $\nabla \times \mathbf{M}$:

$$\begin{aligned}\mathbf{J}_{total} &= \mathbf{J}_{cond} + \mathbf{J}_{bound} + \mathbf{J}_{ext} \\ &= \mathbf{J}_{cond} + \frac{\partial \mathbf{P}}{\partial t} + c\nabla \times \mathbf{M} + \mathbf{J}_{ext}\end{aligned}\tag{1.5}$$

Here, we introduce new fields called the electric displacement \mathbf{D} and magnetic field strength \mathbf{H} through:

$$\mathbf{D} = \epsilon_1 \mathbf{E} = (1 + 4\pi\chi_e)\mathbf{E} = \mathbf{E} + 4\pi\mathbf{P}\tag{1.6}$$

$$\mathbf{B} = \mu_1 \mathbf{H} = (1 + 4\pi\chi_m)\mathbf{H} = \mathbf{H} + 4\pi\mathbf{M}\tag{1.7}$$

with ϵ_1 being the dielectric constant (permittivity), χ_e the dielectric susceptibility and $\mathbf{P} = \chi_e \mathbf{E}$ the dipole polarization density. Similarly for magnetic field, we have μ_1 as magnetic permeability, χ_m the magnetic susceptibility and $\mathbf{M} = \chi_m \mathbf{H}$ the magnetization.

In the case of non-magnetic materials, we assume $\mu_1 = 1$ which means we neglect the magnetic susceptibility in these materials and only study the dielectric component.

We assume that there are no external currents inside the sample ($\mathbf{J}_{ext} = 0$) and that there is no external charge ($\rho_{ext} = 0$). By neglecting the polarization charge and assuming the current participation as in equation 1.5, we re-write the Maxwell equations 1.1c and 1.1d in presence of matter for the new fields:

$$\nabla \times \mathbf{H}(\mathbf{r}, t) = \frac{1}{c} \frac{\partial \mathbf{D}(\mathbf{r}, t)}{\partial t} + \frac{4\pi}{c} \mathbf{J}_{cond}(\mathbf{r}, t)\tag{1.8a}$$

$$\nabla \cdot \mathbf{D}(\mathbf{r}, t) = 4\pi\rho_{ext}(\mathbf{r}, t) = 0\tag{1.8b}$$

For harmonic waves (eqs.1.3) we can write the Maxwell's equations in the momentum and frequency domain:

$$i\mathbf{q} \times \mathbf{H}(\mathbf{q}, \omega) = -i\frac{\omega}{c}\mathbf{D}(\mathbf{q}, \omega) + \frac{4\pi}{c}\mathbf{J}_{cond}(\mathbf{q}, \omega)\tag{1.9a}$$

$$i\mathbf{q} \cdot \mathbf{D}(\mathbf{q}, \omega) = 4\pi\rho_{ext}(\mathbf{q}, \omega) = 0\tag{1.9b}$$

Before going further, we should note that we are working within the linear response assumption which means that the response functions do not depend on the field

1. THEORY

strength:

$$\mathbf{J} = \sigma \mathbf{E} \quad (1.10)$$

$$\mathbf{P} = \chi_e \mathbf{E} \quad (1.11)$$

$$\mathbf{M} = \chi_m \mathbf{H} \quad (1.12)$$

Since the electric field is assumed to have harmonic time dependence (eq.1.3a) and we work in the linear response regime, we can write:

$$\frac{\partial \mathbf{D}}{\partial t} = -i\omega \mathbf{D} \quad (1.13)$$

Which lets the equation 1.8a to be written as:

$$c\nabla \times \mathbf{H} = -i\omega\epsilon_1 \mathbf{E} + 4\pi\sigma_1 \mathbf{E} = -i\omega\hat{\epsilon} \mathbf{E} \quad (1.14)$$

Where the complex dielectric constant $\hat{\epsilon}$ is defined as:

$$\hat{\epsilon} = \epsilon_1 + i\epsilon_2 = \epsilon_1 + i\frac{4\pi\sigma_1}{\omega} \quad (1.15)$$

We also define the complex conductivity $\hat{\sigma}$ as:

$$\mathbf{J}_{tot} = \hat{\sigma} \mathbf{E} \quad (1.16)$$

Where $\hat{\sigma} = \sigma_1 + i\sigma_2$ is related to dielectric constant $\hat{\epsilon}$ through:

$$\hat{\epsilon} = 1 + \frac{4\pi i}{\omega} \hat{\sigma} \quad (1.17)$$

It is important to note that the dielectric constant presented in equation 1.6 is more than just a constant and is, in fact, a response function to the applied electric field that depends on any two positions and times:

$$\mathbf{D}(\mathbf{r}, t) = \int \int_{-\infty}^{\infty} \epsilon_1(\mathbf{r}, \mathbf{r}', t, t') \mathbf{E}(\mathbf{r}', t') dt' dr' \quad (1.18)$$

Further simplification to this equation is made based on the following assumptions: First of all, it is the difference in time that matters. Second, we assume a local approximation for our response function ϵ_1 . The arguments above imply that the dielectric

1.1 Light-matter interaction

function can be written as:

$$\epsilon_1(\mathbf{r}, \mathbf{r}', t, t') = \delta(\mathbf{r} - \mathbf{r}')\epsilon(t - t') \quad (1.19)$$

Also the integral higher limit can be reduced from infinity to t because ϵ_1 is a casual response function. We can now write the equation 1.18 in a simpler form of:

$$\mathbf{D}(t) = \int \int_{-\infty}^t \epsilon_1(t - t')\mathbf{E}(\mathbf{r}', t')dt' dr' \quad (1.20)$$

Before going further, and for sake of simplicity, we assume that we will be dealing with isotropic and homogeneous materials where no magnetic effect is present ($\mu_1 = 0$) and optical effects are linear. We will write the wave equation inside matter using the Maxwell's equations in presence of matter (eqs.1.8a and 1.8b). We describe the electric and magnetic components of light using sinusoidal wave equations of the following form:

$$\mathbf{E}(\mathbf{r}, t) = \mathbf{E}_0 \exp(i(\mathbf{q} \cdot \mathbf{r} - \omega t)) \quad (1.21)$$

$$\mathbf{H}(\mathbf{r}, t) = \mathbf{H}_0 \exp(i(\mathbf{q} \cdot \mathbf{r} - \omega t - \phi)) \quad (1.22)$$

Where \mathbf{q} is the wave-vector, ω is the frequency and ϕ is a phase factor allowing the magnetic and electric components to be out of phase.

Under above-mentioned assumptions, we will try to get an intuition about the effect of material characteristics parameters (μ_1 , ϵ_1 and σ_1) on the solution of Maxwell's equations in presence of matter. By applying the curl operator on Faraday's law (eq.1.1a) and using the identity $\nabla \times \nabla \times A = \nabla(\nabla \cdot A) - \nabla^2 A$ we get:

$$\frac{1}{c} \frac{\partial}{\partial t} (\nabla \times \mathbf{B}) = \nabla^2 \mathbf{E} - \nabla \left(\frac{4\pi\rho_{ext}}{\epsilon_1} \right) \quad (1.23)$$

Also by substituting the material parameters (equations 1.10-1.12) in Ampere's law (eq.1.8a) we get:

$$\nabla \times \mathbf{B} = \left(\frac{\epsilon_1\mu_1}{c} \right) \frac{\partial}{\partial t} \mathbf{E} + \left(\frac{4\pi\epsilon_1\sigma_1}{c} \right) \mathbf{E} \quad (1.24)$$

Now substituting the right hand side of equation 1.24 by the left hand side of equation 1.23 and assuming no net charge ($\rho_{ext} = 0$) we arrive at the wave equation of

1. THEORY

electric field inside matter:

$$\nabla^2 \mathbf{E} - \frac{\epsilon_1 \mu_1}{c^2} \frac{\partial^2}{\partial t^2} \mathbf{E} - \frac{4\pi \mu_1 \sigma_1}{c^2} \frac{\partial}{\partial t} \mathbf{E} = 0 \quad (1.25)$$

In a similar manner, we can derive the wave equation for the magnetic field strength inside matter:

$$\nabla^2 \mathbf{H} - \frac{\epsilon_1 \mu_1}{c^2} \frac{\partial^2}{\partial t^2} \mathbf{H} - \frac{4\pi \mu_1 \sigma_1}{c^2} \frac{\partial}{\partial t} \mathbf{H} = 0 \quad (1.26)$$

If we substitute a monochromatic wave (eq.1.21) in the wave equation for electric field (eq.1.25), we arrive at the following equation for the wave-vector \mathbf{q} :

$$\mathbf{q} = \frac{\omega}{c} \left[\epsilon_1 \mu_1 + i \frac{4\pi \mu_1 \sigma_1}{\omega} \right]^{1/2} \mathbf{n}_q \quad (1.27)$$

with \mathbf{n}_q being the unit vector of the wave-vector \mathbf{q} .

A few implications of the derived equations are mentioned below:

1. From Helmholtz theorem and equation $\mu_1 \nabla \cdot \mathbf{H} = 0$ we infer that \mathbf{H} only has transverse components.
2. Equation 1.27 indicates that if the medium is dissipative ($\sigma_1 \neq 0$) the wave-vector will be complex and a phase shift between \mathbf{E} and \mathbf{H} will occur.
3. In case of non-dissipative medium $\sigma_1 = 0$, the solutions will be harmonic and similar to the waves in vacuum with the only difference in coefficient that define the wave vectors (or wave-lengths). In this case, both electric and magnetic components will be perpendicular to the wave-vector which means both are transverse waves.

Finally, we define the refractive index as:

$$\hat{N} = n + ik = \sqrt{\hat{\epsilon} \mu_1} \quad (1.28)$$

1.1.1 Fresnel equations

The light at the interface of a material gets either transmitted or reflected. The electric and magnetic components of light have to be continuous at the boundary of material which impose certain boundary conditions on the wave-vectors. These conditions,

1.2 Kramers-Kronig relations

together with Snell's law of refraction $\hat{N} = \frac{\sin(\theta_i)}{\sin(\theta_t)}$ enable us to derive the Fresnel equations which describe reflection of light for two particular polarizations of incident light: S-polarization which is when the electric component of the incident light is perpendicular to the plane of incidence and P-polarization for the electric component parallel to the plane of incidence.

$$\hat{r}_p = \frac{E_{0r}}{E_{0i}} = \frac{\hat{N}^2 \cos(\theta_i) - \mu_1 \sqrt{\hat{N}^2 - \sin^2(\theta_i)}}{\hat{N}^2 \cos(\theta_i) + \mu_1 \sqrt{\hat{N}^2 - \sin^2(\theta_i)}} \quad (1.29a)$$

$$\hat{r}_s = \frac{E_{0r}}{E_{0i}} = \frac{\mu_1 \cos(\theta_i) - \sqrt{\hat{N}^2 - \sin^2(\theta_i)}}{\mu_1 \cos(\theta_i) + \sqrt{\hat{N}^2 - \sin^2(\theta_i)}} \quad (1.29b)$$

Where \hat{N}^2 is the complex index of refraction, θ_1 is the angle of incidence and μ_1 is the magnetic permeability that is usually assumed to be one. In these equations the light is assumed to enter the matter from vacuum. The Fresnel equations are used in ellipsometry to obtain the complex optical parameters of the reflected light that is measured as a function of polarization.

1.2 Kramers-Kronig relations

All optical parameters such as dielectric function, conductivity, refractive index, etc. are related to the complex "response function" that describe the response of the material to the electromagnetic waves. The Kramers-Kronig relations tell us that if the system is causal, the real and imaginary parts of the response function are mathematically related.

As explained in section 1.1, in a causal system with local response, we get the following form for a response function $G(t)$:

$$Y(t) = \int_{-\infty}^t G(t-t')X(t')dt' \quad (1.30)$$

Where $X(t)$ is the input signal and $Y(t)$ is the response of the system to X . The

1. THEORY

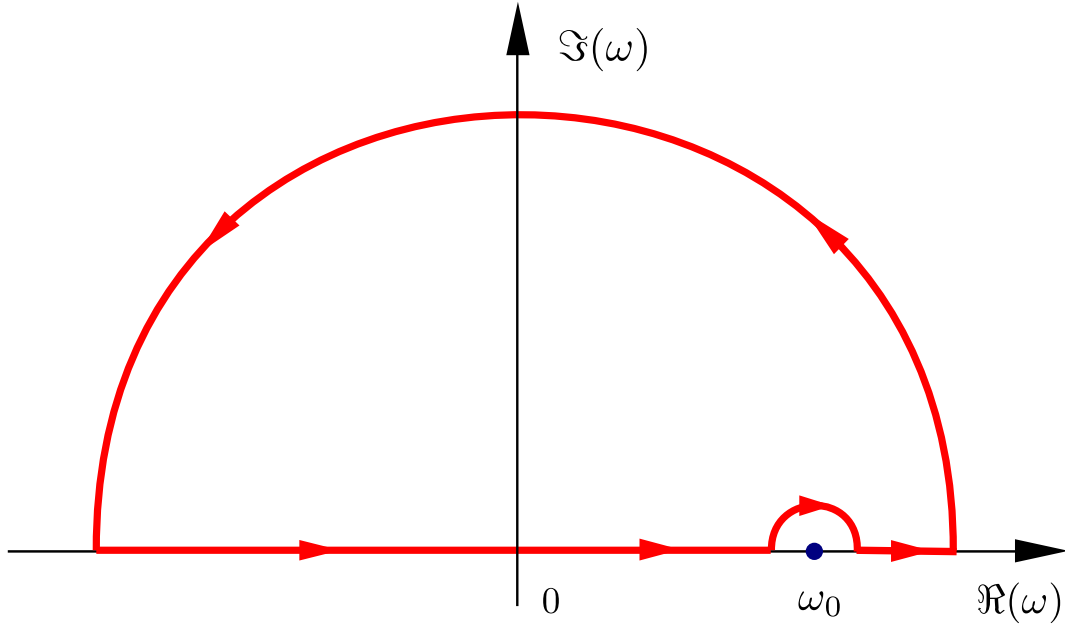


Figure 1.1: Integration path of Cauchy's theorem in the upper half of the complex plane. The large semi-circle as assumed to have infinite radius.

Fourier transform of convolution of two functions corresponds to their multiplication:

$$Y(\omega) = G(\omega)X(\omega) \quad (1.31)$$

For sake of mathematical convenience, we assume that frequency is complex $\omega = \omega_1 + i\omega_2$ and we write the Fourier transform for $G(\omega)$:

$$G(\omega) = \int G(t - t') \exp(i\omega_1(t - t')) \exp(-\omega_2(t - t')) dt \quad (1.32)$$

The second exponent has to be negative to make the response function physically meaningful. At the same time, causality dictates that the time-dependent response function is zero for $t - t' < 0$. So the integral has valid values only for $\omega_2 > 0$ which corresponds to the upper half of the complex plane. For response functions that are analytic in this region, we can write Cauchy's theorem around a contour shown in figure 1.1:

$$\oint_c \frac{G(\omega')}{\omega' - \omega_0} d\omega' = 0 \quad (1.33)$$

For a response function that vanishes at infinity, the integral over the whole imaginary

1.2 Kramers-Kronig relations

range vanishes and we will be left with the real part integral and the small semi-circle around ω_0 for which we use the residue theorem in complex analysis (Cauchy's residue theorem or the Dirac identity) and write:

$$\mathcal{P} \int_{-\infty}^{\infty} \frac{G(\omega')}{\omega' - \omega_0} d\omega' - i\pi G(\omega_0) = 0 \quad (1.34)$$

Where \mathcal{P} is the principal part of the integral. For the second term we have used residue theorem for an assumed semi-circle with radius η : $\omega' = \omega_0 - \eta \exp(i\phi)$. This equation relates the real and imaginary parts of the response function through:

$$G_1(\omega) = \frac{1}{\pi} \mathcal{P} \int_{-\infty}^{\infty} \frac{G_2(\omega')}{\omega' - \omega} d\omega' \quad (1.35a)$$

$$G_2(\omega) = -\frac{1}{\pi} \mathcal{P} \int_{-\infty}^{\infty} \frac{G_1(\omega')}{\omega' - \omega} d\omega' \quad (1.35b)$$

For many practical applications, the equations 1.35 can be made simpler. For example, if our response function is the optical conductivity $\hat{\sigma}$, the integral range starts from zero (instead of $-\infty$). This is because from equation 1.32 it can be seen that $\hat{\sigma}(\omega) = \hat{\sigma}^*(-\omega)$ and hence $\sigma_1(\omega) = \sigma_1(-\omega)$ and $\sigma_2(\omega) = -\sigma_2(-\omega)$. An integral can always be split as:

$$\begin{aligned} \mathcal{P} \int_{-\infty}^{\infty} \frac{\hat{\sigma}(\omega')}{\omega' - \omega} d\omega' &= \mathcal{P} \int_{-\infty}^0 \frac{\hat{\sigma}(\omega')}{\omega' - \omega} d\omega' + \mathcal{P} \int_0^{\infty} \frac{\hat{\sigma}(\omega')}{\omega' - \omega} d\omega' \\ &= -\mathcal{P} \int_0^{\infty} \frac{\hat{\sigma}(-\omega')}{\omega' + \omega} d\omega' + \mathcal{P} \int_0^{\infty} \frac{\hat{\sigma}(\omega')}{\omega' - \omega} d\omega' \\ &= \mathcal{P} \int_0^{\infty} \frac{\omega'[\hat{\sigma}(\omega') + \hat{\sigma}(-\omega')] + \omega[\hat{\sigma}(\omega') - \hat{\sigma}(-\omega')]}{\omega'^2 - \omega^2} d\omega' \end{aligned}$$

This will lead to the following relation between the real and imaginary parts of the

1. THEORY

optical conductivity:

$$\sigma_1(\omega) = \frac{2}{\pi} \mathcal{P} \int_0^\infty \frac{\omega' \sigma_2(\omega')}{\omega'^2 - \omega^2} d\omega' \quad (1.36a)$$

$$\sigma_2(\omega) = -\frac{2\omega}{\pi} \mathcal{P} \int_0^\infty \frac{\sigma_1(\omega')}{\omega'^2 - \omega^2} d\omega' \quad (1.36b)$$

Similar equations are used for other optical parameters. In chapter 2 these equations will be used to calculate the phase of the reflected light from its frequency-dependent reflection amplitude. Theoretically, the Kramers-Kronig relations need the full frequency range of a response function to work. In practice, however, fairly precise results are obtained by using measured data in a limited range completed by appropriate approximations for the missing parts. These approximations come from models that are generally believed to hold for optical parameters.

1.3 Drude model of metals

In this section I give a very short description of the Drude model for conductivity of metals together with some of its implications. The model is based on the assumption that electrons in metals behave like a classical gas with an average relaxation time τ . The equation of motion for this classical gas in the presence of an electric field \mathbf{E} is written as:

$$m \frac{\partial}{\partial t} \mathbf{p} + \frac{\mathbf{p}}{\tau} = -e\mathbf{E} \quad (1.37)$$

Where \mathbf{p} is the average electron momentum and $-e$ is the electron charge. We have also the linear response conductivity defined as $\mathbf{J} = \sigma \mathbf{E}$. By defining the current density $\mathbf{J} = -Ne\mathbf{p}/m$ (where m is the electron mass and N is the charge carrier density), and assuming an alternating electric field of $\mathbf{E}(t) = \mathbf{E}_0 \exp(-i\omega t)$ we get the following solution for conductivity from the Drude equation of motion (eq. 1.37):

$$\hat{\sigma}(\omega) = \frac{Ne^2\tau}{m} \frac{1}{1 - i\omega\tau} = \frac{\omega_p^2}{4\pi} \frac{\tau}{1 - i\omega\tau} \quad (1.38)$$

Where $\omega_p = \sqrt{\frac{4\pi Ne^2}{m}}$ is the plasma frequency.

It should be noted that the classical Drude model for gases gives a mean free path

proportional to the average velocity which is determined by the gas temperature. In metals, however, only the electrons close to the Fermi surface are affected by the electric field and the scattering process follows different physics than of the gas model. In many cases, the Drude model is not enough to describe the response of metals to an electric field and corrections need to be applied to the Drude model as will be shown later in this chapter.

1.3.1 Hagen-Rubens approximation

For energies much smaller than the scattering rate τ^{-1} the ‘‘Hagen-Rubens’’ regime holds where the dc conductivity of the metal dominates the optical response:

$$\sigma_1(\omega) \approx \sigma_{dc} \quad (1.39a)$$

$$\sigma_2(\omega) \approx \sigma_{dc}\omega\tau \quad (1.39b)$$

Among all the optical properties in this regime, we highlight the reflectivity amplitude $R(\omega)$ which becomes a linear function of the square root of frequency:

$$R(\omega) \approx 1 - \sqrt{\frac{2\omega}{\pi\sigma_{dc}}} \quad (1.40)$$

This equation is in particular useful for verification of reflectivity data at low frequency and high temperatures (where the scattering rate is larger for metals).

1.3.2 Drude-Lorentz model

A phenomenological development of the Drude model is the ‘‘Drude-Lorentz model’’ where (in addition to the Drude part) the optical conductivity is represented by Lorentzians that can account for any non-Drude contribution to the optical conductivity:

$$\hat{\sigma}(\omega) = \frac{\omega_p^2}{4\pi} \cdot \frac{1}{\gamma - i\omega} + \sum_j \frac{\omega_{pj}^2}{4\pi} \cdot \frac{i\omega}{(\omega^2 + i\gamma\omega - \omega_0^2)} \quad (1.41)$$

The first term in Eq. 1.41 is the Drude optical conductivity as in Eq. 1.38 (note that the relaxation time τ is the inverse of scattering rate γ).

The Drude-Lorentz model is very useful in modeling of phonons and interband

1. THEORY

transitions. This model is Kramers-Kronig consistent and can be used to extrapolate (or interpolate) the missing parts of optical conductivity.

1.4 Extended Drude model

By assuming frequency dependence for the scattering rate (τ^{-1}) due to electron-electron interactions or electron-phonon coupling, KK consistency of the optical conductivity in equation 1.38 imposes a frequency dependence for the mass. We can express the optical conductivity using a complex "memory function" [2] $M(\omega)$ that contains both frequency dependent scattering rate $\Gamma_1(\omega)$ and mass $m^*(\omega)$:

$$\hat{\sigma}(\omega) = \frac{\omega_p^2}{4\pi} \cdot \frac{i}{M(\omega) + \omega} = \frac{\omega_p^2}{4\pi} \cdot \frac{1}{\tau^{-1}(\omega) - i\omega[\frac{m^*(\omega)}{m_b}]} \quad (1.42)$$

where the frequency dependent scattering rate and mass are connected to real and imaginary parts of the memory function (M_1 & M_2) through:

$$\frac{m^*(\omega)}{m_b} = 1 + \frac{M_1(\omega)}{\omega} \quad (1.43)$$

$$\tau^{-1}(\omega) = M_2(\omega) \quad (1.44)$$

As seen in equations 1.43 and 1.44, the frequency dependent scattering rate equals the imaginary part of the memory function while the mass enhancement (m^*/m_b) is indirectly related to the real part of memory function. In absence of interband transitions, the spectral sum rule gives the value for the plasma frequency through equation 1.45.

$$\frac{\omega_p^2}{8} = \int_0^\infty \sigma_1(\omega) d\omega \quad (1.45)$$

The optical conductivity could also be expressed as sheet conductance in units of $G_0 = 2e^2/h$:

$$G(\omega) = \frac{i\pi K}{\hbar\omega + M(\omega)} G_0 \quad (1.46)$$

The spectral weight factor K is related to the plasma frequency through the relation

$$\hbar^2 \omega_p^2 = \frac{4\pi e^2}{d_c} K \quad (1.47)$$

where $d_c = c/N_L$ is the average spacing between copper-oxide layers. c is the c-axis lattice parameter and N_L is the number of CuO_2 layers per unit cell.

1.5 Kubo formula

In this section, a brief derivation of the Kubo formula is given which expresses the real part of the optical conductivity in terms of current-current correlations. The imaginary part can be calculated using the Kramers-Kronig transformations. Doing so, we consider the electromagnetic fields (expressed by vector and scalar potentials) as a perturbation \mathcal{H}_{int} added to the ground state Hamiltonian \mathcal{H}_0 . We will only consider the first-order expansion of the vector potential \mathbf{A} . We are interested in the transverse response of the perturbation which for a Coulomb gauge ($\nabla \cdot \mathbf{A} = 0$) is the response to the vector potential \mathbf{A} . In this scenario the perturbation (or interaction) Hamiltonian takes the form:

$$\mathcal{H}_{int}^T = \frac{e}{2mc} \sum_{i=1}^N [\mathbf{p}_i \cdot \mathbf{A}(r_i) + \mathbf{A}(r_i) \cdot \mathbf{p}_i] \quad (1.48)$$

By respecting the commutation rules the current operator $\mathbf{J}(r)$ can be expressed in terms of the velocity operator \mathbf{v}_i at point i in space:

$$\mathbf{J}(r) = -\frac{e}{2} \sum_{i=1}^N [\mathbf{v}_i \delta_i + \delta_i \mathbf{v}_i] \quad (1.49)$$

By putting the velocity operator of an electron $\mathbf{v} = \frac{\mathbf{p}}{m} + \frac{e\mathbf{A}}{mc}$ in equation 1.49, we get two terms for the current which we call paramagnetic and diamagnetic terms:

$$\begin{aligned} \mathbf{J}(r) &= \mathbf{J}_p(r) + \mathbf{J}_d(r) \\ &= -\frac{e}{2m} \sum_{i=1}^N [\mathbf{p}_i \delta_i + \delta_i \mathbf{p}_i] - \frac{e^2}{mc} \sum_{i=1}^N A_i \delta_i \end{aligned} \quad (1.50)$$

Which, in Coulomb's gauge, enables us to write the transverse perturbation Hamiltonian and its Fourier transform as:

$$\mathcal{H}_{int}^T = -\frac{1}{c} \int \mathbf{J}(r) \cdot \mathbf{A}(r) dr \quad (1.51)$$

$$\mathcal{H}_{int}^T = -\frac{1}{c} \mathbf{J}(q) \cdot \mathbf{A}(q) \quad (1.52)$$

1. THEORY

We can write the total transition (absorption) rate by summing the Fermi's golden rule over all initial states $|i\rangle$ to final states $|f\rangle$ and expressing the perturbation Hamiltonian in terms of current:

$$\begin{aligned}
W &= \sum_{i,f} W_{i \rightarrow f} \\
&= \sum_{i,f} \frac{2\pi}{\hbar^2} |\langle f | \mathcal{H}_{int}^T | i \rangle|^2 \delta(\omega - \Delta\omega_{i \rightarrow f}) \\
&= \sum_{i,f} \frac{2\pi}{\hbar^2 c^2} \langle f | \mathbf{J}(q)^T | i \rangle \langle i | \mathbf{J}(q)^{T*} | f \rangle |\mathbf{A}^T(q)|^2 \delta(\omega - \Delta\omega_{i \rightarrow f}) \\
&= |\mathbf{E}^T(q)|^2 \sum_i \frac{1}{\hbar^2 \omega^2} \int dt \langle i | \mathbf{J}^T(q, 0) \mathbf{J}^{T*}(q, t) | i \rangle \exp(-i\omega t)
\end{aligned} \tag{1.53}$$

Here, $W_{i \rightarrow f}$ is the transition rate from state $|i\rangle$ to $|f\rangle$ and $\Delta\omega_{i \rightarrow f}$ is the frequency difference between the initial and final states. In the last term, the time evolution operator has been used assuming that the perturbation was turned on at time $t = 0$.

For an electromagnetic wave the transverse electric field is related to the vector potential through $\mathbf{E} = i\omega \mathbf{A}^T/c$. The absorbed power and electric field and transition rate are connected through:

$$P = \hbar\omega W = \sigma_1^T (\mathbf{E}^T)^2 \tag{1.54}$$

Which gives the Kubo formula for the dissipative part of the conductivity:

$$\sigma_1^T(q, \omega) = \sum_i \frac{1}{\hbar\omega} \int \langle i | \mathbf{J}^T(q, 0) \mathbf{J}^{T*}(q, t) | i \rangle \exp(-i\omega t) dt \tag{1.55}$$

The equation above resembles the fluctuation dissipation theorem and is based on fluctuations in the ground state. For most metals the density of states is considered to be constant as the dominating transitions occur within the conduction band close to the Fermi surface. If transition with Fermi statistics are studied, the Kubo formula takes a different form (in the $T = 0$ limit):

$$\sigma_1(\omega) = \frac{\pi e^2}{m^2 \omega} |\langle f | \mathbf{p} | i \rangle|^2 D_{i \rightarrow f}(\omega) \tag{1.56}$$

where $D_{i \rightarrow f}(\omega)$ is the joint density of states.

1.6 Fermi liquid

1.6.1 Memory function of a local Fermi liquid

For a system whose carriers can be well described by a local (i.e. momentum independent) scattering rate, the optical conductivity can be expressed entirely in terms of the complex electronic self-energy $\Sigma(\varepsilon) \equiv \Sigma_1(\varepsilon) + i\Sigma_2(\varepsilon)$. The scattering rate is $-\Sigma_2$, and Σ_1 is linked to Σ_2 by a Kramers-Kronig transformation. This happens because, for a local self-energy, the vertex corrections vanish in the Kubo formula for the conductivity $\sigma(\omega)$. As a result,

$$\sigma(\omega, T) = \int d\varepsilon \frac{i\Phi(0)}{\omega} \frac{f(\varepsilon) - f(\varepsilon + \hbar\omega)}{\hbar\omega + \Sigma^*(\varepsilon) - \Sigma(\varepsilon + \hbar\omega)} \quad (1.57)$$

Here $f(\varepsilon) = [\exp(\varepsilon/k_B T) + 1]^{-1}$, and $\phi(0)$ is proportional to the Fermi-surface average of the square of the bare electronic group velocity. In a Fermi liquid, the quasi-particles are well-defined at low temperature close to the Fermi surface, because in this limit the scattering rate vanishes with a characteristic energy and temperature dependence proportional to $\varepsilon^2 + (\pi k_B T)^2$. The quasi-particle spectral weight Z is smaller than unity, as reflected by the fact that $\Sigma_1(\varepsilon)$ has a finite negative slope $1 - 1/Z$ at $\varepsilon = 0$. This leads to the following low-energy model for the self-energy of a local Fermi liquid:

$$\Sigma(\varepsilon) = \left(1 - \frac{1}{Z}\right) \varepsilon - \frac{3}{2} iC [\varepsilon^2 + \pi^2 (k_B T)^2] \quad (1.58)$$

The added factor $3/2$ anticipates the formula for the memory function. In systems where all properties are set by a single characteristic energy D , like in isotropic doped Mott insulators where D is typically the half bandwidth, the coefficient C would be proportional to $1/(Z^2 D)$. Indeed, in such cases the scattering rate $-\Sigma_2(0)$ scales with renormalized electronic energies like $D(k_B T/ZD)^2$. The quasi-particle life-time controls the Drude response at very low frequencies. On the Fermi surface, it can be computed from the self-energy as $\tau_{qp} = \hbar/(2Z|\Sigma_2(0)|)$. We are interested in the regime of frequencies much larger than $1/\tau_{qp}$: introducing Eq. 1.58 into Eq. 1.57, and expanding

1. THEORY

for large $\omega\tau_{qp}$, we get

$$\begin{aligned} \sigma(\omega, T) = & \\ \Phi(0) Z\tau_{qp} & \left\{ \frac{i}{\omega\tau_{qp}} + \frac{4}{3(\omega\tau_{qp})^2} \left[1 + \left(\frac{\hbar\omega}{2\pi k_B T} \right)^2 \right] \right\} \\ & + O[1/(\omega\tau_{qp})^3] \end{aligned} \quad (1.59)$$

The expression of the conductivity in terms of the memory function is $\sigma(\omega) = i\hbar\phi(0)/[\hbar\omega + M(\omega)]$. Comparing this with Eq. 1.58, we obtain:

$$M(\omega, T) \cong \left(\frac{1}{Z} - 1 \right) \hbar\omega + iC [(\hbar\omega)^2 + (p\pi k_B T)^2] \quad (1.60)$$

in the regime $\omega\tau_{qp} \gg 1$. Note that here, for consistency with Eq. 1.47, we have defined $M(\omega)$ using the full spectral weight, which is proportional to $\phi(0)$. If the experimentally determined spectral weight K underestimates the full spectral weight by a factor α , the measured value of the residue –from the slope of $M_1(\omega)$ – will overestimate Z by a factor α .

Experimental

2.1 Introduction

Nowadays, thanks to the advances in instrumentation of optical spectroscopy, it is not a difficult task to measure optical spectra of a reflecting surface of a few squared millimeters at room temperature. However, in many situations those conditions are not met and measuring optical spectra with high accuracy becomes a very demanding task. In our field of research, where we need to measure the absolute value of reflectivity for very small crystals (down to sub-millimeters dimensions) within an error margin of about 1% while covering a wide temperature range, extra attention needs to be paid during measurements. Such experiments turn out to be sometimes very difficult (and time-consuming) while the chances for failure are much higher as compared to an ordinary measurement. Some of the main difficulties in performing such experiments are related to:

1. Sample preparation (small sample size, surface alignment difficulties and oxidation of the sample in air)
2. Signal acquisition (need for accurate optical alignment, weak signal)
3. Signal stability (mechanical effects during thermal cycle, drift and limited lifetime of detectors, source instability, interferometer instability, etc.)
4. Vacuum requirements (water absorption)

In this chapter, some of the methods to counter the problems mentioned above are explained.

2. EXPERIMENTAL

2.2 Sample preparation

The sample preparation for optical measurements concerns two main aspects: the thermo-mechanical contact and the surface quality.

For contact, the samples can easily be mounted on the tip of a copper cone using silver paste. The only subtlety is that the optimal amount of paste should be applied in order to avoid chemical contamination of the sample on one hand, and to keep strong physical and thermal connection on the other hand. To do that, silver paste has been put in vacuum until the bubbles disappeared. This method reduces the risk of bubble formation (which turn into cavities in the dried paste) while the paste is drying. To obtain high contact quality, we applied the paste twice: once with a very little amount only to have the crystal glued to the cone tip and the second time (after the first paste dries) to make a stronger contact.

For surface preparation, different methods apply depending on the type of crystal. Before going into details, it should be reminded that our optical experiments consist of several rounds of measurements during each we need to deposit a layer of gold on the sample. Therefore, we will have to remove the gold layer before the next measurement. This is usually done using a scotch tape and, as we will see, may cause the sample to cleave together with the gold. Moreover, the cleavage of gold may not work all the time depending on how strongly the film is stuck to the sample. Therefore, in some cases we will have to either re-cleave the sample together with the gold or simply polish it.

In case of the $\text{SrFe}_{2-x}\text{Co}_x\text{As}_2$ family (Sr122 from now on), a fresh surface (which corresponds to ab-plane) can be obtained by cleaving the crystals using scotch tape. In case of unsuccessful gold removal, the crystals can easily be cleaved again to obtain a fresh surface. This, of course, could be a source of spectral mismatch among different measurements on one sample because of possible change in layer properties due to inhomogeneity of the grown crystal.

For the $\text{HgBa}_2\text{CuO}_{4+\delta}$ family (Hg1201 from now on), cleaving does not work using tapes and mechanically stronger methods are needed which increase the risk of damaging or losing the sample. To avoid this problem, we have chosen to polish the mercury-based crystals after each measurement by applying dry abrasive with grain size of around $0.1 \mu\text{m}$. As will be shown, failure in polishing the sample exactly parallel to ab-plane will introduce some c-axis contribution to the optical data. This problem can be avoided using a polarizer at the cost of losing some signal intensity.

2.3 Optical measurements

In this section, the two methods of obtaining optical spectra are explained. For the far-near infrared range (6 meV-1.2 eV), an FTIR spectrometer was used in reflection mode to measure optical response of the crystals. For measurements in the range of near IR to UV, an ellipsometer was used.

2.3.1 Reflectivity

2.3.1.1 Optical setup

We used the BRUKER IFS113v FTIR spectrometer for reflectivity measurements. This spectrometer employs the Genzel interferometer that has two distinct properties as compared to the standard Michelson interferometer[3]:

1. The beam is focused on the beamsplitter allowing for small-size beamsplitters and therefore less drum-head vibrations which happens in particular in large-diameter Mylar[®] beamsplitters.
2. The angle of incidence on the beamsplitter ($\sim 15^\circ$) is much smaller than normal angle (as in the standard Michelson setup). This allows for almost equal intensities for both s and p polarizations and hence makes it easier to study sample polarization effects because there will be no need to change the sample orientation during the experiment.

The optical beam path used for reflectivity measurement is shown in Figure 2.1. To cover the wide spectral range of 6meV-1.2eV, several configurations need to be used each having different source, beam-splitter, polarizer and detectors. Table 2.1 lists the set of optical elements used for each measured spectral range.

Table 2.1: Measurement settings for different frequency ranges.

Effective frequency(meV)	2.5-12.5	6-85	62-490	490-1200
Source	Hg	Hg/Globalar	Globalar	Tungsten
Beam splitter	Si10	Ge/Mylar	Ge/KBr	Si/CaF
Detector	Bolo2K	Bolo4K	BoloMIR/MCT	MCT
Window	Diamond-PE	Diamond	Diamond-KBr	Diamond
Polarizer	Gold	Gold	KrS-5	Polaroid

2. EXPERIMENTAL

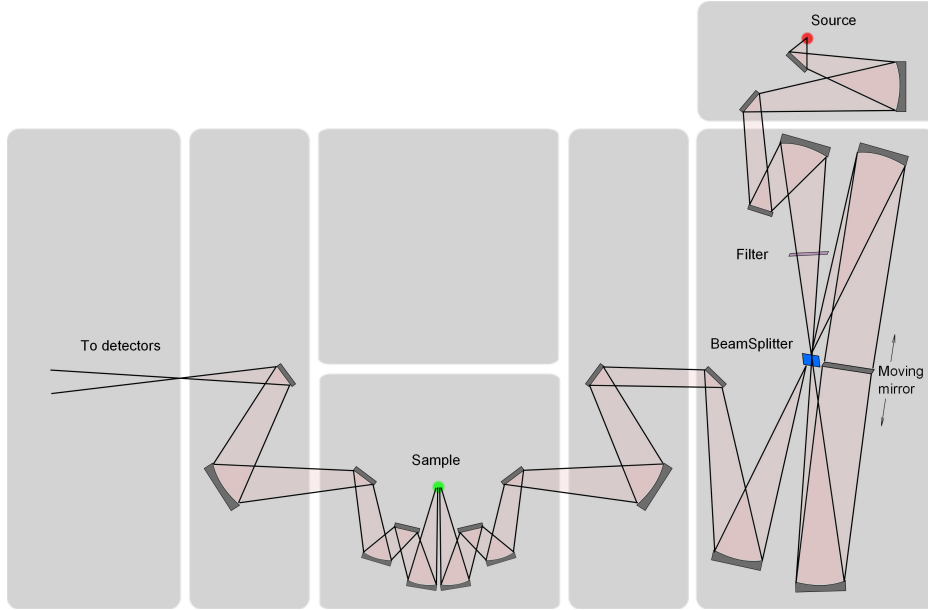


Figure 2.1: Beampath of the Bruker IFS 113v spectrometer in reflection mode.

2.3.1.2 Optical cryostat

We used a home-made UHV optical cryostat with a diamond window for the reflectivity measurements. The temperature range covered by this cryostat was 10-400K. The typical pressure for measurements with this cryostat was $10^{-6} - 10^{-9}$ torr depending on the temperature and pre-baking conditions. If a very high vacuum is needed, the cryostat must be baked at about 150°C for about 24 hours or more. When aiming at very high vacuums, the O-rings used must be made of oxygen-free copper(OFC). The cryostat is equipped with an ion gauge and an ion pump. It also accommodates two gold evaporation units.

2.3.1.3 Reference measurement

In order to obtain the absolute value of reflectivity, we need to normalize the measured reflectance by a perfect reflector that has the same surface properties as the sample(surface area, roughness, thermal expansion, etc.). One of the best methods is to deposit a layer of a highly reflective metal on our sample. This way, the reference signal follows all the sample properties during the thermal cycle and reduces the error in absolute reflectivity measurement. For far and mid-infrared range, gold is a very good mirror because of its perfect metallic properties. The gold reflectivity will drop

and will also have contributions from interband transitions when it reaches frequencies higher than 1.2 eV. For those frequencies, silver or aluminum are used instead of gold in order to give flat frequency distribution of reflection. We have used twisted tungsten wires to hold and evaporate gold. Usually a power of around 50 Watts is needed for about 15 seconds to perform the evaporation.

2.3.1.4 Polarizer

For the case of Hg1201 samples (where the surface is polished), there is a chance of having c-axis optical response in the measured data due to the possible miscut caused by inaccurate polishing of the surface or existence of multiple domains. The c-axis contribution can easily be observed as strong c-axis phonon peaks at frequencies around 19.2 meV, 52.7 meV and 80.6 meV (see figure 2.2). The c-axis contribution effect is more difficult to distinguish from ab plane response at higher frequencies because c-axis reflectivity is almost constant and has no features at that range (no phonons). A very effective way to correct for this effect is to use polarizers that polarize light in a direction parallel to the direction of miscut lines on the surface (the miscut lines represent the edges of the ab planes that are terminated at the surface). A comparison of spectra from different polarization angles is shown in figure 2.2. To find the right polarization angle, we changed the angle of the polarizer until the effect of the c-axis phonon disappeared. This method has the disadvantage of losing more than 50% of the light intensity during the measurement and usually becomes a challenge for experiments with small samples. Once we use a polarizer in the low frequency range, we must use polarizers of exactly the same polarization angle for all frequency ranges. Because not all polarizers come with indicated polarization axis, we had to find the axis position by measuring the transmitted signal intensity through a silicon wafer that is rotated around the vertical axis by its nominal Brewster's angle. In this configuration, the signal will drop to a minimum when polarizer axis is at vertical position (see figure 2.3). This way, the axis of each polarizer will be defined with respect to its frame and helps us set the correct zero for the stepper motor controller.

2.3.1.5 Drift Corrections

There are several sources of error in reflectivity measurements. One source is indeed the noise in optical signal measured during each scan. This error can be reduced by increasing the signal amplitude or the number of scans (energy or time). Another source

2. EXPERIMENTAL

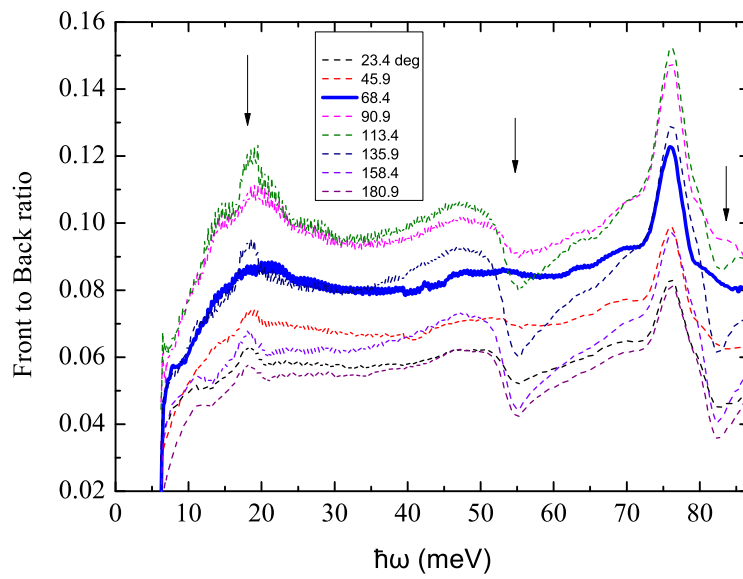


Figure 2.2: Effect of c-axis phonons (Hg1201) on the spectra for different polarization angles. The effect of three c-axis phonons at around 19.2 meV, 52.7 meV and 80.6 meV is clearly seen when polarization angle is far from the angle that corresponds to the surface miscut (68 degrees).

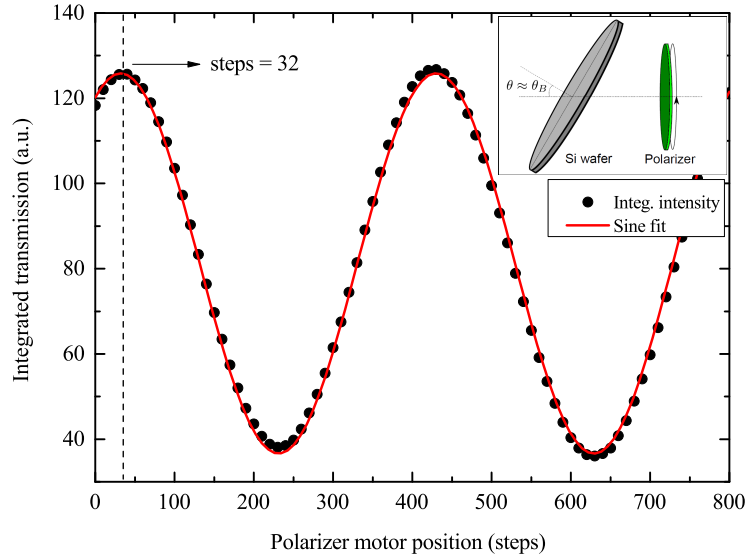


Figure 2.3: Finding polarizer axis using transmission through a Silicon wafer close to the Brewster’s angle. This specific example applies to the gold polarizer for low frequency range(6-85 meV). The inset shows the polarizer and the tilted Si wafer from top view.

of error is the drift in signal amplitude during a long period of measurement. This drift may come from the instability of either source or detector. In order to distinguish the drift from the temperature induced variations in sample, we should be able to measure the signal without being reflected from the sample during the measurement. One simple way is to change the beampath and send the beam through the back-channel of the spectrometer (IFS 113v has two separate chambers with possibility of sending the beam through one or the other). This requires two of the mirrors to change their position twice in order to measure the back-channel signal and switch back to front channel. The problem with such method is that any change in the beampath will itself introduce an error due to possible mechanical reproducibility problems. We have developed a very reproducible way of changing the beampath and measuring the signal without hitting the sample on the way. As shown in figure 2.4 we have added a sliding mirror controlled by a piezoelectric stepper motor to deflect the beam right at the beam focal point before entering the cryostat. The deflected beam hits a fixed mirror outside the cryostat (which is assumed not to be changing its position) and will follow the same beampath as the measurement on the sample does. This way, we have avoided

2. EXPERIMENTAL

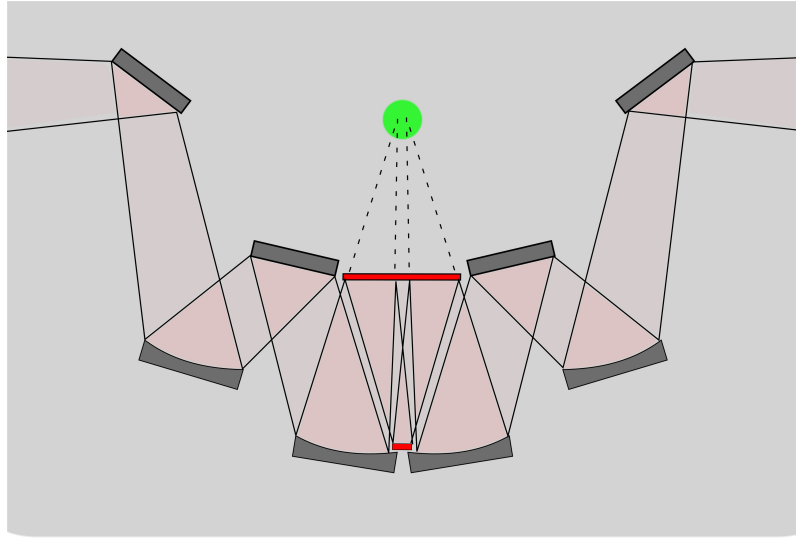


Figure 2.4: Optical setup for reference measurement outside the cryostat. Two additional mirrors (shown in red) are used: The large one reflects the beam before entering the cryostat and sends it to the small reference mirror outside the cryostat.

the mechanical movement of sensitive parts inside the spectrometer (like the flipping mirrors). In the worst case of irreproducibility in mirror movement, nothing would be affected on the main beampath. Using this method, during the measurement, we can regularly measure the signal outside the cryostat and later separate instabilities caused by source and detector from those caused by sample (and cryostat). An example of source (detector) drift is shown in figure 2.5. We see that a drift of about 7% happens during 30 hours for a detector (here MCT) that was refilled with liquid nitrogen twice. The first and second jumps in signal happen after the first and second refilling of the detector. The third jump corresponds to the instabilities in the detector when it starts to run out of liquid nitrogen. In such cases, we have to re-normalize signal intensity measured from the sample by the external mirror signal in order to get the correct (temperature-induced) behavior. There are other sources of error such as mechanical displacements due to thermal cycle or formation of mechanical defects on the sample during the measurement (cracks or surface oxidation). The thermal cycle problem could be avoided -to a good extent- by "training" the sample inside cryostat which means cooling (and warming) it through the thermal cycle before the real measurement exactly the same way as planned for the measurement. Concerning the defects problem, high vacuum maintenance and proper surface treatments typically help.

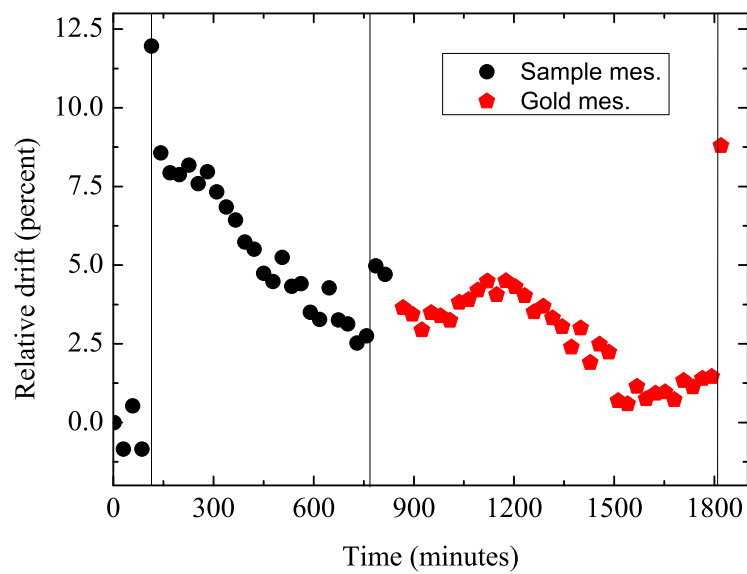


Figure 2.5: Drift in signal of the external reference mirror shows the scale of instabilities that may exist in sources and detectors. The solid vertical lines show sharp drifts that correspond to some physical change in the spectrometer as explained in the text. This graph shows drift for a combination of Globar (as source) and MCT (as detector). The colors correspond to the type of ongoing measurement (sample or gold) and have no effect on the reference mirror signal shown here.

2. EXPERIMENTAL

2.3.2 Ellipsometry

For frequency ranges typically between 0.62-5.5 eV the ellipsometry technique was used to determine optical properties. This method has many advantages over reflectivity method such as: not requiring the reference measurement (no metallic film deposition), high stability against source drift and also ability to measure both real and imaginary parts of the optical constants. However, there are disadvantages too. For example, as the measurements are performed at angles much larger than the normal angle, the effect of c-axis component of the optical response has to be taken into account when studying highly anisotropic crystals like Hg1201 (this problem has nothing to do with the possible miscut of surface). This requires direct access to the c-axis response which are typically possible through reflectivity measurements on ac (or bc) plane while using a polarizer to pick up the c-axis response only. Such measurements are usually challenging due to the poor signal obtained from the small cross section area as well as the difficulties in polishing and surface preparation. A microscope-equipped FTIR spectrometer with polarized incident light was used to get c-axis response from ac (bc) planes (shown in figure 2.6). We have used a J.A. Woollam variable angle spectroscopic ellipsometer (VASE[®]) to measure optical response in the 0.62-3.7 eV range. Separate measurements on ac (or bc) plane have been done to help us distinguish between the ab-plane and the c-axis response. The ellipsometer measures two angles ψ and Δ which are a measure of the reflectivity ratio of s and p-polarized light:

$$\rho = \frac{r_p}{r_s} = \tan(\psi)e^{i\Delta} \quad (2.1)$$

These two variables are connected to the real and imaginary parts of the dielectric function through [1]:

$$\epsilon_1 = \sin^2(\theta_i) \left[1 + \frac{\tan^2(\theta_i) (\cos^2(2\psi) - \sin^2(\Delta)\sin^2(2\psi))}{(1 + \sin(2\psi) \cos(\Delta))^2} \right] \quad (2.2)$$

$$\epsilon_2 = \sin^2(\theta_i) \frac{\tan^2(\theta_i) \sin(4\psi) \sin(\Delta)}{(1 + \sin(2\psi) \cos(\Delta))^2} \quad (2.3)$$

Where θ_i is the angle of incidence and ψ and Δ are the angles measured by the ellip-

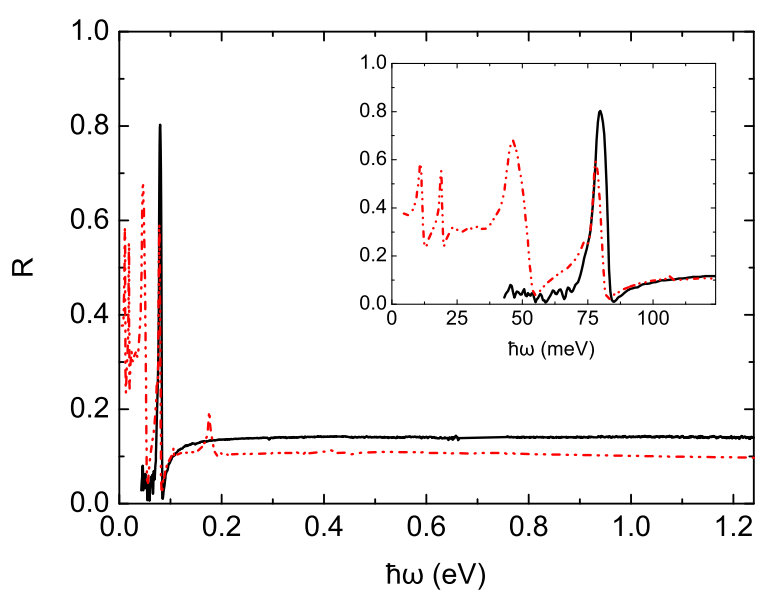


Figure 2.6: The solid curve shows c-axis reflectivity of Hg1201($T_c=67\text{K}$) measured using a microscope and polarized light. Data shown as the dashed line correspond to c-axis reflection from the same family of compound with different doping [4].

2. EXPERIMENTAL

someter.

2.3.2.1 Window and lens corrections (Ellipsometry)

We used two lenses to focus the light beam on tiny samples. This, together with the two windows of the optical cryostat, may introduce a change in the measured optical data by depolarizing the beam. In some cases, this change is noticeable and a correction routine must be applied before any further data processing. To do so, we need to extract the effect of the lenses and the windows by measuring on the sample once without any lens and window and once with them both at room temperature. Because the properties of lens and window do not change during the thermal cycle, their contribution to the signal is considered to be the same for all sample temperatures. The following equations show how to extract ψ_{win} and Δ_{win} which correspond to the window (and lens) contribution to measured ψ and Δ at a chosen temperature:

$$\tan(\psi_{win}) = \frac{\tan(\psi_{cryo})}{\tan(\psi_{free})} \quad (2.4)$$

$$\Delta_{win} = \Delta_{cryo} - \Delta_{free} \quad (2.5)$$

Where "cryo" index indicates values measured through the lens and cryostat window and "free" index means measurements in free space without any lens or window.

Once we obtain the window and lens contribution to the signal (marked with "win" index), we can continue the measurement inside the cryostat for all the temperatures and correct them later:

$$\tan(\psi_{corr}) = \frac{\tan(\psi_{cryo})}{\tan(\psi_{win})} \quad (2.6)$$

$$\Delta_{corr} = \Delta_{cryo} - \Delta_{win} \quad (2.7)$$

Where the "corr" index means the corrected value with respect to the window (and lens) effect.

2.3.2.2 C-axis corrections

The reflected light with p polarization is a function of refraction index along both ab-plane and c-axis. Because ellipsometer basically measures the ratio of p and s reflected

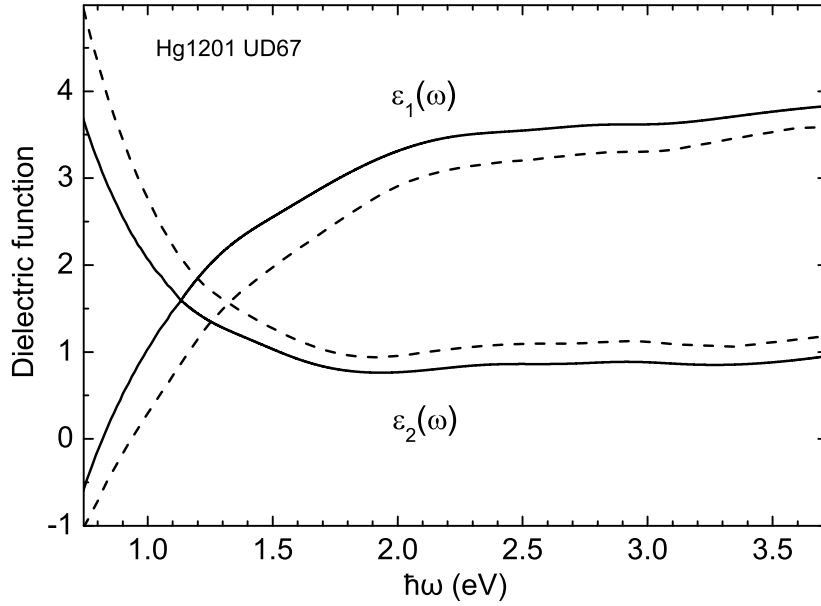


Figure 2.7: Comparison between the pseudo-dielectric function measured on Hg1201 (dashed line) and the dielectric function calculated with help of the measured c-axis optical data (solid line).

light, the output will depend on the c-axis index of refraction n_c through:

$$\rho = \frac{r_p}{r_s} = \frac{\sqrt{n_c^2 - \sin^2(\theta)} - n_c n_b \cos(\theta)}{\sqrt{n_c^2 - \sin^2(\theta)} + n_c n_b \cos(\theta)} \cdot \frac{\sqrt{n_a^2 - \sin^2(\theta)} + \cos(\theta)}{\sqrt{n_a^2 - \sin^2(\theta)} - \cos(\theta)} \quad (2.8)$$

Where $n_a = n_b$ for tetragonal samples such as Hg1201. In order to obtain n_a (and therefore other optical constants) we will need to have the value for n_c . That is where knowing the c-axis optical response becomes crucial. It is difficult to invert the equation 2.8 and express n_a directly. However, n_a can be numerically calculated and converted to required optical constants such as dielectric function ϵ . Figure 2.7 shows the "pseudo-dielectric function" resulting from conversion of n_a under isotropic assumptions ($n_a = n_b = n_c$) and the dielectric function obtained from realistic assumptions ($n_a = n_b \neq n_c$).

2. EXPERIMENTAL

2.4 Data analysis

2.4.1 Optical conductivity

In principle, optical parameters can be converted to each other through fairly simple relations. The problem is that in reflectivity (R) measurements, we only have access (within a limited frequency range) to the absolute value of the complex reflectance (\hat{r}):

$$R = |\hat{r}|^2 = |r_1 + ir_2|^2 \quad (2.9)$$

To calculate any optical constant, we will need to have both real and imaginary parts of the reflectance. As seen in section 1.2, for any casual response function, one can relate the real and imaginary parts through Kramers-Kronig transformations. Since we can only measure the absolute value of the reflectance (which has contributions from both real and imaginary parts), we need to do a transformation through which the measured value will correspond to the real part of a complex value. For this purpose, we write square of reflectance in the phasor form:

$$\hat{r}^2 = |\hat{r}|^2 \cdot e^{i\phi} = R \cdot e^{i\phi} = e^{\ln(R) + i\phi} \quad (2.10)$$

This way, the natural logarithm of the complex reflectance \hat{r} will be expressed as a complex number with $\ln(R)$ as the measured real part which (for normal angle of incident) is related to the imaginary part (ϕ) through Kramers-Kronig transformations:

$$2 \ln(\hat{r}) = \ln(R) + i\phi \quad (2.11)$$

$$\phi = -\frac{2\omega}{\pi} \mathcal{P} \int_0^\infty \frac{\ln(R)}{\omega'^2 - \omega^2} d\omega' \quad (2.12)$$

The factor of two and the integral range from zero (instead of $-\infty$) to ∞ are both because $R(\omega)$ is the fourier transform of a real value and therefore it is an even function ($R(\omega) = R(-\omega)$). The problem here is that we have access to a limited range of $R(\omega)$ while the whole range is needed for the Kramers-Kronig transformation. Indeed, it is impossible to measure the full range of $R(\omega)$ but we can use estimations that give fairly accurate results for the desired range. To estimate the full-range reflectivity, we fitted both the reflectivity and the ellipsometry data to a Drude-Lorentz model and used the model-generated values to fill the low-frequency part as well as to extend the

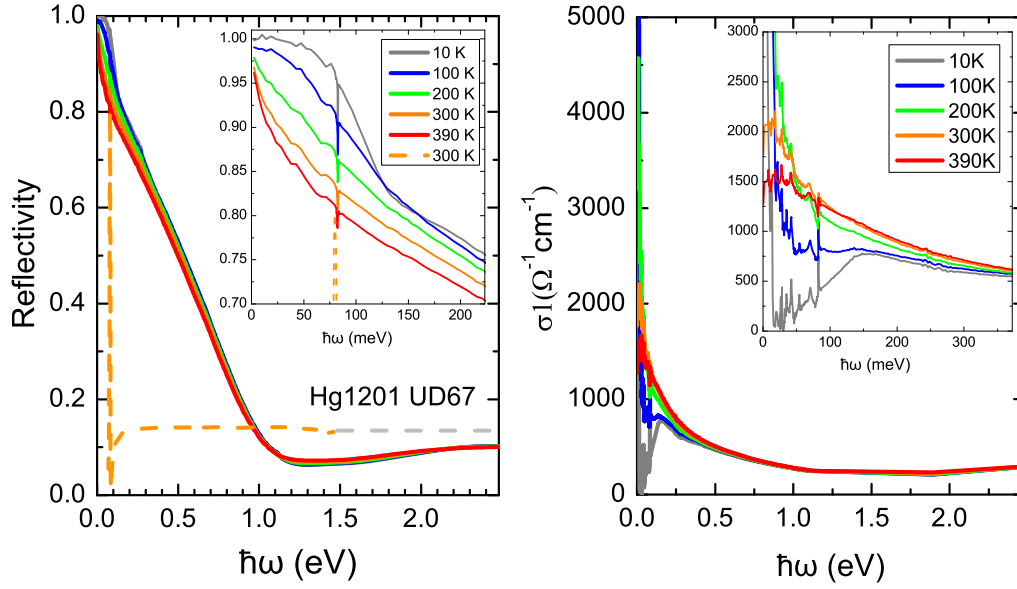


Figure 2.8: Measured reflectivity (left panel) and the real part of the optical conductivity calculated through Kramers-Kronig transformations (right panel). The dashed curves in reflectivity panels correspond to the *c*-axis measurements.

reflectivity to frequencies up to 25 eV. From 25 eV to 50 eV we assume $R = \omega^{-4}$ and then we perform the integral over 0-50 eV range. It should be reminded that the inaccuracies in *R* estimations at high frequencies have very little effect on low frequency output of the integral. The only important point is that the integrand must be a Kramers-Kronig consistent function.

By applying the Kramers-Kronig transformation as explained above, we get the complex reflectance \hat{r} and we can get to all optical constants using known relations [1]. Here, we used equation 2.13 to get optical conductivity $\sigma(\omega)$ in units of $\Omega^{-1}cm^{-1}$:

$$\hat{\sigma} = \frac{i\left(\frac{\omega}{2\pi}\right)\hat{r}}{15(1 + \hat{r})^2} \quad (2.13)$$

Where $\frac{\omega}{2\pi}$ is wavenumber in cm^{-1} and the magnetic permeability μ_1 is assumed to be one. Figure 2.8 shows the measured reflectivity (left panel) and the real part of the optical conductivity (right panel) for the Hg1201($T_c=67K$) sample obtained from the method explained above.

2. EXPERIMENTAL

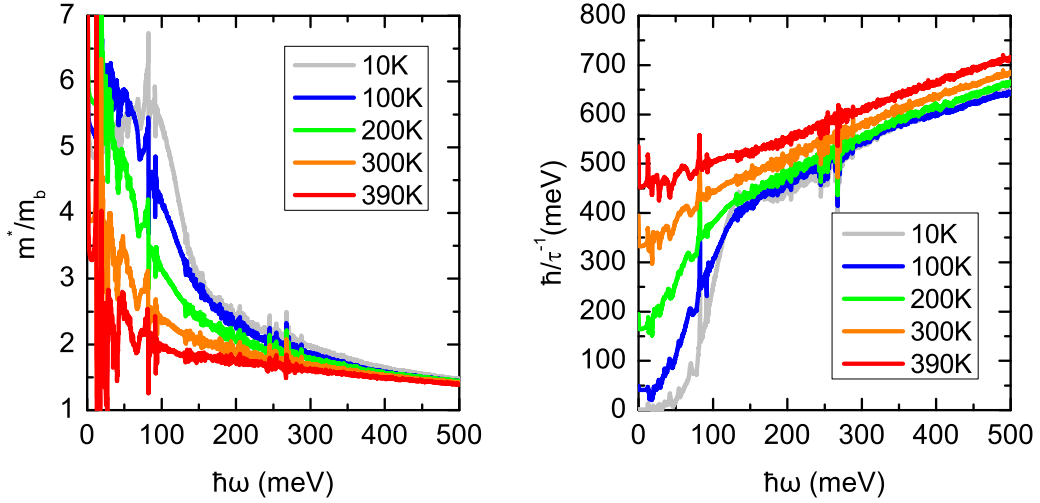


Figure 2.9: Frequency dependent mass enhancement and scattering rate for the Hg1201 ($T_c=67K$) sample calculated from extended Drude analysis.

2.4.2 Extended Drude analysis

As explained in section 1.4, the extended Drude formalism gives frequency-dependent scattering rate and enhanced mass. Figure 2.9 shows the frequency dependent scattering rate and enhanced mass for the Hg1201 ($T_c = 67K$) sample presented in this thesis.

The choice of plasma frequency ω_p is very important as it defines the relation between the optical conductivity and the memory function. If the interband transitions are well apart from the free-carrier response, one can use Eq. 1.45 to calculate the plasma frequency directly from conductivity. Another criterion for correct estimation of the plasma frequency is that the mass enhancement m^*/m_b has to tend to one (and not smaller) at high frequencies. In most cases, the interband transitions will contribute to the low frequency optical response and the correct calculation of the plasma frequency using the sum-rules will become a sensitive task which requires careful (if possible) separation between the free carrier response and the interband transitions. This can be done by applying the Drude-Lorentz model and only considering those oscillators that are assumed to represent the free carrier response. Another method would be to consider a cut-off frequency that acts as the higher limit of integral in equation 1.45.

Optical properties of Iron pnictides

3.1 Introduction

The discovery of superconductivity at $T_c = 26K$ in LaOFeAs in early 2008 [5] generated great excitement in high-temperature superconductivity (HTSC) society as it seemed to lead to understanding of the HTSC phenomena. This material belongs to the “oxypnictides” family that contain oxygen and one of the pnictogens (elements of group V). Many similar compositions were made by different labs all around the world with the hope of getting to higher T_c s in this family of compounds. Soon after, the T_c of about 55K was found in SmFeAsO_{1- δ} [6] which is now the highest among Iron-pnictides in bulk form (higher T_c for thin films is reported in Ref.[7]).

Iron pnictides do not fall within any class of superconductors that were known before 2008 (conventional SCs, copper oxides, heavy fermions, MgB₂, etc.) while they show similarities to each class [8]. In general, the phase diagram of Iron pnictides is a rich diagram that shares many properties with the one of cuprates (and heavy fermions). In both cases, a "superconducting dome" appears as a function of carrier doping or by applying pressure (or by isoelectronic substitution in case of pnictides [9]). In general, superconductivity seems to be competing with magnetism but co-existence of SC and magnetic states has also been reported [10, 11, 12]. In terms of magnetism, pnictides are similar to cuprates in that they both have a magnetic ground state in their parent compounds (no doping). On the other hand, in contrast to cuprates which have insulating parent compounds, pnictides have metallic parent compounds. In terms of correlations, electrons in pnictides are assumed to be weakly correlated [13, 14](although weaker than cuprates) which makes pnictides closer to cuprates than

3. OPTICAL PROPERTIES OF IRON PNICTIDES

to conventional superconductors and MgB_2 where nearly free-electron physics is ruling. Finally, pnictides have two sets of Fermi surfaces [15] similar to the case of MgB_2 [16]. An interesting difference between pnictides and cuprates is that, unlike in the cuprates, where electron (or hole) doping of the parent compound is a prerequisite of superconductivity, the parent compounds of pnictides can become superconducting by applying physical pressure [17, 18, 19] or chemical isovalent substitution (internal pressure) [20, 21]. However, charge doping (like substituting Iron with non-magnetic elements [22, 23]) can induce superconductivity as well. In general, it seems that superconductivity emerges as soon as magnetism is suppressed [24]. An extensive review of pnictides and their properties is found in Ref.[25].

Optical properties of pnictides provide us with valuable information that will help us understand the mechanism of superconductivity in these materials [26, 27]. Hence, in this chapter, the optical response of $\text{SmO}_{1-x}\text{F}_x\text{FeAs}$ family of iron-pnictides (oxypnictides with iron) for different doping levels will be presented as a first attempt to optically characterize this family of pnictides with highest T_c among pnictides (referred to as the 1111 family). Later in this chapter, the results of a systematic study on $\text{SrFe}_{2-x}\text{Co}_x\text{As}_2$ as a function of cobalt (electron) doping are presented. The results will be compared with $\text{Fe}_{1.087}\text{Te}$ chalcogenide that has a different magnetic ground state. The possible observation of an optical signature of quantum criticality in the $\text{SrFe}_{2-x}\text{Co}_x\text{As}_2$ family will be discussed.

3.2 Optical Properties of $\text{SmO}_{1-x}\text{F}_x\text{FeAs}$

The $\text{SmO}_{1-x}\text{F}_x\text{FeAs}$ samples were made using a conventional solid state reaction as described elsewhere [28]. The reflectivity of $\text{SmO}_{1-x}\text{F}_x\text{FeAs}$ poly-crystals with the grain size of 5-30 μm [29] and doping levels of $x = 0.12, 0.15$ & 0.2 was measured in the 3-75 meV energy range for temperatures above and below the critical temperature. The critical temperatures can be estimated from resistivity measurements (see figure 3.1) to be about 20 K, 39 K and 45 K for $x = 0.12, 0.15$ & 0.2 respectively. Since the samples came in polycrystalline form with a mixture of different crystal orientations at a relatively porous surface, we chose not to polish or manipulate the surface for optical experiments.

The reflectivity was obtained using a gold mirror as a reference as shown in figure 3.2. The proximity of R to one at low energies is an indication of metallic behavior that

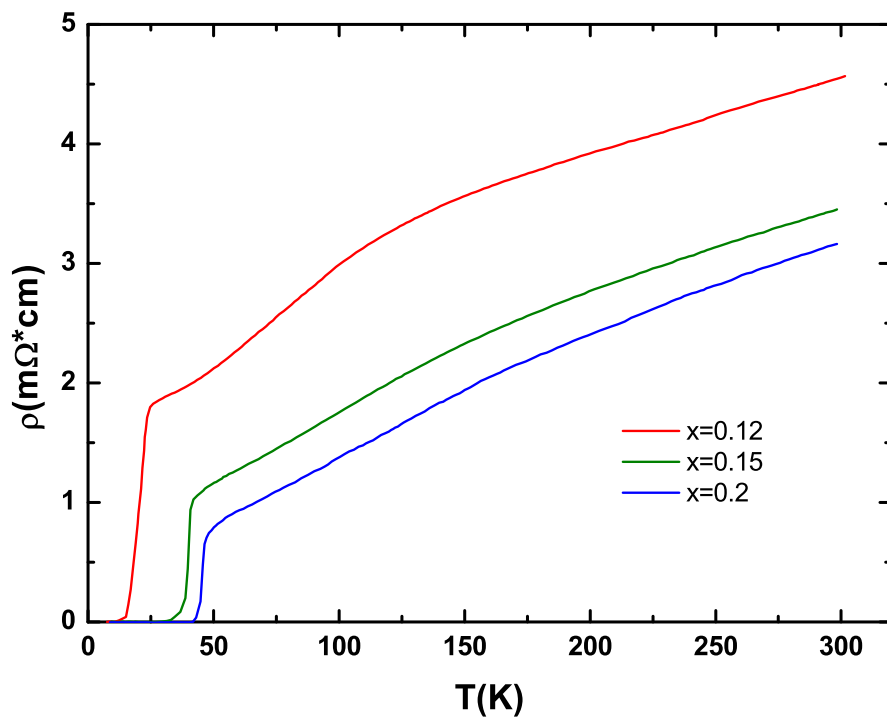


Figure 3.1: The resistivity of the $\text{SmO}_{1-x}\text{F}_x\text{FeAs}$ samples with different doping as a function of temperature.

3. OPTICAL PROPERTIES OF IRON PNICTIDES

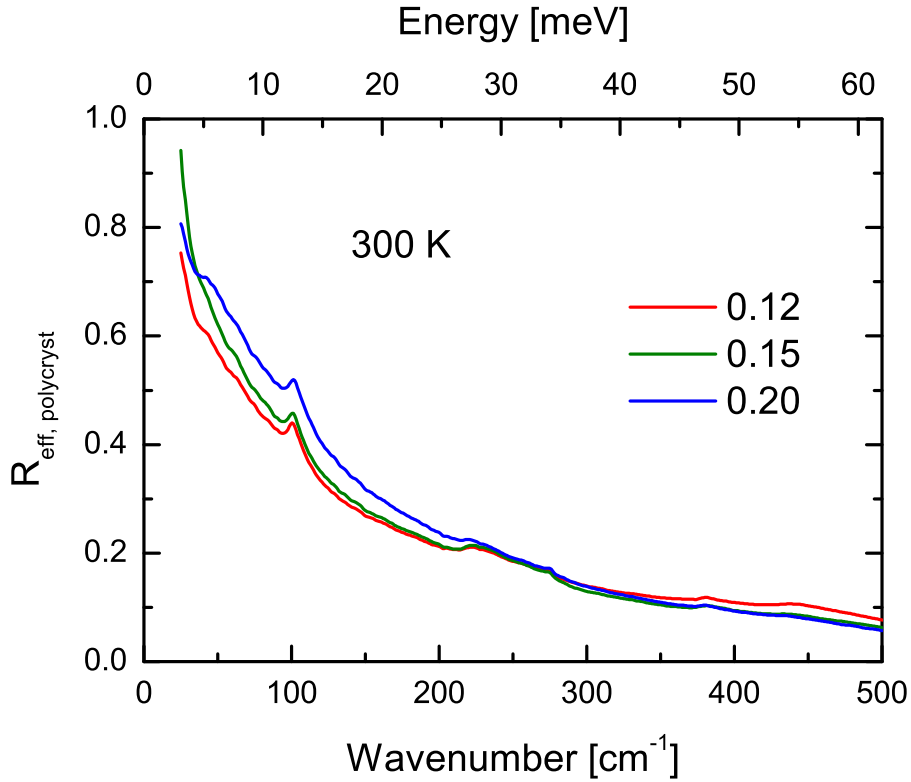


Figure 3.2: Reflectivity of polycrystalline unpolished samples of $\text{SmO}_{1-x}\text{F}_x\text{FeAs}$ with doping levels $x = 0.12, 0.15$ and 0.2 . The effective reflectivity is reduced due to diffuse surface light scattering and possible anisotropy of optical response.

also reveals itself as an overall increase in reflectivity with increasing the doping level. This trend agrees with resistivity measurements shown in figure 3.1. The reflectivity measured by this method is not accurate and is assumed to be lower than reflectivity of a single crystal for the following reasons. First, because of the polycrystalline form of the sample, there are both ab-plane and c-axis crystal orientations on the surface that contribute differently to optical response. It is also likely that the c-axis conductivity is much smaller than the one parallel to the planes, as suggested by experiment [30, 31], which is similar to cuprates. We note that high quality single crystals of sufficient thickness to show the c-axis response are not available, so the polycrystals are the only way to observe c-axis properties. The second reason is the diffuse light scattering on a rough sample surface, which is enhanced at higher frequencies. One can

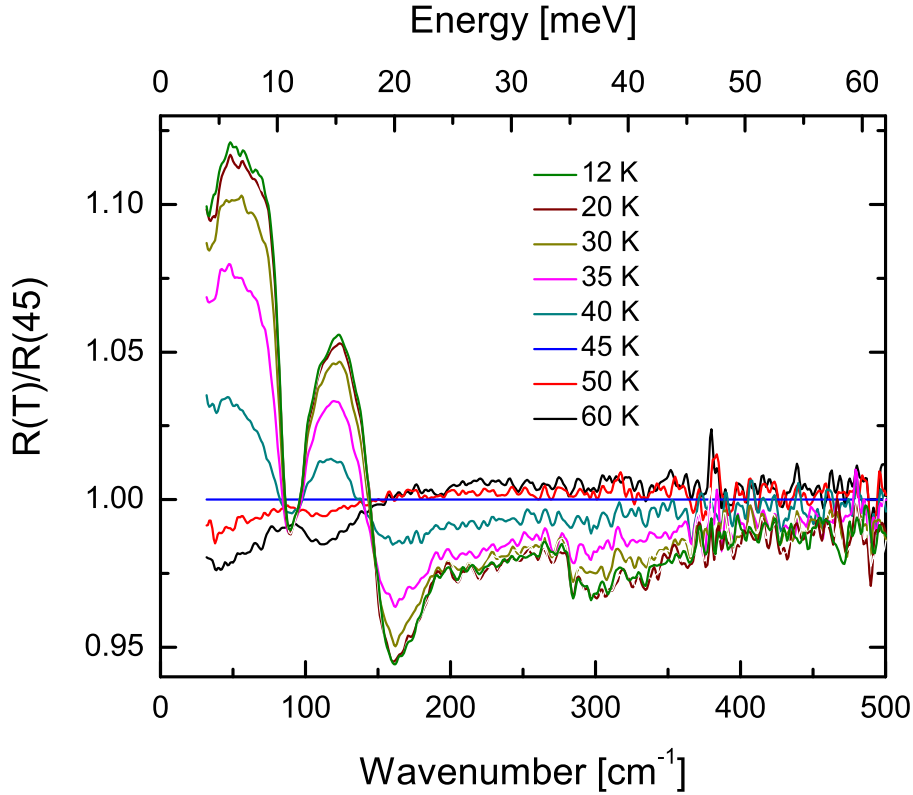


Figure 3.3: Reflectivity ratio for the sample with $x=0.2$ for different temperatures. All reflectivity graphs are divided by the reflectivity at 45 K. Two major features are observed at around 11 meV and around 19.8 meV. The peak at 14.9 meV is believed to belong to a phonon.

recognize a few phonon peak structures at 12 meV, 27 - 34 meV, 47 meV and 55 meV. The positions of these peaks are in agreement with previous optical measurements on $(\text{Nd,Sm})\text{FeAsO}_{0.82}\text{F}_{0.18}$ [30], $\text{LaFeAsO}_{0.9}\text{F}_{0.1}$ [32] and CeFeAsO [33].

In order to see the effect of the superconducting transition on the infrared response, we plot in figure 3.3 the reflectivity ratio $R(T)/R(45\text{K})$ for the $x = 0.2$ sample at several temperatures between 12 and 60 K. Below $T_c = 45\text{K}$ the reflectance strongly changes, and the reflectivity ratio shows a complicated frequency dependence. In the superconducting state, the reflectivity ratio increases below 18 meV reaching a maximum value of 1.12 at about 7 meV and lowers at higher photon energies, showing a pronounced dip at 20 meV. This behavior agrees with the Mattis-Bardeen model

3. OPTICAL PROPERTIES OF IRON PNICTIDES

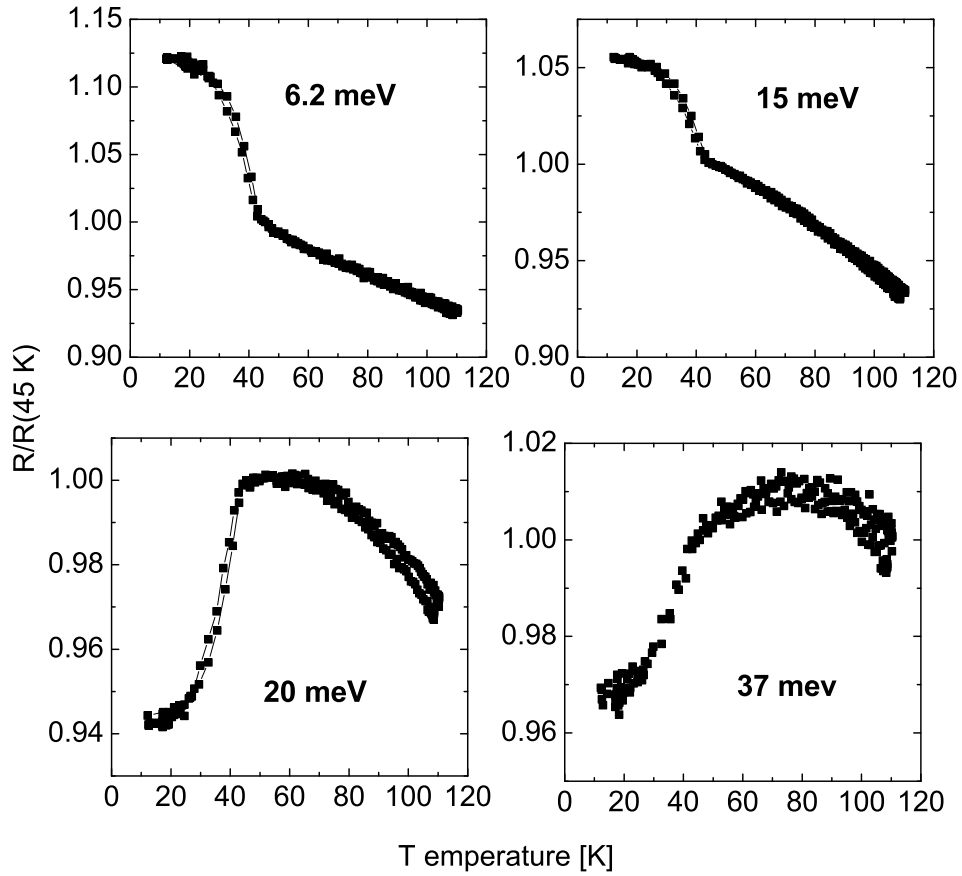


Figure 3.4: Temperature dependence of reflectivity ratio at 4 different energies for $\text{SmFeAsO}_{0.8}\text{F}_{0.2}$.

for a BCS superconductor, but would also be consistent with the appearance of a strong plasma mode due to the condensate. As in the earlier infrared experiments on polycrystalline samples of the high- T_c cuprates [34] it is difficult to distinguish between these two possibilities. In the first scenario, the value of the 2Δ can be very roughly estimated to be between 10 and 20 meV, which would not be inconsistent with the weak-coupling BCS gap ratio, observed in a point-contact tunneling measurement [28]. However, from independently measured reflectivity of ab-plane of single crystals [35] of 122 family, we now know that the 10% change in reflectivity shown in Fig.3.4 most likely originates in the c-axis which supports the scenario for a strong Josephson plasmon. In Fig.3.4, the temperature dependence of the reflectivity ratio

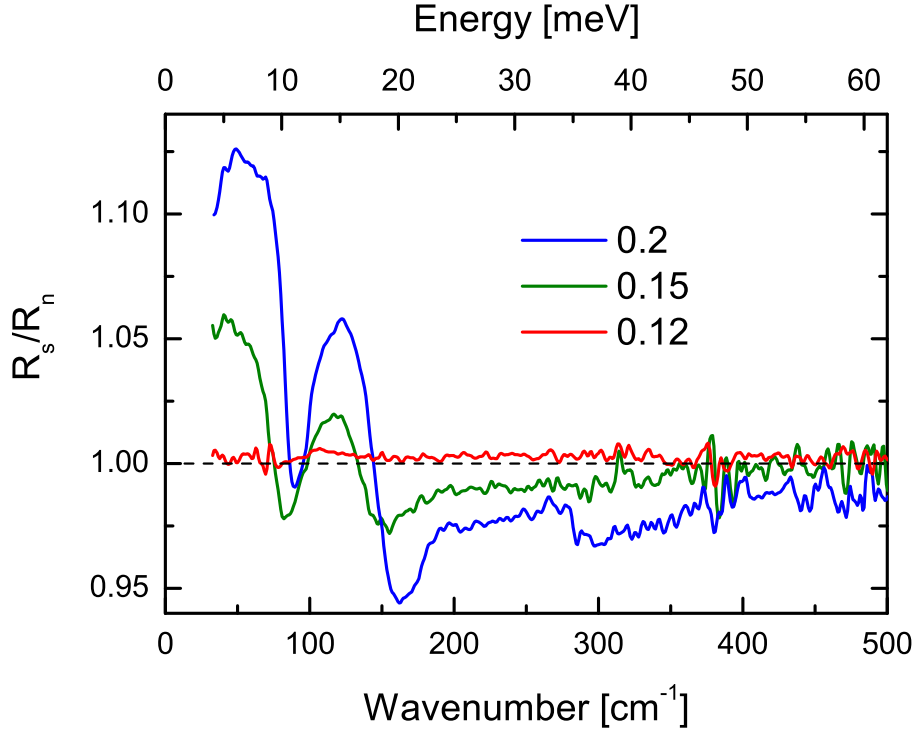


Figure 3.5: Reflectivity ratio R_s/R_n for samples with doping levels of 0.12, 0.15 and 0.2. R_s is taken at 12 K, R_n - at T_c .

is shown for four different photon energies (6.2, 15, 20 and 37 meV). A sharp upward kink at T_c is observed at low energies. The curve at higher energies also show a clear kink in the opposite direction. Fig. 3.5 shows the reflectivity ratio for three different doping levels as mentioned before. Comparing to the highest doping of 0.2, we see that for $x=0.15$ and 0.12 the low energy structures have strongly reduced in intensity and also have slightly shifted to lower frequencies. For $x=0.12$, almost no effect of the superconducting transition is discernible. It is interesting to compare the superconducting-to-normal state reflectivity ratio spectra for polycrystalline samples from different families of superconductors, which have though a similar value of T_c . Fig. 3.6 presents R_s/R_n of $\text{SmFeAsO}_{0.8}\text{F}_{0.2}$ ($T_c = 45$ K), $\text{La}_{1.85}\text{Sr}_{0.15}\text{CuO}_4$ ($T_c = 37$ K) [36] and MgB_2 ($T_c = 40$ K) [37]. Note that here the spectra of $\text{La}_{1.85}\text{Sr}_{0.15}\text{CuO}_4$ were calculated using the effective medium approximation [38] based on the ab-plane and c-axis dielectric functions, obtained on single crystals. We see that the spectral range

3. OPTICAL PROPERTIES OF IRON PNICTIDES

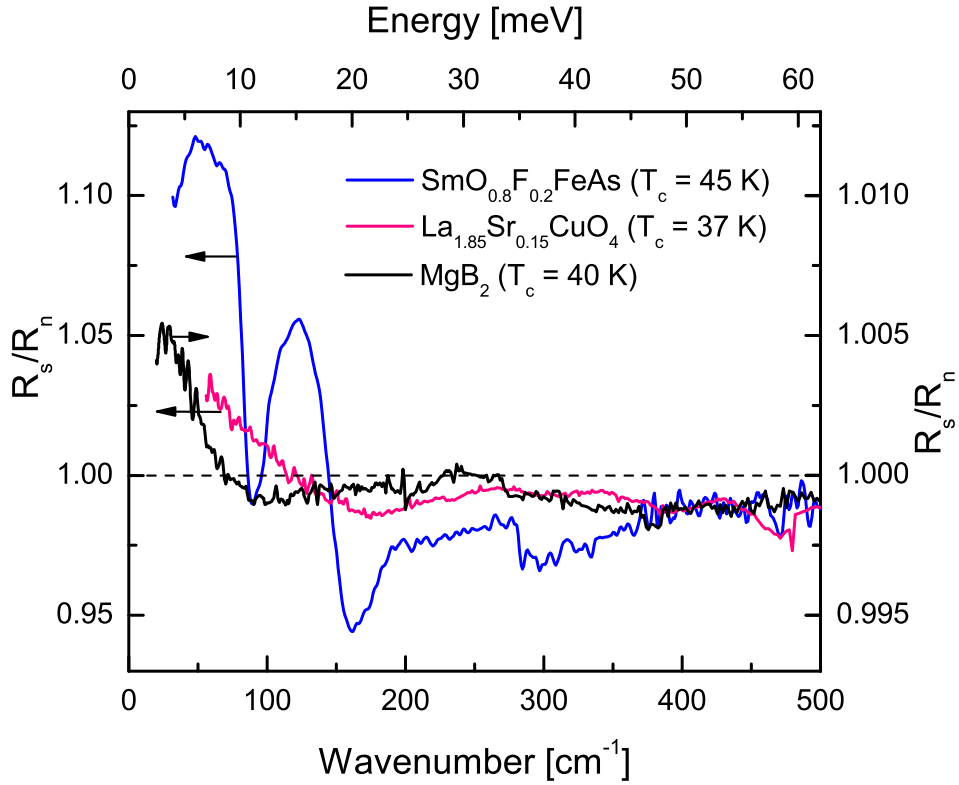


Figure 3.6: The spectra of R_s/R_n for three different superconductors with similar values of T_c .

where the superconductivity induced changes are clearly observed in the iron arsenide superconductors is quite broad and comparable with the one in $\text{La}_{1.85}\text{Sr}_{0.15}\text{CuO}_4$. We also notice that this range is much narrower in MgB_2 . Of course, the difference might be due to many reasons, for example different gap symmetry, optical anisotropy etc.

3.3 Optical Properties of $\text{SrFe}_{2-x}\text{Co}_x\text{As}_2$

3.3.1 Sample Preparation

Large samples of $\text{SrFe}_{2-x}\text{Co}_x\text{As}_2$ with $x = 0, 0.12, 0.20$ ($T_c = 0, < 10\text{K}, 15\text{K}$) were grown using the flux method [39]. As mentioned in section 2.2, surfaces of these crystals can be prepared using scotch-tape cleaving. One advantage of cleavage

is that the obtained surface is fresh (less exposed to air) and shiny which makes it appropriate for optical measurements. The usual sample sizes used in measurements were around $2 \times 2 \text{ mm}^2$ that is enough for getting high optical SNR (signal to noise ratio) for short acquisition times. The samples were mounted on a copper cone using silver paste. In some cases, the samples needed to be cleaved several times during the optical measurements in order to get the reference gold layer off. This -in some cases- introduced some (minor) mismatch among optical data of different frequency ranges.

3.3.2 Optical measurements

In this section, the two methods of obtaining optical spectra are explained. For the far-near infrared range (6-740 meV), we used an FTIR spectrometer (Bruker IFS 113v) in normal angle reflection mode to measure optical response of the crystals. For the range of 0.74-5 eV, an ellipsometer was used.

3.3.2.1 Reflectivity

We used a high vacuum (HV) optical cryostat with changeable window for the reflectivity measurements. A poly-ethylene (PE) window was used for the 6-86 meV range using a bolometer as detector and a KBr window was used for the 50-740 meV range using MCT as detector. The typical pressure in the HV cryostat was 10^{-6} - 10^{-5} Torr which -for some samples- is not the ideal vacuum to avoid water absorption at low temperatures. The temperature range covered by our HV cryostat was 15-300K. Two gold evaporation units can be used at the same time in this cryostat to ensure a successful evaporation. In-situ gold evaporation at room temperature was used in order to measure absolute reflectivity. Figure 3.7 shows the reflectivity for three doping levels of $x = 0, 0.12$ & 0.20 .

3.3.2.2 Drift Corrections

As explained before, there always is some drift (over time) in the signal amplitude coming from several sources of instability. At the time of experiments with $\text{SrFe}_{2-x}\text{Co}_x\text{As}_2$ samples, no systematic way of drift correction has been developed. We therefore, assumed a linear drift in time using the amplitude at the high temperature in the beginning and the end of the thermal cycle. This type of correction does not work in case of

3. OPTICAL PROPERTIES OF IRON PNICTIDES

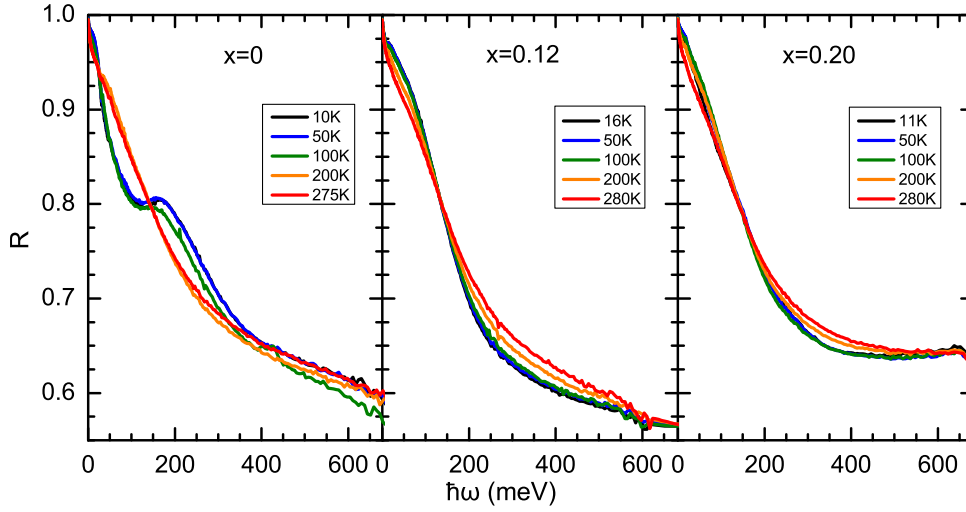


Figure 3.7: Measured reflectivity of the $\text{SrFe}_{2-x}\text{Co}_x\text{As}_2$ for $x = 0, 0.12, 0.20$.

non-linear time drifts that may happen during the experiment. So, extra caution was taken when applying such corrections.

3.3.2.3 Ellipsometry

Ellipsometry was used for measurements of optical data in the 0.74-5 eV range. Based on measurements at mid-infrared range, we assumed temperature independent optical properties at high frequencies and sufficed only to the room temperature data. We have also assumed low anisotropy in optical data for $\text{SrFe}_{2-x}\text{Co}_x\text{As}_2$ samples based on the reported c-axis measurements [40].

3.3.3 Data analysis

In this section, the methods used to calculate the optical constants will be explained.

3.3.3.1 Complex optical constants

The complex optical dielectric function and conductivity were calculated using the optical data analysis software “RefFIT” [41], through the following procedure: First, by simultaneous fitting of the reflectivity and ellipsometry data to the Drude-Lorentz model, we get an appropriate model for the optical data. Then, using the variational dielectric function (VDF) fitting method, we obtain the Kramers-Kronig consistent fit

3.3 Optical Properties of $\text{SrFe}_{2-x}\text{Co}_x\text{As}_2$

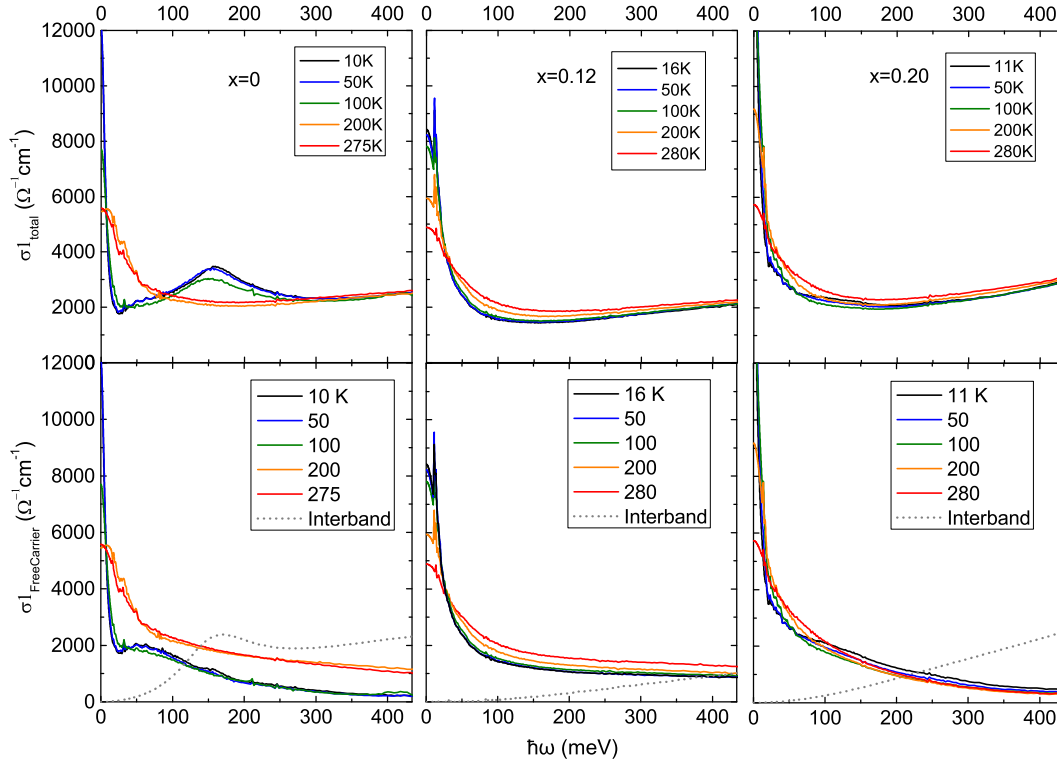


Figure 3.8: Optical conductivity for $\text{SrFe}_{2-x}\text{Co}_x\text{As}_2$ with $x = 0, 0.12, 0.20$. In the top three graphs, a background spectral weight is present which makes the extended Drude analysis difficult to interpret. To avoid this problem, the interband contribution (dashed lines) were subtracted from the total optical conductivity as shown in the three bottom graphs.

to the data which is -to a great precision- equivalent of directly performing the KK transformation. Figure 3.8 shows the resulting optical conductivity for three different doping levels of $\text{SrFe}_{2-x}\text{Co}_x\text{As}_2$.

3.3.3.2 Extended Drude analysis

The memory function was calculated using equation 1.42. To get proper values for scattering rate ($\gamma = \frac{1}{\tau}$) and the enhanced mass ($\frac{m^*}{m_b}$), we have subtracted the higher frequency Lorentzians from the original optical conductivity. What is left is considered to represent the coherent interband-free spectra which is used for a meaningful extended Drude analysis. Figures 3.9 and 3.10 show the enhanced mass and scattering rate for different doping levels.

From the enhanced mass graphs a common feature could be observed: the mass

3. OPTICAL PROPERTIES OF IRON PNICTIDES

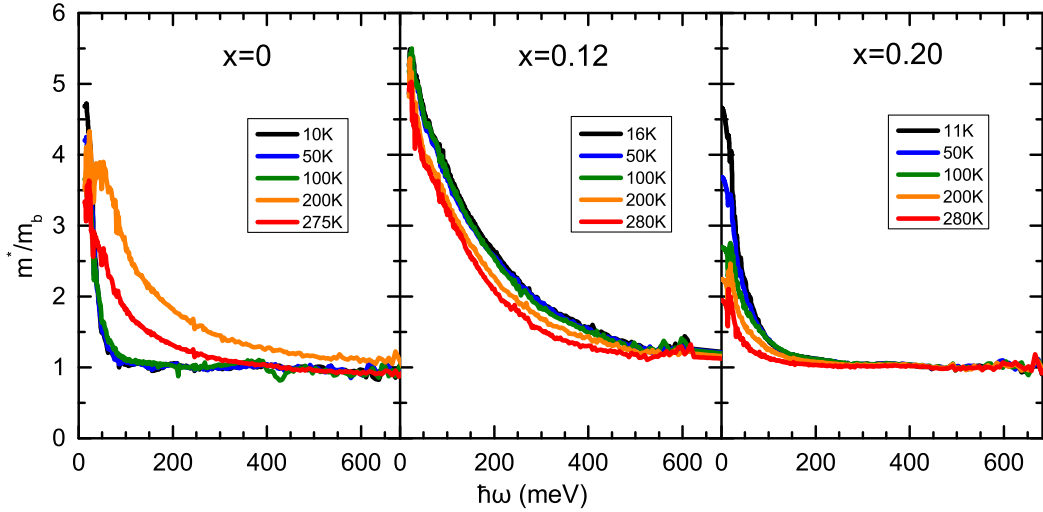


Figure 3.9: Enhanced mass for $\text{SrFe}_{2-x}\text{Co}_x\text{As}_2$ with $x = 0, 0.12, 0.20$. The values shown here are calculated after subtraction of the interband contribution from the optical conductivity. The variation of the low-temperature curves as a function of doping suggests a quantum critical transition.

enhancement reaches a maximum at low frequencies and low temperatures. A considerable change in width of mass enhancement is seen in the parent compound when it undergoes a magneto-structural transition at around $T_N=190\text{K}$. It can be seen from both enhanced mass and scattering rate figures that the temperature behavior of those properties has some anomalies: in the parent compound, above the magnetic transition temperature the mass gets narrower and the scattering rate decreases contrary to what one expects from metals. The same narrowing of the mass is also observed for the other two doped compounds. As it will be discussed in section 3.4, the great difference between optical parameters of the two doped samples is associated to quantum criticality. Another interesting observation is that for the $x = 0.12$ doping, the scattering rate has almost linear behavior as a function of both frequency and temperature. This is similar to the optimally doped cuprates [42].

3.3.4 Comparing 122 family of pnictides and 11 family of chalcogenides

The iron pnictide or chalcogenide systems have often been compared to the cuprates because of their proximity of magnetism to superconductivity. However, it is not clear

3.3 Optical Properties of $\text{SrFe}_{2-x}\text{Co}_x\text{As}_2$

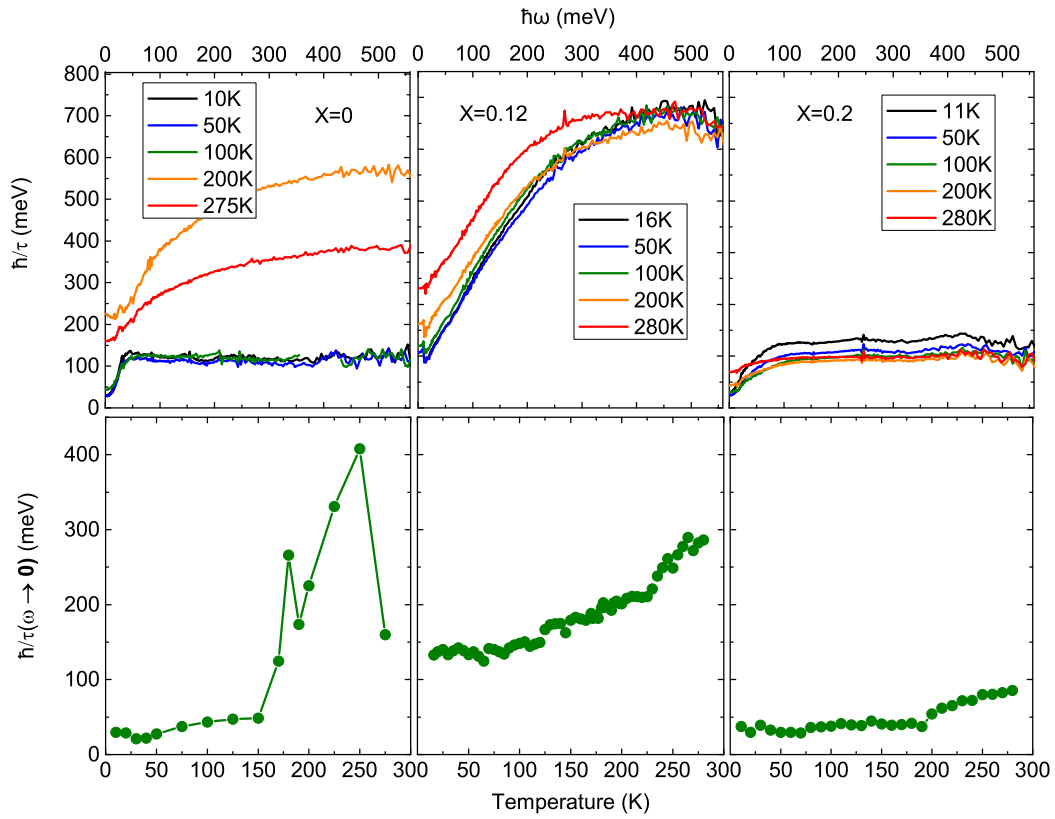


Figure 3.10: Top row: Scattering rate for $\text{SrFe}_{2-x}\text{Co}_x\text{As}_2$ with $x = 0, 0.12, 0.20$ after subtraction of interband contribution. Bottom row: Scattering rate at zero frequency limit as a function of temperature. For $x = 0.12$ the linear scattering rate in both frequency and temperature resembles the properties of optimally doped cuprates.

3. OPTICAL PROPERTIES OF IRON PNICTIDES

whether these two classes of iron systems belong to the same universality class, given the notably different magnetic-ordering pattern of the parent compound ground states. Below $T_{ms}=67$ K, the “11” chalcogenide $\text{Fe}_{1.087}\text{Te}$ undergoes a magneto-structural phase transition into a bidiagonal magnetically ordered ground state [Fig. 3.11(a)] with a large moment of $\sim 2\mu_B$ [43, 44, 45]. In contrast, the “122” pnictide $\text{SrFe}_{2-x}\text{Co}_x\text{As}_2$ with $T_{ms}=190$ K orders in a smaller moment, vertical-stripe pattern [46] as shown in Fig. 3.11(b), common to the parent compounds of the type XFe_2As_2 and related compounds isostructural to LaFePO . Both systems can be driven superconducting by chemical substitution [47, 48] and pressure[49, 17]. Formal valence counting gives the same nominal Fe valence while electronic structure[50, 51, 52] and angle-resolved photoemission (ARPES)[53, 54] results suggest topological equivalence to the Fermi surfaces in the high-temperature, paramagnetic phase.

Fig. 3.12(a) compares the strength $\omega_{p,1}^2$ of the narrow Drude component in each of the two systems. In each case, the value of the model $\omega_{p,1}^2$ has a steplike change at the magnetostructural transition and is almost independent of temperature for $T < T_{ms}$. This reflects the fact that the structural transitions are first order[43, 56] and the formation of electron and hole pockets occurs abruptly at T_{ms} , consistent with ARPES data on BaFe_2As_2 (Ref. [53]) and $\text{Fe}_{1.06}\text{Te}$. [57] The direction of the step at the transition T_{ms} is the clearest transport-related difference between these two systems: the carrier weight in the 122 system decreases with the onset of magnetic order but the carrier weight of the 11 system increases. This behavioral difference arises from the diverse magnetic-ordering pattern, which has profoundly different effects on zone folding (Fig. 5 of Ref. [55]) and therefore also the topology of the low-temperature Fermi surfaces.

3.4 Quantum Criticality in $\text{SrFe}_{2-x}\text{Co}_x\text{As}_2$

3.4.1 Introduction

As mentioned earlier in this chapter, the phase diagram of iron pnictides is similar to the one of the cuprates in that both have magnetic ground state in their parent compounds. The disappearance of magnetic order as a function of non-thermal control parameters (like pressure) and emergence of superconductivity at the vicinity of this magnetic phase transition brings the idea of possible existence of quantum criticality

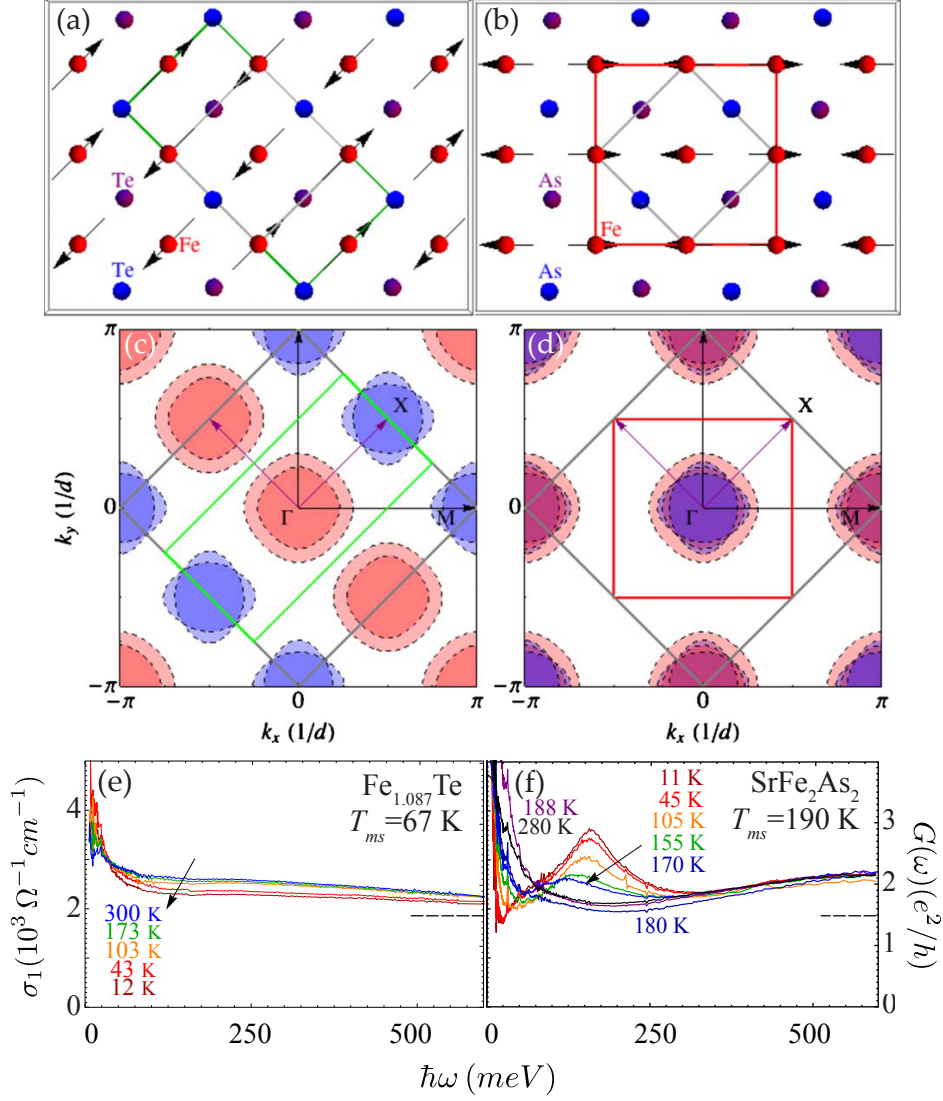


Figure 3.11: Low-temperature magnetic structure of (a) $\text{Fe}_{1.087}\text{Te}$ and (b) SrFe_2As_2 . [(c) and (d)] Fermi-surface folding expected from the lowered structural symmetry. Optical conductivity $\sigma_1(\omega, T)$ of (e) $\text{Fe}_{1.087}\text{Te}$ and (f) SrFe_2As_2 crossing their magnetostructural phase transition. Dashed lines indicate expectation from Dirac cone $G(\omega) = \sigma_1(\omega)d$. Figure from Ref. [55].

3. OPTICAL PROPERTIES OF IRON PNICTIDES

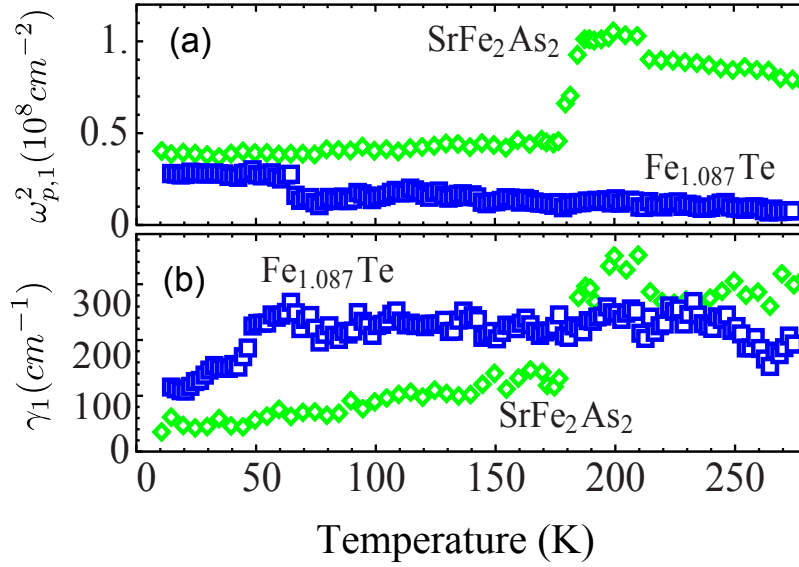


Figure 3.12: Comparison of the (a) strengths and (b) widths of the narrow Drude contributions for each of the two systems. Figure with modifications from Ref. [55]

in pnictides. Here, we briefly study the possible connection between optical properties of SrFe_{2-x}Co_xAs₂ family and quantum criticality.

3.4.2 Quantum criticality

The change in the energy of a system at absolute zero temperature is governed by quantum fluctuations due to Heisenberg’s uncertainty principle. A “Quantum phase transition” is a change in the ground state of a system due to change in physics of its zero-point (quantum) fluctuations. This type of phase transition is possible through tuning parameters such as magnetic field, pressure or doping. Quantum phase transitions are second-order phase transitions where the change in entropy is continuous and phases are separated by the so called “Quantum Critical Point” in the tuning parameter space. Quantum criticality has become one of the important subjects in condensed matter physics. Strongly correlated materials such as heavy Fermions [58, 59, 60, 61], High- T_c cuprates [62, 63, 64] and iron arsenides [65, 66, 67, 61] are shown to behave like quantum critical systems; an idea that is also supported by theory [68, 69, 70, 71].

3.4.3 The case of 122 family

In the 122 family, there are two different types of substitution that lead to a change in the ground state: 1-The isovalent(or isoelectronic) chemical substitution such as As with P [72, 73], Fe with Ru [74, 75, 76] or Ba with Sr[77]) and 2-The carrier (electron or hole) doping like substituting Fe with Ni [78] or Co [23] for electron doping and with K [79, 80] for hole doping). Isovalently doped 122 system is preferred over charge doped one since it is a cleaner system and covers a wider range of doping. However, the electron(hole)-doped systems also show similar behavior in their phase diagram [66, 67].

The case of $\text{SrFe}_{2-x}\text{Co}_x\text{As}_2$ falls within the second category with electron doping achieved through addition of Cobalt ions. The general characteristic of this system is very similar to the widely studied case of $\text{BaFe}_{2-x}\text{Co}_x\text{As}_2$. Having lighter Sr ions instead of Ba leads to a higher magnetic (and structural) phase transition temperature of around $T_N = 190\text{K}$ (instead of 135K in case of Ba ion). In both cases, two phonons at around 12 and 32 meV are observed in optical spectra [81, 35].

An effort to extract the phase diagram of $\text{SrFe}_{2-x}\text{Co}_x\text{As}_2$ family is done in Ref.[23] which is also shown in Fig.3.13. According to this phase diagram, the quantum critical point should be around doping level of $x = 0.18$. One should note that x here is calculated according to the notion in $\text{SrFe}_{2-x}\text{Co}_x\text{As}_2$ which is a factor of two higher than in $\text{Sr}(\text{Fe}_{1-x}\text{Co}_x)_2\text{As}_2$ used in Ref.[23]. Therefore, the data shown in previous section for $\text{SrFe}_{2-x}\text{Co}_x\text{As}_2$ are likely to be corresponding to magnetic (for $x = 0$ & 0.12) and quantum critical states (for $x = 0.2$) of Sr122 family. The considerable difference in scattering rate and normalized mass of the two doped compounds is most likely due to the difference in their quantum phases.

3. OPTICAL PROPERTIES OF IRON PNICTIDES

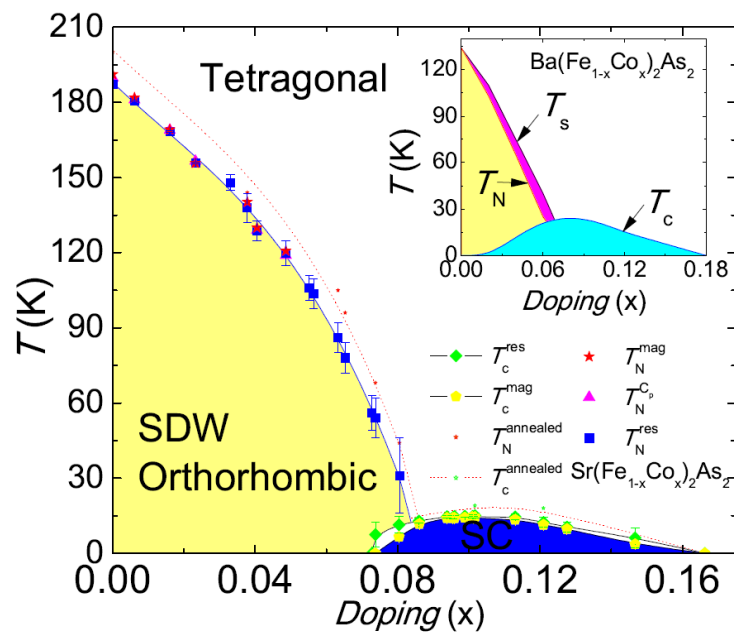


Figure 3.13: Phase diagram of the Sr(Fe_{1-x}Co_x)₂As₂. Inset shows the phase diagram of the Ba(Fe_{1-x}Co_x)₂As₂ in the inset. Figure from ref.[23]

Optical properties of under-doped $\text{HgBa}_2\text{CuO}_{4+\delta}$

4.1 Introduction

The $\text{HgBa}_2\text{Ca}_{n-1}\text{Cu}_n\text{O}_{2n+2+\delta}$ family of high T_c superconductors are very interesting materials to study because of their record T_c as well as their high crystal symmetry. The simplest member of this family is the $\text{HgBa}_2\text{CuO}_{4+\delta}$ (Hg1201) with one copper-oxygen sheet per unit cell as shown in Fig. 4.1. The optical measurements on these materials have become possible recently after a breakthrough in the growth of high purity large single crystals [82]. In this chapter, the details of the optical measurements on under-doped Hg1201 samples will be explained.

4.2 Sample preparation

Single crystals of $\text{HgBa}_2\text{CuO}_{4+\delta}$ (Hg1201) were grown using a flux method, characterized and heat treated to the desired doping level as described in Refs. [82] and [83]. The crystal surface is oriented along the ab plane with an area of about $1.51 \times 1.22 \text{ mm}^2$. For contact, samples were mounted on the tip of a copper cone using silver paste as explained in chapter 2. Special care was taken to glue the sample as strong as possible to the holder. The strong contact is needed because we may need to polish the sample several times while it is still mounted on the cone.

For surface preparation of mercury-based cuprates, scotch-tape cleaving does not

4. OPTICAL PROPERTIES OF UNDER-DOPED $\text{HgBa}_2\text{CuO}_{4+\delta}$

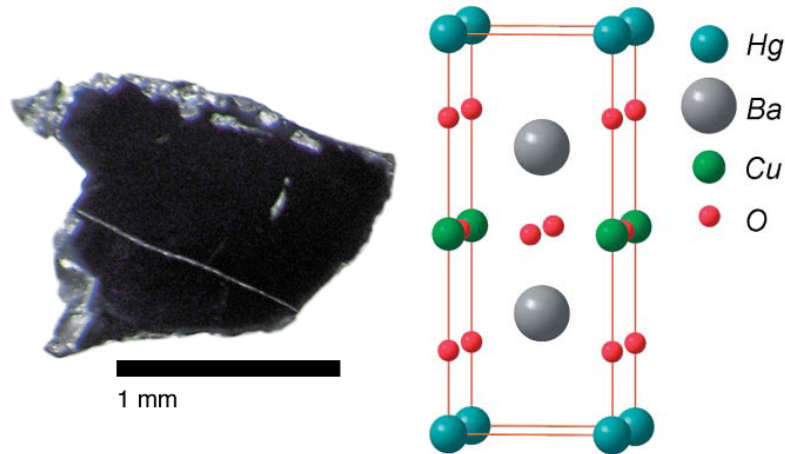


Figure 4.1: Left: A photo of the sample after polishing. Right: The crystal structure of the $\text{HgBa}_2\text{CuO}_{4+\delta}$ compound.

work and mechanically stronger methods are needed (like using a blade to cleave) by which there is high risk of damaging or losing the sample. To avoid this problem, we have chosen to polish our crystals using dry abrasive with grain size of around $0.1 \mu\text{m}$ after each measurement. As it will be shown, failure in polishing the sample exactly parallel to ab-plane (as well as crystal structure disorder) may introduce a c-axis contribution to the optical data. This problem can be avoided using a polarizer at the cost of losing part of the signal intensity. As Hg1201 samples are hygroscopic, the last stage of the preparation of the sample surface was done under a continuous flow of nitrogen, after which the sample was transferred to a high vacuum chamber (10^{-7} torr) within less than a few minutes. Before each measurement, the surface was carefully checked for any evidence of oxidation.

It should be reminded that the process of collecting optical data consist of several measurements during each we have to deposit a layer of gold on the sample. Therefore, we have to remove the gold layer before next measurement. This is usually done using a scotch tape and as seen in practice, will not work all the time depending on how strongly the film is stuck to the sample. So, in some cases we have to polish the surface in order to get the gold layer off.

4.3 Optical measurements

Two methods of measuring optical spectra were used in this experiment: (near) normal incident reflectivity and ellipsometry.

4.3.1 Reflectivity

For the far and near infrared range (6 meV-1.2 eV), we used a Bruker 113 FTIR spectrometer (Fig. 2.1) in reflection mode to measure the optical response of the sample. For measurement of the c-axis response within the range of (60 meV-1.4 eV), a microscope-equipped FTIR spectrometer (Bruker VERTEX 70V) was used.

We used a home-made UHV optical cryostat with a diamond window for the reflectivity measurements. The temperature range covered by this cryostat was 10-400K. The typical pressure for measurements with this cryostat was 10^{-9} - 10^{-6} torr depending on many parameters such as pre-baking, o-ring sealing and temperature of the parts. The cryostat is equipped with an ion gauge and an ion pump. It also accommodates two gold evaporation units and can be baked for ultra high vacuum applications.

In order to obtain the absolute value of the reflectivity, we normalized the measured reflectance by the reflectance of a gold layer deposited on the sample. We have used twisted tungsten wires to hold and evaporate gold wires. Usually a power of around 50 Watts is needed for about 15 seconds to perform the evaporation.

There is always a chance of having c-axis optical response in our data due to the possible miscut caused by inaccurate polishing of the surface or because of having crystal distortion. This shows up as strong c-axis phonon contributions at frequencies around 19.2 meV, 52.7 meV and 80.6 meV as shown in figure 2.2. The c-axis contribution effect is more difficult to observe at higher frequencies because the c-axis reflectivity has no features and is almost constant there. A very effective way to correct for this effect is to use polarizers that polarize the light in a direction parallel to the direction of miscut lines on the surface.

The sample was cooled down from 395K to 10K at a speed of 0.9 K/min leading to about one reflectivity spectrum per Kelvin. In order to increase the signal to noise ratio, the data were averaged over 10K temperature intervals.

To correct for the signal drifts caused by instabilities of sources and detectors, a calibration reference mirror was used (Fig. 2.4). The corrected reflectivity is obtained from the relation:

4. OPTICAL PROPERTIES OF UNDER-DOPED HGBA₂CUO_{4+δ}

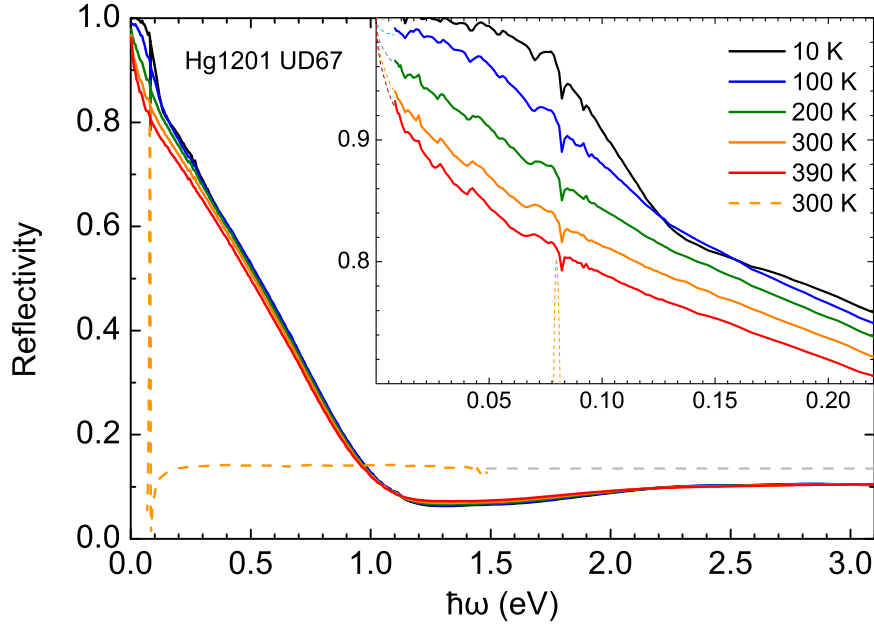


Figure 4.2: Optical reflectivity of Hg1201 UD67 along the ab-plane (solid lines) and c-axis (dashed line) at selected temperatures. A strong phonon mode is observed in both a and c axis at 82 meV. The inset shows the far infrared reflectivity where it is also possible to see the remaining of a suppressed c-axis phonon at 70 meV.

$$R(\omega) = \frac{I_{sample}(\omega)}{I_{gold}(\omega)} \cdot \frac{I_{gold-calib.-mirror}}{I_{sample-calib.-mirror}} \quad (4.1)$$

Figure 4.2 shows the measured reflectivity along both a(b) and c axis. It is important to note that an ab plane phonon exists at around 80 meV that should be distinguished from the closely located c-axis phonon.

4.3.2 Ellipsometry

Ellipsometric measurements were performed in the near-IR to near-UV (0.75-4.3 eV) using a Woolam VASE[®] ellipsometer with an angle of incidence set at 61 degrees relative to the surface normal vector, providing (after inversion of the Fresnel equations) the so-called pseudo dielectric function:

$$\epsilon_{ps}(\omega) = \sin^2\theta + \sin^2\theta \left(\frac{\sqrt{\epsilon_{ab} - \sin^2\theta} \sqrt{\epsilon_{ab}} - \sqrt{1 - \epsilon_c^{-1} \sin^2\theta}}{\sqrt{\epsilon_{ab} - \sin^2\theta} \sqrt{1 - \epsilon_c^{-1} \sin^2\theta} - \sqrt{\epsilon_{ab} \cos^2\theta}} \right)^2 \quad (4.2)$$

where ϵ_{ab} and ϵ_c are the dielectric tensor elements in the ab-plane and along the c-axis respectively. The dashed curves in Fig. 4.3 represent the pseudo dielectric function measured at 300 K. In the limit of zero anisotropy ($\epsilon_{ab} = \epsilon_c$) the pseudo-dielectric function equals the dielectric function ($\epsilon_{ps} = \epsilon_{ab}$). We calculate the ab dielectric function by fitting the measured pseudo-dielectric function, ab-plane and c-axis reflectance simultaneously to a Drude-Lorentz model. The resulting ab-plane dielectric functions are shown in Fig. 4.3 for a few selected temperatures. The reflectance and phase spectra were calculated in this data range using the Fresnel expression for normal incidence reflectivity. A perfect match was obtained where the ellipsometry and normal incidence reflectance data overlap (0.8-1.2 eV). The complex dielectric constant was obtained by standard Kramers-Kronig transformation of the reflectance data, using the reflectance and phase data between 0.8 and 3.7 eV to fix the high frequency extrapolation. This procedure anchors the phase output of the Kramers-Kronig transformation in the entire frequency range to the experimental data between 0.8 and 3.7 eV.

4.4 Drude-Lorentz analysis

In order to characterize the oscillator strengths and frequencies corresponding to the interband transitions, we have fitted to the experimental conductivities a linear superposition of Drude and Lorentz oscillators:

$$\epsilon(\omega) = 1 + S_h + \sum_{j=0}^N \frac{\omega_{pj}^2}{\omega_j^2 - \omega(\omega + i\gamma_j)} \quad (4.3)$$

where S_h summarizes the dielectric polarizability originating in oscillators at frequencies higher than the $j=7$ mode at 5.2 eV. The dielectric function is understood to represent the superposition of the conduction electron (or hole) optical conductivity and the “bound charge” response:

$$\epsilon(\omega) = \frac{4\pi i}{\omega} \sigma_f(\omega) + \epsilon_b(\omega) \quad (4.4)$$

4. OPTICAL PROPERTIES OF UNDER-DOPED HGBA₂CUO_{4+δ}

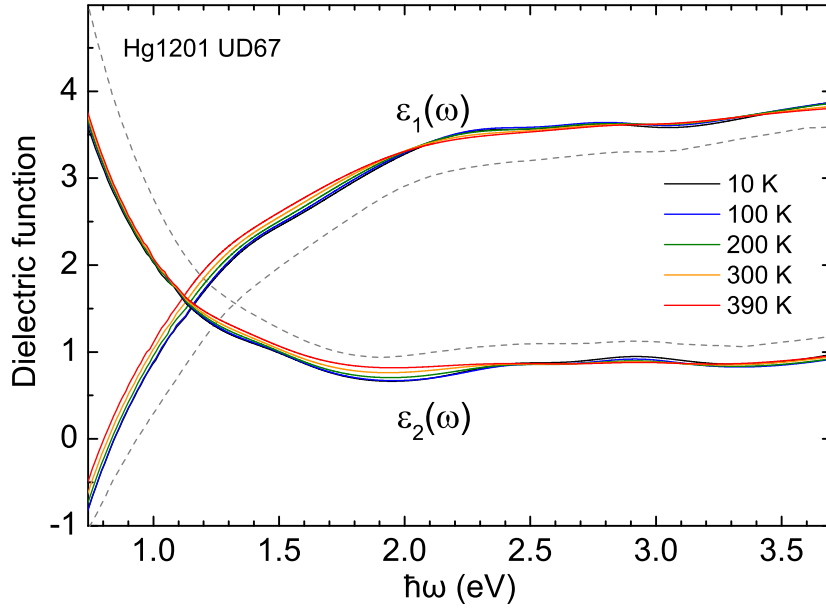


Figure 4.3: Real and imaginary parts of the pseudodielectric function (dashed curves) obtained from ellipsometry at room temperature, and ab-plane dielectric function at selected temperatures corrected using the method explained in the text.

The optical conductivity is shown in Fig. 4.4, together with the Drude-Lorentz fit. The corresponding parameters are summarized in Table 4.1.

Table 4.1: Parameters of the Drude-Lorentz oscillators displayed in Fig.4.4. S_h is dimensionless. The parameter values corresponding to $\hbar\omega_p$, $\hbar\omega_0$, and $\hbar\gamma$ are in units of eV.

	j=0	j=1	j=2	j=3	$\hbar\omega_p$	j=4	j=5	j=6	j=7	S_h
$\hbar\omega_{0,j}$	0	0.116	0.542	0.908		1.443	2.430	2.939	5.204	
$\hbar\omega_{p,j}$	0.857	1.461	0.969	0.638	2.053	0.444	0.947	0.510	4.390	2.2
$\hbar\gamma_j$	0.046	0.337	0.747	0.805		0.598	1.126	0.636	2.723	

4.5 Conduction band and bound charge contributions

Here we will interpret all oscillators below 1.2 eV as an intrinsic part of the conduction band response. The interpretation of the weak green peak at 1.4 eV is uncertain. Since the spectral weight is very small, it makes next to no difference for the discussion

4.5 Conduction band and bound charge contributions

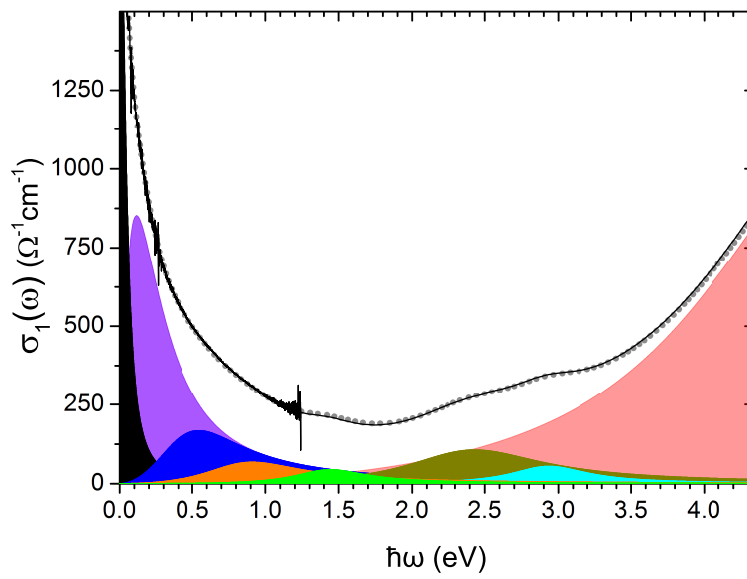


Figure 4.4: The Drude-Lorentz fit to the real part of the optical conductivity, $\sigma_1(\omega)$, at 300 K. The 4 Lorentzians above 1.2 eV are interpreted as bound charge contributions to $\sigma_1(\omega)$. The dotted grey curve is the sum of all oscillators which matches perfectly the $\sigma_1(\omega)$ calculated from Kramers-Kronig transformation (black thin curve).

4. OPTICAL PROPERTIES OF UNDER-DOPED HGBA₂CUO_{4+δ}

in the present work whether or not we assume it to be part of the conduction band response. A reasonable approximation for the total (coherent + incoherent) conduction band spectral weight is therefore

$$\omega_p^2 = \sum_{\hbar\omega_j < 1.2 \text{ eV}} \omega_{pj}^2 \quad (4.5)$$

The resulting value for $\hbar\omega_p$ is indicated in table 4.1. An alternative scheme for determining the conduction band spectral weight consists of fitting the dielectric function in the full frequency range to a sum of bound charge oscillators above 1.2 eV and to use Allen's formula (Eq. 6.1) for the conduction band conductivity of electrons coupled to bosons[42, 84, 85], where in the latter the amplitudes of the blocks of a histogram representation of the electron-boson coupling function are adjusted to obtain the best fit.

The rise in optical conductivity above 1.8 eV is due to the onset of $O : 2p \rightarrow Cu : 3d$ charge transfer transitions. The dielectric response described by the oscillators above 1.2 eV is therefore interpreted as "bound charge" response. The bound charge component of the dielectric function is

$$\begin{aligned} \epsilon_b(\omega) &= 1 + S_h + \sum_{\hbar\omega_j > 1.2 \text{ eV}} \frac{\omega_{pj}^2}{\omega_j^2 - \omega(\omega + i\gamma_j)} \\ &\cong 1 + S_h + \sum_{\hbar\omega_j > 1.2 \text{ eV}} \frac{\omega_{pj}^2}{\omega_j^2} \end{aligned} \quad (4.6)$$

The right hand side of the expression is a valid approximation for the present set of data. This is demonstrated in Fig.4.5 showing $Re\{\epsilon_b(\omega)\}$ and $Im\{\epsilon_b(\omega)\}$ using the parameters in table 4.1, together with the total dielectric function. We see, that $\epsilon_b(\omega) = 4.3 \pm 0.1$ everywhere in the frequency range shown.

4.6 Sheet conductance and spectral weight

We consider a cuprate with N_L conducting CuO₂ sheets per unit cell, having c-axis lattice parameter c . This corresponds to an average spacing $d_c = c/N_L$ between the CuO₂ sheets. The relation between sheet conductance and bulk conductivity is

$$G(\omega) = d_c \sigma(\omega) \quad (4.7)$$

4.6 Sheet conductance and spectral weight

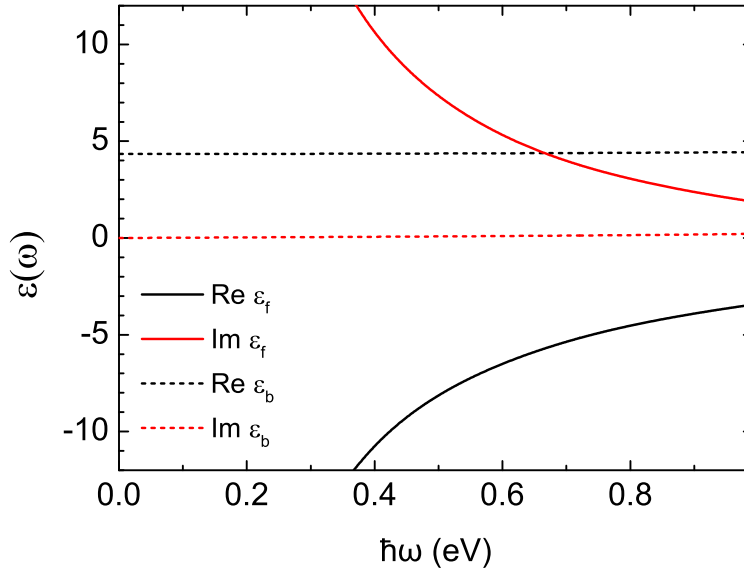


Figure 4.5: Total (solid curves) and bound charge dielectric function (last four oscillators of Table 4.1) at room temperature. To a very good approximation $\epsilon_b = 4.3 \pm 0.1$ with negligible imaginary part in the entire frequency range shown.

The general expression for spectral weight of the sheet conductance along the x_j axis is [84]

$$K = \frac{d_c}{V} \sum_{k,\sigma} n_{k,\sigma} \frac{\partial^2 \epsilon_{k,\sigma}}{\partial k_j^2} \quad (4.8)$$

where $n_{k\sigma}$ is the average occupation of the state with momentum k and spin σ . V is the sample volume. For a parabolic dispersion relation ($\epsilon_k = \hbar^2 k^2 / 2m$) the Fermi energy is πK . Ab initio LDA band-calculations for the cuprates can be accurately represented by the tight-binding expression

$$\begin{aligned} \epsilon_k = & -2t [\cos(k_x a) + \cos(k_y a)] \\ & + 4t' \cos(k_x a) \cos(k_y a) - 2t'' \cos(2k_x a) \cos(2k_y a) \end{aligned} \quad (4.9)$$

We calculated K numerically as a function of hole density, inserting Eq. 4.9 in Eq. 4.8, and adopting the parameter set appropriate to the case of Hg1201 [87]: $t = 0.45$ eV, $t'/t = 0.35$, $t''/t' = 0.5$. The parametric plot of K versus hole density is presented in Fig. 4.6 (black solid curve).

4. OPTICAL PROPERTIES OF UNDER-DOPED HGBA₂CUO_{4+δ}

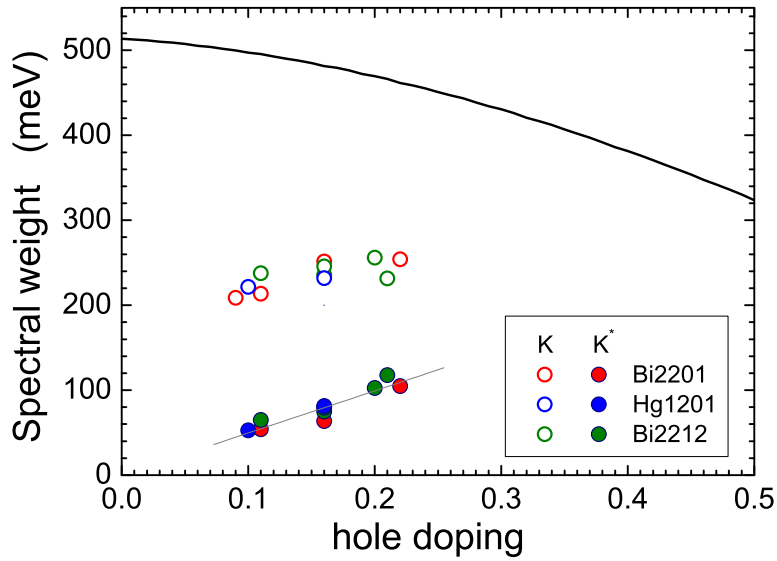


Figure 4.6: Conduction band spectral weight per CuO₂ layer for a large number of cuprate superconductors. Closed symbols: coherent spectral weight, K^* . The grey line is a linear least squares fit, $K^* = 496x$, where x is the nominal hole-doping. Open symbols: total spectral weight, K . New data are presented for Hg1201 with 10% doping (see table 4.1). For the other materials see table 1 in Ref. [86]. The black solid curve represents K calculated from ab initio band parameters for Hg1201 (Eq. 4.8). For the Bi₂Sr₂CuO₆ (Bi2201) sample with hole doping below $0.10K^*$ can not be calculated, since in this case we obtain $M_1(\omega, T) < 0$ for $\omega \rightarrow 0$, possibly due to intrinsic or stoichiometry-related inhomogeneity.

4.6 Sheet conductance and spectral weight

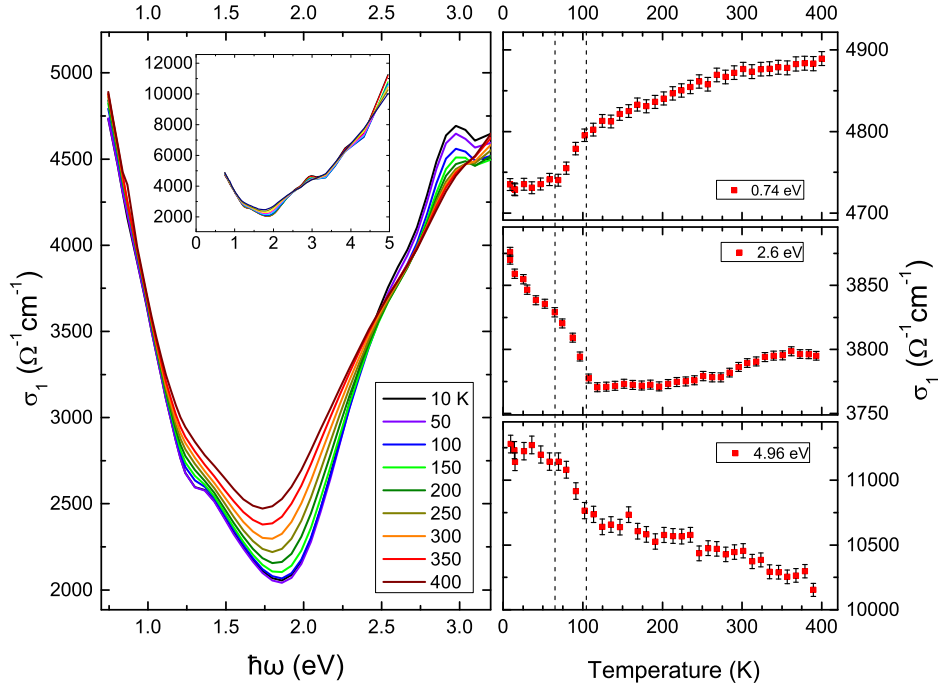


Figure 4.7: Optical conductivity of $\text{HgBa}_2\text{CuO}_{4+\delta}$ calculated from ellipsometry data (no c-axis correction). The vertical dashed lines in the right panels show the two characteristic temperatures that are discussed in the text.

4.6.1 High-energy spectral weight in superconducting state

As seen in chapter 2, ellipsometry technique allows for very precise measurement of optical values at relatively high energies (0.6-5.5 eV). Taking advantage of such high precision, it is possible to study very carefully the temperature evolution of optical parameters. The optical conductivity of $\text{HgBa}_2\text{CuO}_{4+\delta}$ sample calculated directly from the ellipsometry data is shown in figure 4.7 together with its temperature dependence at three selected energies.

One should note that in this case, no c-axis correction is applied in order to avoid errors introduced by inaccuracy of the reflectance data at high energies as well as the errors in c-axis temperature dependence (which is not measured precisely and is assumed to be negligible). Therefore, the values for the optical conductivity may not be the same as the ab-plane conductivity presented throughout this work. In this section, however, the main focus is on the spectral features, their temperature dependence and some of the possible interpretations.

The first eye-catching feature in this set of data is formation of high energy peaks

4. OPTICAL PROPERTIES OF UNDER-DOPED HGBA₂CUO_{4+δ}

at low temperatures. As shown in the left panel of figure 4.7, three peaks develop at around 1.4 eV, 2.6 eV and 3 eV at low temperatures close to the T_c . The spectral weight transfer at high energies in cuprates has been already observed using equilibrium [88, 89, 90, 91, 92, 93] and non-equilibrium techniques [94]. The peak at about 1.4 eV is in good agreement with those observations and together with the other two peaks, it may be an indication of kinetic-energy mechanism for high temperature superconductivity [95, 96, 97, 98, 99]. One can not completely rule out the possibility of changes in the interband components as the temperature changes. In fact, this together with the possible *c*-axis temperature dependent and the narrowing of the drude peak as a function of temperature, makes it difficult to analyze the intraband response in that energy range with enough precision. One solution to this problem is to use the ultrafast probe techniques (out of equilibrium) to separate the broadening of drude component from the changes in the spectral weight [94].

On the right panel of the figure 4.7, the temperature dependence of optical conductivity is shown for three different energies. Two characteristic temperatures can be observed in all the three curves: one at T_c and the other one at around 100 K. The latter might be interpreted as either the pair formation fluctuations or the inhomogeneity in the sample that causes the normal-superconductor transition to become rather broad.

4.7 Comparison with DC resistivity

Transport measurements have been performed using the 4-terminal method. Due to the irregular shape of the cleaved samples the absolute value of the DC resistivity be determined with about 20 % accuracy. However, we obtained very high relative accuracy of the temperature dependence of the DC resistivity, as seen from identical temperature dependence of samples of the same composition and doping, regardless of having significantly different dimensions and shapes. An independent check of the DC resistivity was obtained from the $\omega = 0$ limit of the experimental infrared optical conductivity (Fig. 4.8). The DC-resistivity had to be scaled by a factor 0.66 in order to match the optical data, most likely due to aforementioned influence of the irregular shape of the crystals on the absolute value of the measured DC resistances. The excellent match of the two temperature dependencies demonstrates the high quality of both DC resistivity and optical conductivity data.

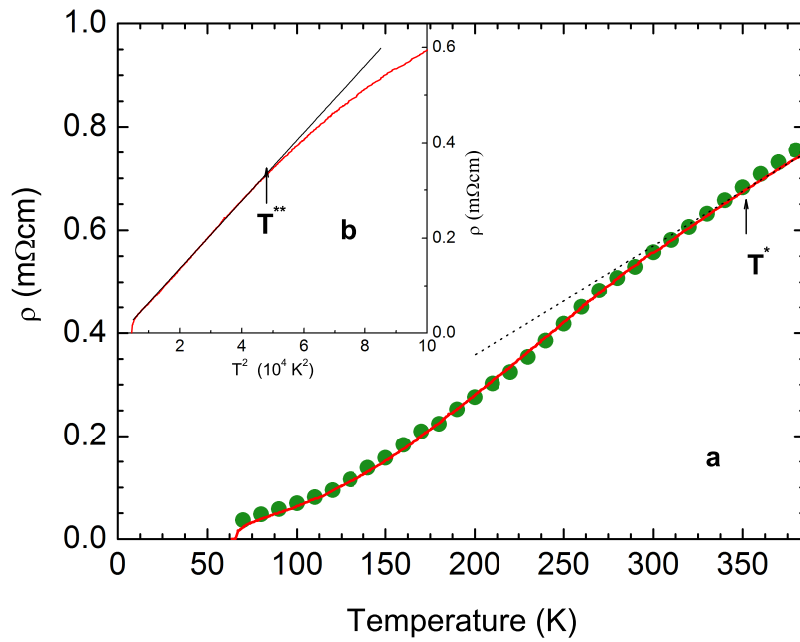


Figure 4.8: DC resistivity of underdoped Hg1201. Inverse optical conductivity extrapolated to zero-frequency (green circles) compared with measured DC-resistivity [100] (solid red line) of a sample of the same composition and doping (a). The dashed black curve is a T -linear fit to the resistivity data above 350 K. b: The same data as a function of T^2 , shown with a T^2 fit to the data below 220 K. The definitions and values for T^* and T^{**} of Ref [100] are used.

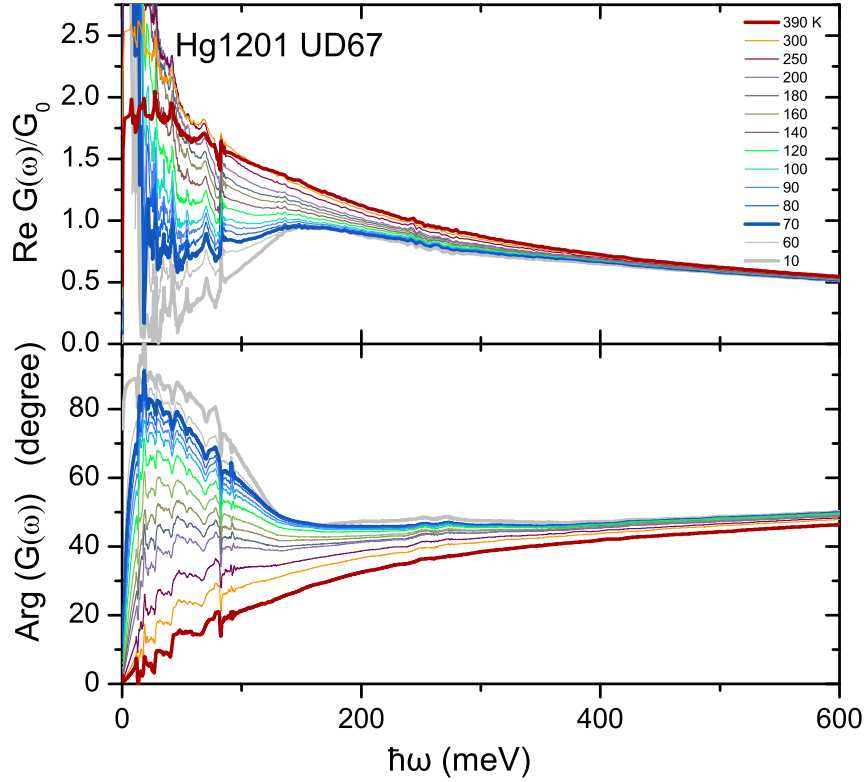


Figure 4.9: Real part (top) and Phase (bottom) of the optical sheet conductance for UD Hg1201. Temperatures from 10 to 390 K. Data below T_c are shown in grey.

4.8 Extended Drude analysis

The real part of the optical conductivity is shown in Fig 4.9 for different temperatures. There is a clear signature of a pseudogap above T_c , with a maximum at approximately 150 meV. The phase of conduction band optical conductivity, shown in Fig 4.9, has a gradual rise of phase as a function of frequency, in agreement with the behavior of underdoped Bi2212 pointed out in Ref. [64], and distinctly different from $\sigma(\omega) = C(i\omega)^{-2/3}$ observed in optimally doped cuprates. Here, the optical conductivity is expressed as a sheet conductance in units of $G_0 = 2e^2/h$ (Eq. 1.46).

The spectral weight factor K is related to the plasma frequency through Eq. 1.47. With $\hbar\omega_p = 2.053$ eV (table 4.1) and the c-axis parameter $d_c = 0.952$ nm we obtain $K = 222$ meV. The memory function $M(\omega, T)$ in Fig.4.10 is defined in section 1.4 and has been calculated from the optical conductivity using Eq.1.46. The sharp features

at 30, 40, 55, 70, 80 and 90 meV of the Hg1201 data are due to dipole active optical phonons. Although in principle these features can be subtracted from the optical conductivity before calculating $M(\omega, T)$, this kind of subtraction procedure contains some ambiguities due to Fano-like phonon asymmetries. Since after subtraction these ambiguities are imported in the resulting memory function, we have refrained from subtracting the phonons. Instead, in order to facilitate comparison of different temperatures, in some figures (like Fig.5.1) narrow bands corresponding to the prominent sharp features at 80 and 90 meV of the UD Hg1201 data have been left open.

The real and imaginary parts of the memory function of underdoped Hg1201 with $T_c = 67$ K are shown in Fig. 4.10 for temperatures from 10 to 390 K. $M_1(\omega, T)$ has a linear slope extrapolating to $\omega = 0$, which becomes less steep at higher temperatures. The maximum at 105 meV erodes gradually as temperature increases, but a residue of this structure remains visible even at 390 K. In the lower left inset we show a plot of the frequency and temperature dependent mass enhancement factor, $m^*(\omega, T) = M_1(\omega, T)/\hbar\omega + 1$. For ω above 60 meV $m^*(\omega, T)$ is a monotonously decreasing function of temperature. For ω not too large, $m^*(T)$ is roughly speaking a plateau at low temperatures, terminating in a weak maximum at $T(max)$ and followed by a linear-like decrease at higher temperature. $T(max)$ increases when ω decreases and for $\omega \rightarrow 0$ extrapolates to 212 K $\sim T^{**}$, indicating another way of identifying T^{**} . The increase of $m^*(\omega, T)$ from about 3 at 390 K to 5 at T^{**} , taken together with the strong temperature dependence of $M_1(\omega, T)$ near its maximum at 105 meV, indicate that the charge carriers become increasingly renormalized when the temperature decreases. Our results also corroborate the observation in Ref. [101], that the integrated optical conductivity does not decrease when T decreases, so that no opening of an optical pseudogap is seen when, at T^* , part of the Fermi-surface is removed by a pseudo-gap, despite the emergence at this temperature of a novel ordered state with two Ising-like magnetic collective modes at 54 and 39 meV as observed with inelastic neutron scattering [102].

Turning now to the dynamical relaxation rate $1/\tau(\omega, T)$, we observe that its frequency dependence exhibits an upward curvature for all temperatures. Also the temperature dependence has a T^2 component for the lowest frequencies. For frequencies higher than 50 meV this component is either absent or completely masked by the onset of superconductivity (grey segments of the temperature traces). Although $M_2(\omega, T)$ has no maximum as a function of temperature, the curves have an inflection point

4. OPTICAL PROPERTIES OF UNDER-DOPED HGBA₂CUO_{4+δ}

which shifts from roughly 200 K to 100 K when the frequency is raised from 10 to 50 meV. The saturation of $m^*(\omega, T)$ and the merging of the resistivity with a T^2 dependence indicate that the system enters a Fermi liquid like state at approximately 200 K.

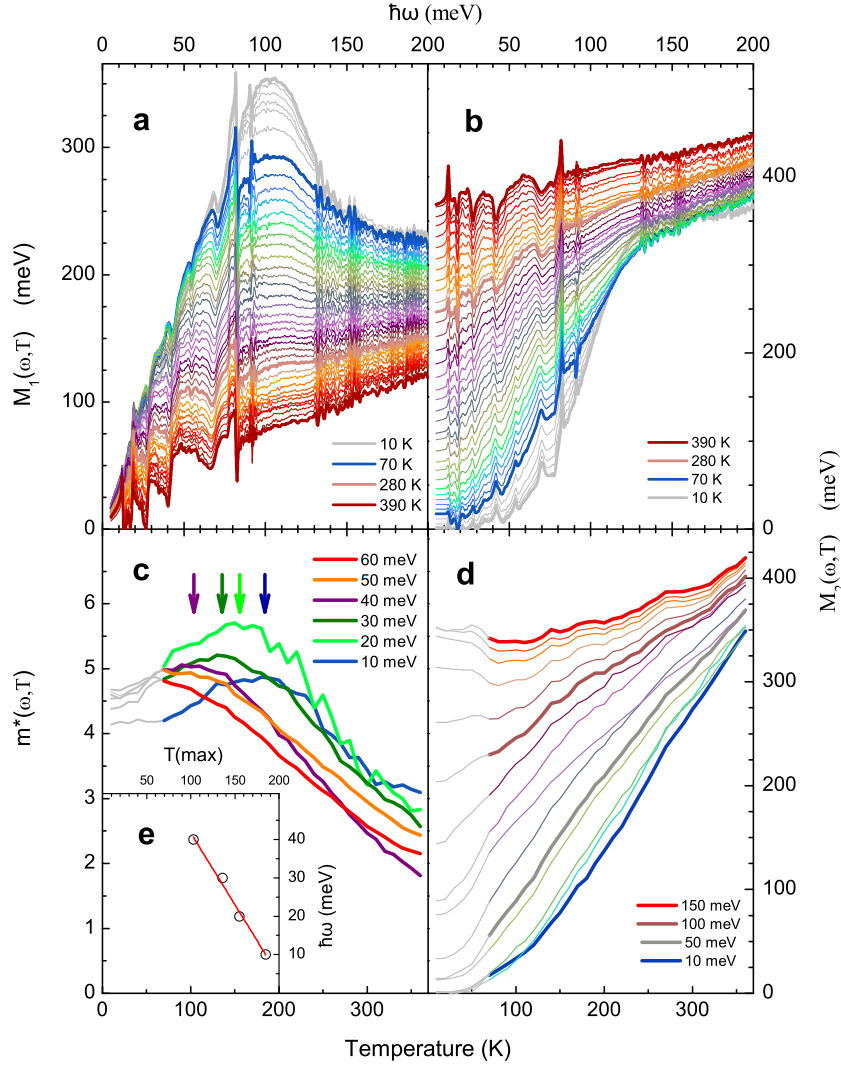


Figure 4.10: Optical self energy as a function of frequency and temperature. Real (a) and imaginary part (b) of the memory function as a function of $\hbar\omega$ for underdoped Hg1201 ($T_c = 67$ K). Spectra are shown in 10 K intervals for temperatures from 10 to 390 K. Thick lines are used to highlight the 10 K, 70 K, 280 K and 390 K data. Panel c (d) Effective mass $m^*(\omega, T)$ (relaxation rate $M_2(\omega, T)$) as a function of temperature for selected values of $\hbar\omega$. The temperatures of the maxima, $T(\max)$, are indicated with an arrow for ω with the corresponding color. Panel e shows the same $T(\max)$ versus ω . The solid curve is a linear fit extrapolating to $T(\max) = 212$ K for $\omega \rightarrow 0$. Spectra are shown in 10 meV intervals from 10 to 60 meV (150 meV) in panel c (d). Thick lines are used to highlight the data at selected energies. Data in the superconducting state is in grey. The temperature range (370 K) of the lower panels is chosen such as to match the frequency range of the upper panels (200 meV) according to the scaling relation $2\pi k_B T = \hbar\omega$.

4. OPTICAL PROPERTIES OF UNDER-DOPED HGBA₂CUO_{4+δ}

Fermi-liquid behavior in under-doped cuprates

5.1 Introduction

One of the open questions in high- T_c field is the existence of non fermi-liquid behavior in the optimally-doped and (arguably) in the under-doped part of the phase diagram of cuprates. In particular, appearance of a “pseudogap” in density of states around the Fermi-level in under-doped regime is a longstanding puzzle in this field [103].

The BCS theory [104] is based on formation of cooper pairs in the Fermi-liquid state of metals and one would naturally expect that the normal state of cuprates might have some sort of Fermi-liquid origin. Signatures for Fermi-liquid behavior are typically observed in experiment as T^2 behavior of DC resistivity, existence of closed loops in fermi surface in ARPES (Angle Resolved Photo-Emission Spectroscopy), observation of quantum oscillations and linear specific heat. The over-doped cuprates show these signatures [105, 106, 107] and are believed to obey Fermi-liquid physics. However, it is now well established that the normal state of the optimally-doped cuprates shows non-fermi liquid behavior which is usually associated to quantum criticality in this regime [62, 108, 109, 110]. For the under-doped regime, the quantum criticality argument does not hold and despite the natural expectation for existence of a Fermi-liquid, it has been believed for long that the Fermi-liquid physics do not apply to this regime. This was in particular due to observation of the pseudo-gap in tunneling density of states [111] as well as “Fermi-arcs” in ARPES [112]. The narrow temperature range between pseudo-gap temperature and the superconducting temperature together

5. FERMI-LIQUID BEHAVIOR IN UNDER-DOPED CUPRATES

with lack of low-impurity single crystals has prevented us from observing the Fermi-liquid behavior very clearly in optical scattering rate [113] and DC-resistivity [114] of under-doped samples.

Recent advances in crystal growth quality as well as measurement techniques, have enabled scientists to re-consider the possibility of existence of Fermi-liquid in under-doped cuprates [100, 115]. In this chapter, we show strong evidence for Fermi-liquid behavior in $\text{HgBa}_2\text{CuO}_{4+\delta}$ [116].

5.2 Optical signatures of Fermi-liquid behavior in $\text{HgBa}_2\text{CuO}_{4+\delta}$

In chapter 4, the memory function $M(\omega, T)$ was obtained using the extended-Drude formalism. Plotting $M_2(\omega, T)$ as a function of ω^2 (Fig. 5.1) we notice that for all temperatures above T_c , the initial rise is given by a linear slope as a function of ω^2 (inset of Fig. 5.1). For an ideal Fermi liquid $M(\omega, T)$ in the relevant range of ω and T is, to a good approximation

$$M(\omega, T) \cong \left(\frac{1}{Z} - 1 \right) \hbar\omega + iC [(\hbar\omega)^2 + (p\pi k_B T)^2] \quad (5.1)$$

where Z is the quasi-particle residue, C is a constant with units of inverse energy, and $p = 2$. To check possible Fermi liquid characteristics of the data, we introduce a single parameter ξ defined as $\xi^2 = (\hbar\omega)^2 + (p\pi k_B T)^2$, and we investigate M_2 as a function of ξ . As shown in Fig. 5.2 for three underdoped cuprate materials (Hg1201, ortho-II $\text{YBa}_2\text{Cu}_3\text{O}_{6.5}$ (Y123) [117], and Bi2201 [86]) with hole concentration $x \approx 0.1$, the M_2 data of the normal state collapse in the low energy range on a single scaling curve for $p = 1.5$. This value of p was obtained by searching for the best scaling collapse for $1 \leq p \leq 2$ in steps of 0.1. Comparing the functional form of $M_2(\xi)$ for these three materials, we make the following observations: (i) Going from Hg1201 (left) to Bi2201 (right) in this plot, the residual ($\xi = 0$) value of $M_2(\xi)$ increases from 0 to about 80 meV. Indeed, it is believed that the relatively low values of T_c in single layer Bi2201 have to do with strong scattering by disorder [118]. (ii) We also notice that in the case of Bi2201 some negative curvature shows up at the lowest energies, which is an indication that the Fermi liquid-characteristics are affected to some extent, and appear to be relatively fragile with respect to disorder. (iii) The implications of the loss

5.2 Optical signatures of Fermi-liquid behavior in $\text{HgBa}_2\text{CuO}_{4+\delta}$

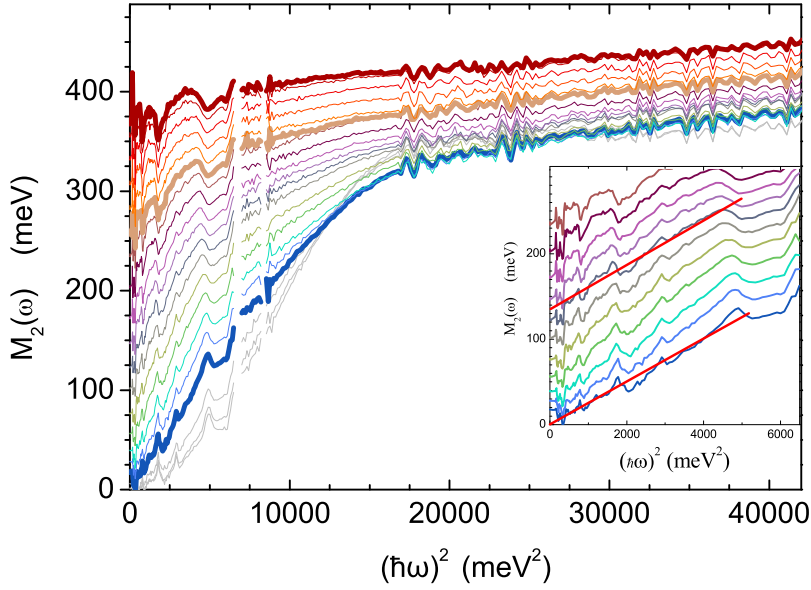


Figure 5.1: Dynamical relaxation rate of underdoped Hg1201. Imaginary part of the memory function of UD Hg1021 ($T_c = 67$ K) for temperatures between 10 and 390 K in 20 K steps as a function of ω^2 . Thick lines are used to highlight the 70 K, 280 K and 390 K data. Inset: Zoom of the low- ω range showing a linear fit, temperatures are from 70 to 270 K in 20 K steps.

of overlap above 100 meV in the Bi2201 data are not entirely clear. In principle there is no reason to expect overlap, since this is clearly beyond the range of "universal" Fermi liquid behavior. However, the single parameter scaling seems still to persist into this regime for the other two materials (Y123 and Hg1201), leading to the speculation that impurity scattering contributes to the disappearance of overlap above 100 meV for the Bi2201 sample.

The most important observation borne out by these data is, that the frequency dependence of $M_1(\omega, T)$ and $M_2(\omega, T)$ follows by and large the behavior expected for a Fermi liquid: At low frequencies and temperatures $M_1(\omega, T)$ is indeed a linear function of ω , and $M_2(\omega, T)$ scales with $(\hbar\omega)^2 + (p\pi k_B T)^2$. We note that recent theories (e.g. Refs. [119, 120, 121]) have emphasized the possible relevance of Fermi liquid concepts -or a hidden form of these in the superconducting regime [122]- to the metallic state of hole-doped cuprates. Our experimental observations provides a strong incentive for further theoretical work in this direction. We highlight two striking aspects of the data: (i) The slope $\partial M_1(\omega, T)/\partial\omega$ for $\omega \rightarrow 0$ decreases significantly as a func-

5. FERMI-LIQUID BEHAVIOR IN UNDER-DOPED CUPRATES

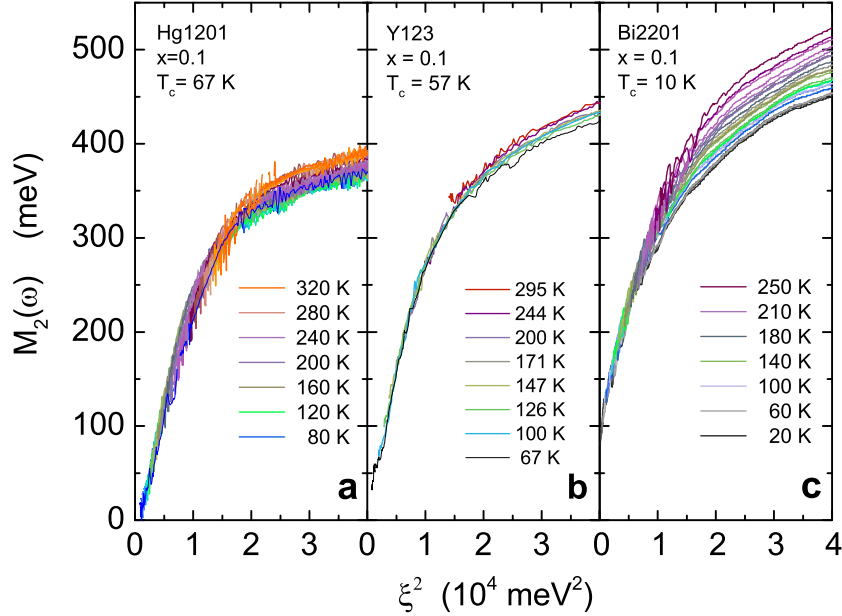


Figure 5.2: Collapse of the frequency and temperature dependence of the relaxation rate of underdoped cuprate materials. Normal state $M_2(\omega, T)$ as a function of $\xi^2 \equiv (\hbar\omega)^2 + (p\pi k_B T)^2$ with $p = 1.5$. a: Hg1201 ($x \cong 0.1, T_c = 67$ K). b: Y123 ($x \cong 0.1, T_c = 57$ K), spectra by Hwang *et al.* [117] (digitized data of Fig. 6) represented here as a function of ξ^2 , c: Bi2201 ($x \cong 0.1, T_c = 10$ K); data of van Heumen *et al.* [86] represented here as a function of ξ^2 . The data displayed in panels a and c are in 10 K intervals with color coding indicated for temperatures in 40 K steps. In between these steps the color evolves gradually as a function of temperature. In panel b the color coding is given for all temperatures displayed.

tion of increasing temperature, (ii) $p < 2$. We speculate that these issues are related to the progressive filling-in of the pseudo gap as a function of increasing temperature. Already in a two-fluid picture of a nodal Fermi liquid in parallel to an anti-nodal liquid non-universal features (for Fermi liquids) are introduced in the optical conductivity, since the properties at the Fermi surface change gradually from Fermi liquid at the nodes [123] to strongly incoherent and pseudo-gapped at the hot spots near the anti-nodes [124]. In fact, $p = 2$ has not been reported until now in any other material [125, 126, 127]. Recently Maslov and Chubukov interpreted this as a combination of Fermi liquid scattering and an additional source of elastic scattering from magnetic moments or resonant levels [128].

Theoretically it is expected that the T^2 and ω^2 dependence of $M_2(\omega, T)$ is limited to $\hbar\omega$ and $p\pi k_B T$ lower than some energy scale ξ_0 , which in the context of single

5.2 Optical signatures of Fermi-liquid behavior in $\text{HgBa}_2\text{CuO}_{4+\delta}$

parameter scaling behavior of a Fermi liquid is proportional to the effective Fermi energy. Strong electronic correlations strongly reduce this energy scale, as compared to the bare Fermi energy. For most materials the issue of the Fermi liquid like frequency dependence of $M_2(\omega, T)$ has remained largely unexplored. This is related to the difficulty that, in cases such as the heavy fermion materials where this type of coupling dominates, the range of Fermi liquid behavior is smaller than 10 meV, making it particularly difficult to obtain the required measurement accuracy in an infrared experiment. Clean underdoped cuprates present in this respect a favorable exception, since as can be seen from Figs. 5.1 and 5.2, the relevant energy scale ξ_0 is about 100 meV for a doping level around 10%. Above this energy $M_2(\omega, T)$ crosses over to a more linear trend both as a function of ω and T . This suggests that in cuprates the range of applicability of Fermi liquid behavior is limited by a different scattering mechanism that develops at high- T and high- ω , as the pseudogap gets filled.

The ξ^2 dependence of the relaxation rate can be understood as follows [68]: An electron at a distance ξ above the Fermi energy can, as a result of electron-electron interactions, decay to a final state $\xi - \Omega$ by creating an electron-hole pair of energy. The density of states of electron-hole pairs is the spin (charge) susceptibility $\chi''(\Omega)$ where spin (charge) refers to electron-hole pairs carrying (no) net spin. $\chi''(\Omega)$ can be strongly renormalized, but the property that $\chi''(\Omega) \propto \Omega$ in the limit $\Omega \rightarrow 0$ is generic for Fermi liquids [129]. Integration of the susceptibility multiplied with the interaction vertex, $I^2\chi''(\Omega)$, over all possible decay channels from zero to ξ leads us to conclude that indeed $M_2 \propto \xi^2$ reported experimentally in the present manuscript. In this description the cross-over ξ_0 corresponds to the energy where $I^2\chi''(\Omega)$ is truncated, leading to a leveling off of M_2 for $\xi > \xi_0$. The strong temperature dependence of $M_1(\omega, T)$ is also a natural consequence of this description; it was shown in Ref. [130] that, in leading orders of temperature, $\chi''(\Omega)$ of a correlated Fermi liquid decreases as a function of temperature. In chapter 6, a model for charge susceptibility of a Fermi liquid will be investigated using electron-boson coupling theory. In that model, the susceptibility is assumed to be linear in frequency as argued above.

5. FERMI-LIQUID BEHAVIOR IN UNDER-DOPED CUPRATES

Optical Data Analysis Using Strong Coupling Formalism

6.1 Introduction

Allen suggested in 1971 that optical data of normal and superconducting states in metals contain important information about the electron-phonon coupling mechanism [85]. If anisotropy in k-space is ignored, the optical conductivity using Kubo's formula (derived from current-current correlation) can be written as:

$$\begin{aligned}\sigma(\omega) &= \frac{\omega_p^2}{4\pi\omega} \frac{i}{\omega + M(\omega)} \\ &= \frac{i\omega_p^2}{4\pi\omega} \int_{-\infty}^{\infty} \frac{n_F(\xi) - n_F(\xi + \omega)}{\omega - \Sigma(\xi + \omega) + \Sigma^*(\xi) + i\Gamma_{imp}} d\xi\end{aligned}\quad (6.1)$$

where ω_p^2 is the plasma frequency, $M(\omega)$ is the memory function (Eq. 1.42), n_F is the Fermi-Dirac distribution function, $\Sigma(\omega)$ is the single particle self energy and Γ is the impurity scattering.

By using this formalism, all optical properties can be calculated if a good way for the estimation of the single particle self energy can be found. Of course, the full evaluation of the self energy requires an infinite number of processes to be taken into account. Here, we make several approximations in order to simplify the self energy calculation:

1. Migdal's approximation: According to Migdal [131] all vertex corrections can

6. OPTICAL DATA ANALYSIS USING STRONG COUPLING FORMALISM

be ignored in the calculation of the self-energy, which makes it much simpler to evaluate.

2. The momentum dependence of the self energy is ignored.
3. The density of states is assumed to have no energy dependence.

Using the simplifications above, and by assuming that the Fermi liquid picture holds, we can write the self energy as:

$$\Sigma(\omega) = \int_0^{\infty} \Pi(\omega') L(\omega, \omega') d\omega' \quad (6.2)$$

where

$$L(\omega, \omega') = \int_{-\infty}^{\infty} \left\{ \frac{n_B(\omega') + n_F(\varepsilon)}{\omega - \varepsilon + \omega' + i0^+} + \frac{n_B(\omega') + 1 - n_F(\varepsilon)}{\omega - \varepsilon - \omega' + i0^+} \right\} d\varepsilon \quad (6.3)$$

is a kernel that captures the temperature dependence according to the assumption above and $\Pi(\omega)$ corresponds to the density of states of bosonic modes multiplied with the square of the coupling constant. $\Pi(\omega)$ can in principle be composed of phonons, spin and charge fluctuations.

The optical memory function can be calculated from the following equation:

$$M(\omega) = \omega \left\{ \int_{-\infty}^{\infty} \frac{n_F(\xi) - n_F(\xi + \omega)}{\omega - \Sigma(\xi + \omega) + \Sigma^*(\xi) + i\Gamma_{imp}} d\xi \right\}^{-1} - \omega \quad (6.4)$$

Finally, we define the mass renormalization factor as:

$$\lambda = 2 \int_0^{\infty} \frac{\Pi(\omega)}{\omega} d\omega \quad (6.5)$$

This parameter is related to the mass enhancement through:

$$\frac{m^*}{m} = 1 + \lambda \quad (6.6)$$

6.2 Improvement in numerical calculations

Using Allen's formalism, the numerical evaluation of the memory function and $\sigma(\omega)$ requires three integrals to be evaluated:

1. The integral for the kernel $L(\omega, \omega')$ (Eq.6.3).
2. The integral for evaluation of the single particle self energy $\Sigma(\omega)$ (Eq.6.2).
3. The integral that evaluates the optical conductivity $\sigma(\omega)$ from the self energy $\Sigma(\omega)$ (Eq.6.1).

The first integral can be analytically simplified as follows:

$$\begin{aligned} L(\omega, \omega') &= \int_{-\infty}^{\infty} \left\{ \frac{n_B(\omega') + n_F(\varepsilon)}{\omega - \varepsilon + \omega' + i0^+} + \frac{n_B(\omega') + 1 - n_F(\varepsilon)}{\omega - \varepsilon - \omega' + i0^+} \right\} d\varepsilon \\ &= -i\pi \coth\left(\frac{\omega'}{2T}\right) + \Psi\left(\frac{1}{2} + i\frac{\omega' - \omega}{2\pi T}\right) - \Psi\left(\frac{1}{2} - i\frac{\omega' + \omega}{2\pi T}\right) \end{aligned} \quad (6.7)$$

Where $\Psi(x)$ is the ‘‘digamma’’ function or the logarithmic derivative of the gamma function:

$$\Psi(x) = \frac{d}{dx} \ln \Gamma(x) \quad (6.8)$$

This simplification has been used in the calculation algorithms of other works.[42][4] In this thesis, we will introduce a new simplification method that (together with the previous method) greatly improves the evaluation speed of self energy integral (Eq.6.2). For this purpose, we define the bosonic spectra $\Pi(\omega)$ to be composed of histograms (blocks) with fixed frequency coordinates and variable amplitude(see Fig.6.1):

$$\Pi(\omega) = \sum_{i=1}^n a_i (\theta(\omega_i) - \theta(\omega_{i+1})) \quad (6.9)$$

Where $\theta(\omega)$ is the heaviside step function, $n - 1$ is the number of blocks and $\omega_i > 0$. This way, we can split the self energy integral into many pieces each with $\Pi(\omega)$ being a frequency-independent constant and therefore leaving the integral. This, together with

6. OPTICAL DATA ANALYSIS USING STRONG COUPLING FORMALISM

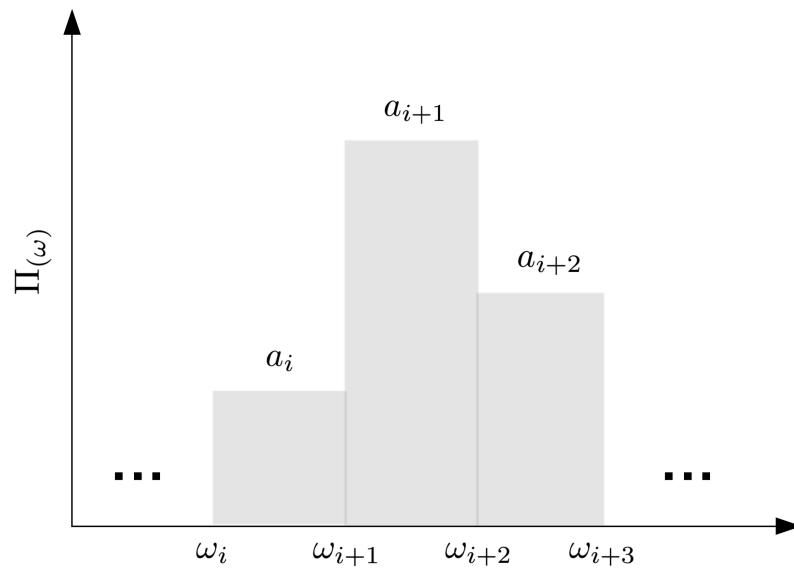


Figure 6.1: Histogram representation of the bosonic spectra $\Pi(\omega)$. In our model, the first frequency ω_1 is always greater than zero. Keeping the frequencies fixed during fitting will help the fitting algorithm converge faster.

6.2 Improvement in numerical calculations

the first simplification (Eq.6.7) gives:

$$\begin{aligned}
 \Sigma(\omega) &= \sum_{i=1}^n a_i \int_{\omega'_i}^{\omega'_{i+1}} L(\omega, \omega') d\omega' \\
 &= \sum_{i=1}^n a_i \left(\int_{\omega'_i}^{\omega'_{i+1}} -i\pi \coth\left(\frac{\omega'}{2T}\right) d\omega' \right. \\
 &\quad \left. + \int_{\omega'_i}^{\omega'_{i+1}} \Psi\left(\frac{1}{2} + i\frac{\omega' - \omega}{2\pi T}\right) d\omega' \right. \\
 &\quad \left. - \int_{\omega'_i}^{\omega'_{i+1}} \Psi\left(\frac{1}{2} - i\frac{\omega' + \omega}{2\pi T}\right) d\omega' \right)
 \end{aligned} \tag{6.10}$$

We can analytically solve the integrals by having:

$$\int \Psi(x) dx = \int \frac{d}{dx} \ln \Gamma(x) dx = \ln \Gamma(x) \tag{6.11}$$

$$\int \coth\left(\frac{\omega'}{2T}\right) d\omega' = 2T \ln\left(\sinh\left(\frac{\omega'}{2T}\right)\right) \tag{6.12}$$

That gives the final result as a sum over a set of functions that can be evaluated numerically very fast:

$$\begin{aligned}
 \Sigma(\omega) &= \sum_{i=1}^n a_i \left(-i2\pi T \ln\left(\sinh\left(\frac{\omega'}{2T}\right)\right) \Big|_{\omega'_i}^{\omega'_{i+1}} \right. \\
 &\quad \left. + \ln \Gamma\left(\frac{1}{2} + i\frac{\omega' - \omega}{2\pi T}\right) \Big|_{\omega'_i}^{\omega'_{i+1}} \right. \\
 &\quad \left. + \ln \Gamma\left(\frac{1}{2} - i\frac{\omega' + \omega}{2\pi T}\right) \Big|_{\omega'_i}^{\omega'_{i+1}} \right)
 \end{aligned} \tag{6.13}$$

In a simpler form, the equation 6.13 can be written as:

$$\Sigma(\omega) = \sum_{i=1}^n a_i X_i(T, \omega) \tag{6.14}$$

6. OPTICAL DATA ANALYSIS USING STRONG COUPLING FORMALISM

Where for a constant temperature T , $X(T, \omega)$ becomes a matrix that can be calculated once and be used for evaluation of the self energy for different values of amplitude vector a . This method reduces an integral over the the whole frequency range to a sum over the number of blocks which is much faster to be numerically evaluated. The algorithm made out of this method has been used for all the calculations in this thesis which has gained an order of magnitude higher speed in the particular case of fitting. Another advantage of this method is that there is less probability for occurrence of local minimum problem during the least squares fitting due to fixed frequency positions.

6.3 Analysis of under-doped $\text{HgBa}_2\text{CuO}_{4+\delta}$

In this section, the optical spectra of under-doped $\text{HgBa}_2\text{CuO}_{4+\delta}$ sample (presented in chapter 4 in detail) is analyzed using the improved method explained in the previous section. To have a better intuition, the memory function $M(\omega)$ will be presented throughout this section instead of optical conductivity $\sigma(\omega)$: The real and imaginary part of the memory function are directly connected to the frequency dependent enhanced mass m^* and the scattering rate respectively.

All the optical conductivity data have been transformed into memory function using the equation 1.42 which needs the plasma frequency ω_p to be set for each temperature. The Eliashberg-Migdal theory does not count for the interband transitions in the optical response. Therefore, the interband contribution to the optical conductivity has to be either subtracted from the optical data or included in the model. In our data, the optical conductivity (directly from Kramers-Kronig transformation of the reflectivity) was transformed into interband-free conductivity by subtracting a constant interband term at high frequencies and then transformed into memory function $M(\omega)$ assuming a constant plasma frequency for all temperatures. Our model memory function is capable of correcting for the interband contribution and the plasma frequency in case of need.

The real and imaginary parts of the memory function ($M_1(\omega)$ & $M_2(\omega)$) have been simultaneously fitted to a model with 40 histograms which represent the bosonic spectra ($\Pi(\omega)$) of the equation 6.2. The DC-resistivity has been added to the scattering rate at its lowest frequency ($M_2(\omega \rightarrow 0)$) as a single data point with low error which keeps the temperature behavior of the resulting fit consistent with DC-resistivity measurement. Figure 6.2 shows the resulting bosonic spectra for a few selected temperatures.

6.4 Fermi-liquid susceptibility: A minimal model

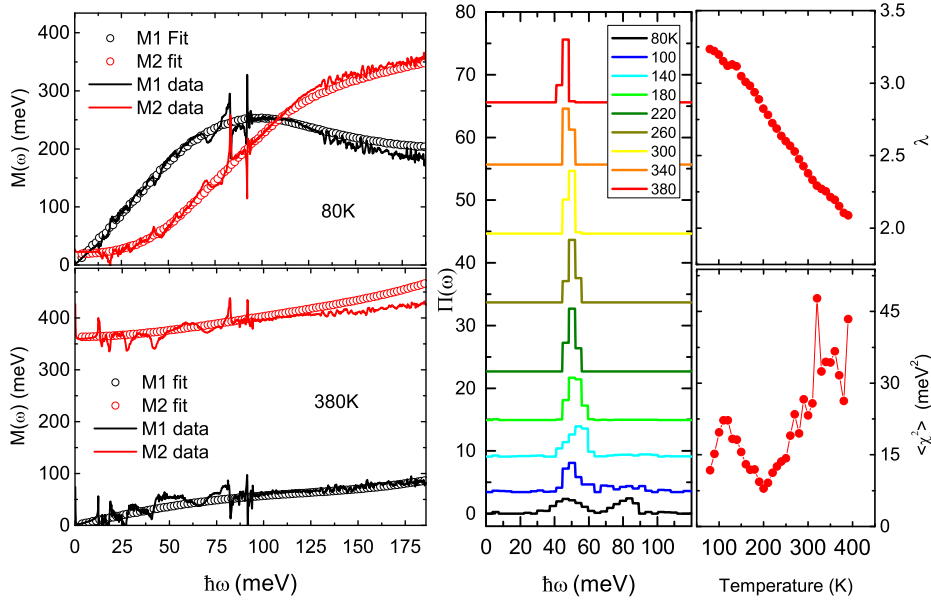


Figure 6.2: Results for fitting memory function of $\text{HgBa}_2\text{CuO}_{4+\delta}$ to the histogram model. The fitted memory functions are compared to data for two temperatures in the left column. The resulting bosonic spectra are shown in the middle column for different temperatures. The top-right panel shows the values for the coupling constant λ (see Eq. 6.5). The averaged (weighted) sums of squares of errors are shown in the bottom-right panel.

From the figure it is evident that at low temperatures and close to the superconducting transition, the spectra has two distinct features one at around 50 meV and the other at around 80 meV. The intensity of the latter decreases rapidly as the temperature increases which is probably related to the superconducting fluctuations. In the right panel, the coupling constant λ (see Eq.6.5) is shown as a function of temperature at the top, and the averaged sum of squared errors χ^2 is shown at the bottom. An important feature of this spectra is the presence of a peak at around 50 meV as observed in other cuprates [132][?][42].

6.4 Fermi-liquid susceptibility: A minimal model

The Fermi-liquid theory predicts that the imaginary part of the susceptibility $\chi''(\omega)$ is proportional to the energy at low energies: $\chi''(\omega) \propto \omega$ [68]. Since a Fermi-liquid like behavior has been observed in the $\text{HgBa}_2\text{CuO}_{4+\delta}$ sample (see chapter 5), a simple

6. OPTICAL DATA ANALYSIS USING STRONG COUPLING FORMALISM

model with susceptibility proportional to energy is expected to be able to explain the observed optical properties in this sample. For this purpose, the memory function and the DC-resistivity have been calculated using a simple model with the following bosonic spectral function $\Pi(\omega)$:

$$\Pi(\omega) = \begin{cases} \alpha\omega & \omega < \omega_c \\ 0 & \omega \geq \omega_c \end{cases} \quad (6.15)$$

Where α is a coefficient and ω_c is the cut-off frequency of the spectra. The results are shown in figure 6.3. As seen in the left panel of the figure, the DC resistivity has a T^2 behavior up to about 250 K and becomes linear for higher temperatures. However, when looking at the experimental resistivity data, the deviation from T^2 can not be explained with the bosonic spectra of equation 6.15 and a change in the shape of $\Pi(\omega)$ is inevitable. In this chapter, an effort is made to find a minimal model that fits the optical memory functions. The very first model to investigate would be the same model as mentioned above but with α and ω_c varying at different temperatures:

$$\Pi(\omega, T) = \begin{cases} \alpha(T)\omega & \omega < \omega_c(T) \\ 0 & \omega \geq \omega_c(T) \end{cases} \quad (6.16)$$

The model parameters $\alpha(T)$ and $\omega_c(T)$ were determined using the least-squared fitting method explained before. The results are shown in figure 6.4. It is clear from the shape of the produced memory functions that this model does not fit all the spectral features of the optical data while the DC resistivity of the model fits well the measured resistivity. The model gives much more accurate results for higher temperatures as seen in the inset of the DC-resistivity (bottom-left panel). It was already visible from the histogram model that there is a peak at around 50 meV in the bosonic spectra as well as some feature at higher energies. To mimic these two features while respecting the Fermi-liquid model of ramped spectra, another model is introduced which consists of a ramped shape spectra and two 12 meV-wide peaks one at 50 meV and the other at

6.4 Fermi-liquid susceptibility: A minimal model

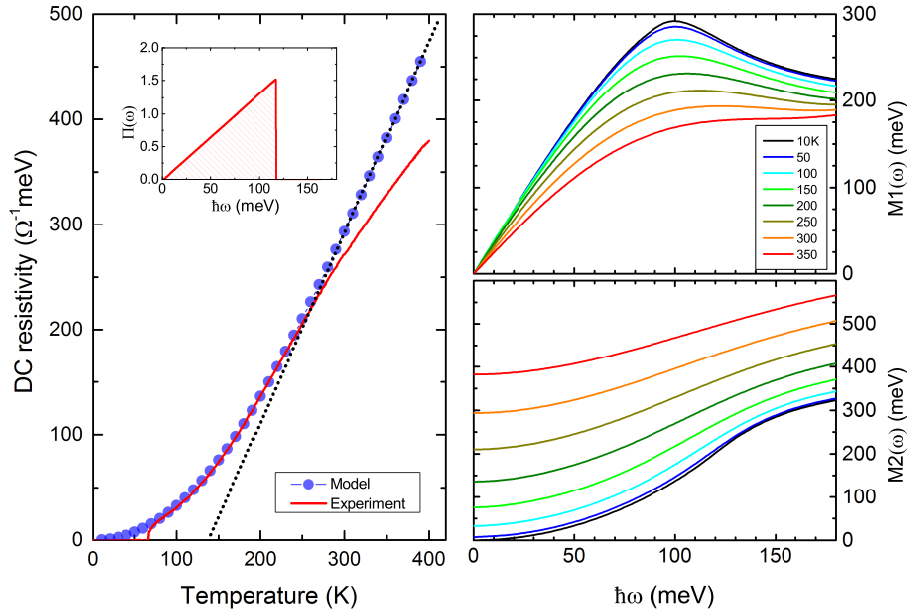


Figure 6.3: The resulting memory function and dc resistivity of a ramp-shaped bosonic spectra. The DC-resistivity curve matches well the experimental resistivity of $\text{HgBa}_2\text{CuO}_{4+\delta}$ sample up to about 250 K. This is in a very good agreement with assumptions about having a standard Fermi-liquid in the pseudo-gap regime of cuprates. However, the optical spectra of $\text{HgBa}_2\text{CuO}_{4+\delta}$ can not be reproduced using such simple ramp-shaped spectra and more complicated model are needed to explain both DC-resistivity and the optical features.

6. OPTICAL DATA ANALYSIS USING STRONG COUPLING FORMALISM

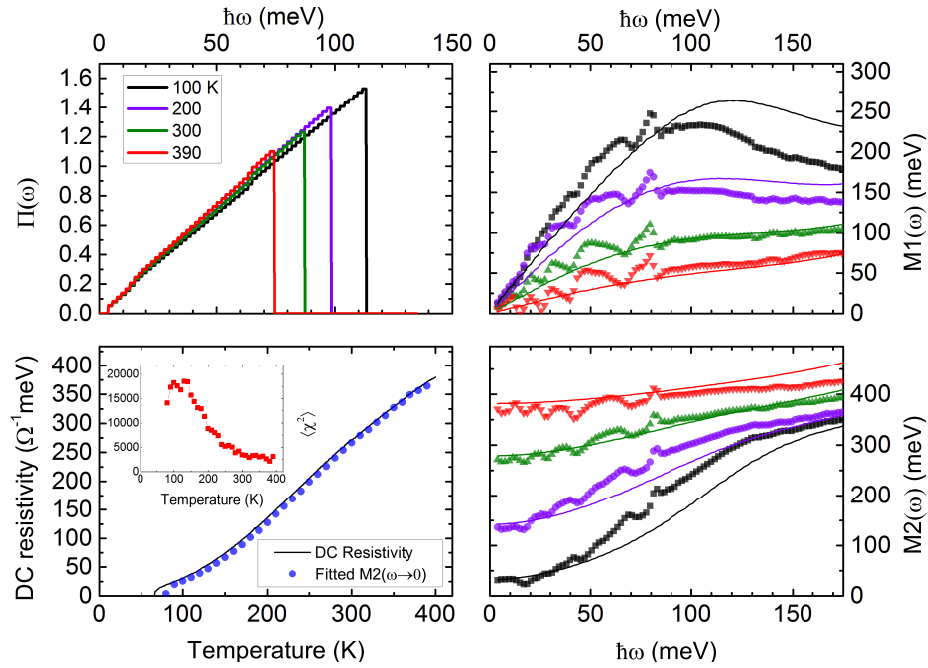


Figure 6.4: Fitting results for the simple triangle model (Eq.6.16). Despite the variation in cut-off frequency ω_c and good match of DC resistivity curves (bottom left panel), the optical data is not yet reproduced well using this model. In particular the shift to the higher frequencies of the maximum in $\Pi(\omega)$ as a function of decreasing temperature leads to the discrepancies around 100 meV for the lower temperature data.

6.4 Fermi-liquid susceptibility: A minimal model

80 meV with variable amplitudes:

$$\Pi(\omega, T) = \begin{cases} \alpha(T)\omega & \omega < \omega_c(T) \\ \Pi_1(T) & \omega_{p1} - 12 < \omega < \omega_{p1} + 12 \\ \Pi_2(T) & \omega_{p2} - 12 < \omega < \omega_{p2} + 12 \\ 0 & \text{elsewhere} \end{cases} \quad (6.17)$$

Where Π_1 and Π_2 are the amplitudes of the peaks and ω_{p1} and ω_{p2} are the central frequency of the two peaks. Since in a simple Fermi-liquid model the density of states (and hence the susceptibility) is assumed to remain constant for different temperatures, one may naturally expect the slope α in the model to stay constant. However, the effect of opening of a pseudo-gap has also to be considered. Even though gapping of the Fermi surface happens at the anti-nodes in k-space, its possible effect on $\sigma(\omega)$ can not be ruled out. This means that our optical conductivity is sensitive to the opening of the pseudo-gap in particular for frequencies above 100 meV. We ignore these complications for the moment, and try to fit the entire $M(\omega, T)$ spectrum with a single component model given by $\Pi(\omega, T)$. We will return to the implications and pitfalls in the discussion part at the end of this chapter.

Two models are studied: Model I with fixed slope α and variable cut-off frequency ω_c and model II with variable slope and fixed cut-off frequency. The first model is inspired by the assumption that the density of states (and hence the susceptibility) should remain constant for all the temperature while the second case considers the fact that the optical spectra might be affected by other phenomena such as spin(charge) density waves, low-energy interband transitions and Fermi surface anisotropy. It should be noted that letting all the variables free during the fitting can easily lead to the well-known ‘‘local minima’’ problem which stops the fit to converge easily or may prevent us from getting meaningful parameters. The results for the two different models are presented in figures 6.5 and 6.6.

In the first model (fixed α and varying ω_c), a gradual decrease in the ω_c is observed upon increasing the temperature up to about 200 K which is close to the Fermi-liquid temperature T^{**} . For $T > T^{**}$ we find the ω_c and averaged error both fluctuating within a wide range (see insets of the top left and bottom left panels in Fig.6.5) which indicates that the model can not decide about the value of ω_c or -in other words- it does not need the ramp-shaped spectra to fit the optical data in the non-Fermi liquid

6. OPTICAL DATA ANALYSIS USING STRONG COUPLING FORMALISM

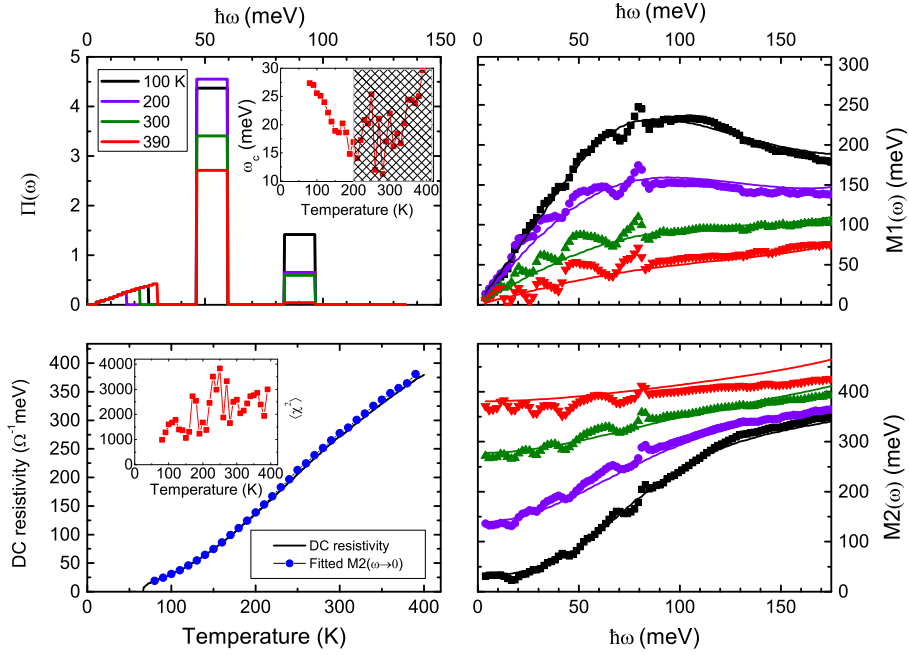


Figure 6.5: Fitting results for model I with varying ω_c and constant α . The change in ω_c as a function of temperature is shown in the inset of top left panel. The non-Fermi liquid temperature range is indicated with the hatched area.

temperature range. The values of Π_1 and Π_2 change as well in order to fit the spectral shapes.

For the model II (fixed ω_c and varying α), both the error and the variation in α are more coherent. A bold feature is observed at around 200 K where the rapidly decreasing slope becomes more stable for temperatures higher than T^{**} (see insets of the top left and bottom left panels in Fig.6.6). This model gives a total lower averaged error than model I. However, the fact that a change in the slope corresponds to change in the density of states, make interpretation of this model somewhat difficult. According to this model, the density of states in the Fermi-liquid seems to be increasing as the temperature decreases. This may be perceived as a contradiction with growing of the pseudo-gap at the density of states as the temperature is decreased.

Both models produce accurate temperature dependence for the DC resistivity. Fig. 6.7 shows the change of the mass renormalization constant λ for the histogram model as well as for models I and II. In all models, λ decreases as a function of increasing temperature which again indicates that the bosonic spectra depends on temperature.

6.4 Fermi-liquid susceptibility: A minimal model

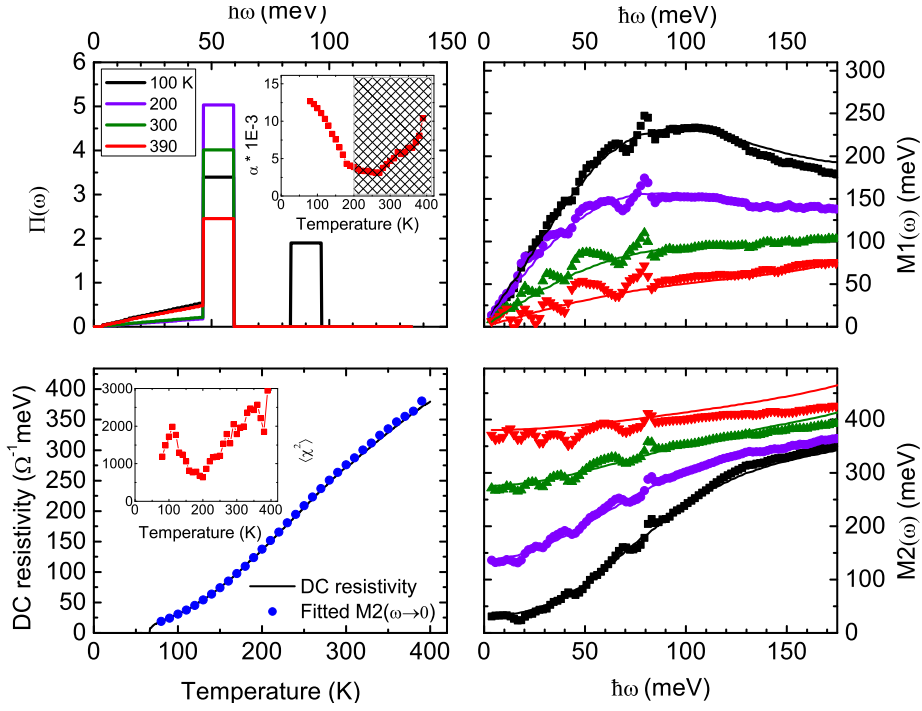


Figure 6.6: Fitting results for model II with varying α . The slope variation is shown in the inset of the top left panel. The non-Fermi liquid area is hatched.

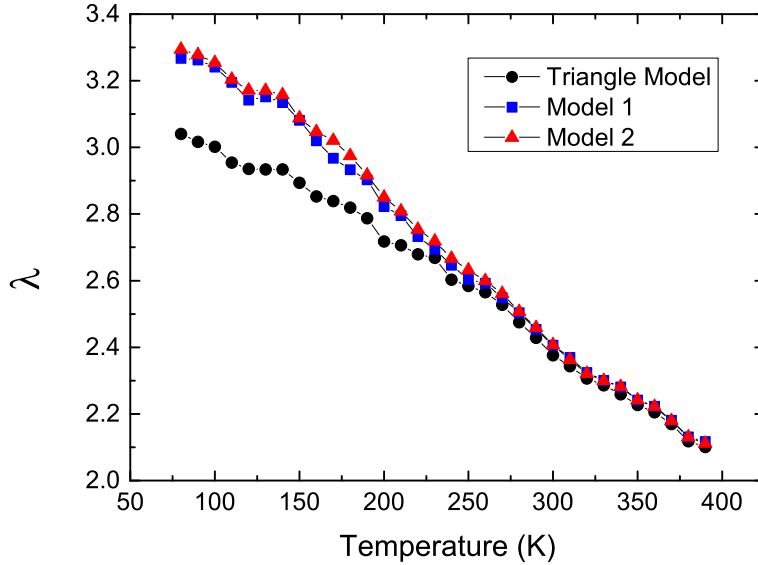


Figure 6.7: The mass renormalization factor λ as a function of temperature for different models. A change of more than 50% is evident throughout the whole temperature range.

6. OPTICAL DATA ANALYSIS USING STRONG COUPLING FORMALISM

6.5 Discussion

We have fitted four different models to the memory function of $\text{HgBa}_2\text{CuO}_{4+\delta}$. In the first model (see Fig. 6.2), the histograms have no limit or dependency on each other or on other parameters. Having around 40 free parameters, the histogram model indeed gives the best fit to the data as compared to other models. The bosonic spectral function gives a peak around 50 meV that gets narrower as a function of increasing temperature. In general, for Fermi physics, the narrowing of features at higher temperatures is somewhat counterintuitive and needs careful thinking. One explanation for this effect is the real change in the physics of the sample as it undergoes at least two phase transitions at T^* and T^{**} (see Fig.4.8). As mentioned earlier in this chapter, the bosonic spectra of a Fermi liquid is proportional to frequency and hence requires some spectral weight at low frequencies (as seen in figure 6.2). By moving to higher temperatures, the low frequency spectral weight is removed as the system will not be a Fermi liquid anymore. Another explanation could be that at higher temperatures, the Fermi distribution function embedded in the kernel $L(\omega, \omega')$ reduces the sensitivity to spectral resolution of $\Pi(\omega)$ and therefore, the fitting algorithm “prefers” to pick up high intensities at one particular frequency rather than a collection of frequencies with lower intensities which leads to the narrow and strong peaks. At low temperatures, there is also a second peak around 80 meV that we believe originates from the strong phonon effect at that frequency.

In the triangle model (see Fig. 6.4), despite the fact that the fit to the optical data is not perfect, the model can reproduce the important features of the optical data and the temperature dependence of the DC resistivity fairly well. An important feature is the relatively constant slope throughout the whole temperature range which is consistent with the Fermi liquid picture.

Models I and II both show that at higher temperatures the low frequency spectral weight of $\Pi(\omega)$ has to be removed either by reducing the cut-off frequency (model I) or by reducing the slope (model II). In both models the peak at around 50 meV grows from 80K to 200K while the low frequency spectral weight reduces. There seems to be a trade-off between these two features in the 80-200K range.

Here, we should remind that a lower sum of squared errors does not necessarily mean a more correct physical picture. All our models are based on assumptions that are not all perfectly justified. For example, we have assumed an isotropic Fermi surface and self energy and the van Hove singularity is not taken into account. The pseudo-

gap phase transition is also ignored in our models. However, for the low frequency and low temperature range where the optical conductivity is dominated by the nodal Fermi liquid response (very large peak in $\sigma(\omega)$) the optical response is much less affected by the issues mentioned above. For energies higher than 100 meV and temperatures higher than the Fermi liquid temperature (T^{**}) the contributions from antinodal regions start to play an important role. Even though it might still be possible to fit optical data in those ranges with our models very well, the resulting bosonic spectra $\Pi(\omega)$ will not be easy to interpret anymore.

6. OPTICAL DATA ANALYSIS USING STRONG COUPLING FORMALISM

Bibliography

- [1] M. Dressel and G. Grüner, *Electrodynamics of Solids Optical Properties of Electrons in Matter*. 2002.
- [2] W. Götze and P. Wölfle, “Homogeneous Dynamical Conductivity of Simple Metals,” *Physical Review B*, vol. 6, pp. 1226–1238, Aug. 1972.
- [3] P. R. Griffiths and C. C. Homes, “Instrumentation for Far-Infrared Spectroscopy,” in *Handbook of Vibrational Spectroscopy*, John Wiley & Sons, Ltd, 2006.
- [4] E. van Heumen, R. Lortz, A. B. Kuzmenko, F. Carbone, D. van der Marel, X. Zhao, G. Yu, Y. Cho, N. Barišić, M. Greven, C. C. Homes, and S. Dordevic, “Optical and thermodynamic properties of the high-temperature superconductor $\text{HgBa}_2\text{CuO}_{4+\delta}$,” *Physical Review B*, vol. 75, pp. 1–10, Feb. 2007.
- [5] Y. Kamihara, T. Watanabe, M. Hirano, and H. Hosono, “Iron-based layered superconductor $\text{La}[\text{O}(1-x)\text{F}(x)]\text{FeAs}$ ($x = 0.05\text{--}0.12$) with $T(c) = 26\text{ K}$,” *Journal of the American Chemical Society*, vol. 130, pp. 3296–7, Mar. 2008.
- [6] Z.-A. Ren, G.-C. Che, X.-L. Dong, J. Yang, W. Lu, W. Yi, X.-L. Shen, Z.-C. Li, L.-L. Sun, F. Zhou, and Z.-X. Zhao, “Superconductivity and phase diagram in iron-based arsenic-oxides $\text{ReFeAsO}_{1-\delta}$ (Re = rare-earth metal) without fluorine doping,” *EPL (Europhysics Letters)*, vol. 83, p. 17002, July 2008.
- [7] Q.-Y. Wang, Z. Li, W.-H. Zhang, Z.-C. Zhang, J.-S. Zhang, W. Li, H. Ding, Y.-B. Ou, P. Deng, K. Chang, J. Wen, C.-L. Song, K. He, J.-F. Jia, S.-H. Ji, Y.-Y. Wang, L.-L. Wang, X. Chen, X.-C. Ma, and Q.-K. Xue, “Interface-Induced

BIBLIOGRAPHY

- High-Temperature Superconductivity in Single Unit-Cell FeSe Films on SrTiO₃,” *Chinese Physics Letters*, vol. 29, p. 037402, Mar. 2012.
- [8] I. I. Mazin, “Superconductivity gets an iron boost.,” *Nature*, vol. 464, pp. 183–6, Mar. 2010.
- [9] S. J. E. Carlsson, F. Levy-Bertrand, C. Marcenat, a. Sulpice, J. Marcus, S. Pairis, T. Klein, M. Núñez Regueiro, G. Garbarino, T. Hansen, V. Nassif, and P. Toulemonde, “Effect of the isoelectronic substitution of Sb for As on the magnetic and structural properties of LaFe(As_{1-x}Sb_x)O,” *Physical Review B*, vol. 84, p. 104523, Sept. 2011.
- [10] a. Drew, F. Pratt, T. Lancaster, S. Blundell, P. Baker, R. Liu, G. Wu, X. Chen, I. Watanabe, V. Malik, a. Dubroka, K. Kim, M. Rössle, and C. Bernhard, “Coexistence of Magnetic Fluctuations and Superconductivity in the Pnictide High Temperature Superconductor SmFeAsO_{1-x}F_x Measured by Muon Spin Rotation,” *Physical Review Letters*, vol. 101, p. 097010, Aug. 2008.
- [11] Y. Laplace, J. Bobroff, F. Rullier-Albenque, D. Colson, and a. Forget, “Atomic coexistence of superconductivity and incommensurate magnetic order in the pnictide Ba(Fe_{1-x}Cox)₂As₂,” *Physical Review B*, vol. 80, p. 140501, Oct. 2009.
- [12] Z. Shermadini, a. Krzton-Maziopa, M. Bendele, R. Khasanov, H. Luetkens, K. Conder, E. Pomjakushina, S. Weyeneth, V. Pomjakushin, O. Bossen, and a. Amato, “Coexistence of Magnetism and Superconductivity in the Iron-Based Compound Cs_{0.8}(FeSe_{0.98})₂,” *Physical Review Letters*, vol. 106, p. 117602, Mar. 2011.
- [13] W. Yang, A. Sorini, C.-C. Chen, B. Moritz, W.-S. Lee, F. Vernay, P. Olalde-Velasco, J. Denlinger, B. Delley, J.-H. Chu, J. Analytis, I. Fisher, Z. Ren, J. Yang, W. Lu, Z. Zhao, J. van den Brink, Z. Hussain, Z.-X. Shen, and T. Devereaux, “Evidence for weak electronic correlations in iron pnictides,” *Physical Review B*, vol. 80, p. 014508, July 2009.
- [14] V. Anisimov, E. Kurmaev, a. Moewes, and I. Izyumov, “Strength of correlations in pnictides and its assessment by theoretical calculations and spectroscopy experiments,” *Physica C: Superconductivity*, vol. 469, pp. 442–447, May 2009.

BIBLIOGRAPHY

- [15] K. Terashima, Y. Sekiba, J. H. Bowen, K. Nakayama, T. Kawahara, T. Sato, P. Richard, Y.-M. Xu, L. J. Li, G. H. Cao, Z.-a. Xu, H. Ding, and T. Takahashi, “Fermi surface nesting induced strong pairing in iron-based superconductors.,” *Proceedings of the National Academy of Sciences of the United States of America*, vol. 106, pp. 7330–3, May 2009.
- [16] H. J. Choi, D. Roundy, H. Sun, M. L. Cohen, and S. G. Louie, “The origin of the anomalous superconducting properties of MgB(2).,” *Nature*, vol. 418, pp. 758–60, Aug. 2002.
- [17] P. L. Alireza, Y. T. C. Ko, J. Gillett, C. M. Petrone, J. M. Cole, G. G. Lonzarich, and S. E. Sebastian, “Superconductivity up to 29 K in SrFe(2)As(2) and BaFe(2)As(2) at high pressures.,” *Journal of physics. Condensed matter : an Institute of Physics journal*, vol. 21, p. 012208, Jan. 2009.
- [18] K. Igawa, H. Okada, H. Takahashi, S. Matsuishi, Y. Kamihara, M. Hirano, H. Hosono, K. Matsubayashi, and Y. Uwatoko, “Pressure-Induced Superconductivity in Iron Pnictide Compound SrFe₂As₂,” *Journal of the Physical Society of Japan*, vol. 78, p. 025001, Feb. 2009.
- [19] C. Chu and B. Lorenz, “High pressure studies on Fe-pnictide superconductors,” *Physica C: Superconductivity*, vol. 469, pp. 385–395, May 2009.
- [20] C. Wang, S. Jiang, Q. Tao, Z. Ren, Y. Li, L. Li, C. Feng, J. Dai, G. Cao, and Z.-a. Xu, “Superconductivity in LaFeAs_{1-x}P_xO: Effect of chemical pressures and bond covalency,” *EPL (Europhysics Letters)*, vol. 86, p. 47002, May 2009.
- [21] S. Kasahara, T. Shibauchi, K. Hashimoto, K. Ikada, S. Tonegawa, R. Okazaki, H. Shishido, H. Ikeda, H. Takeya, K. Hirata, T. Terashima, and Y. Matsuda, “Evolution from non-Fermi- to Fermi-liquid transport via isovalent doping in BaFe₂(As_{1-x}P_x)₂ superconductors,” *Physical Review B*, vol. 81, p. 184519, May 2010.
- [22] P. Canfield, S. Budáček, N. Ni, J. Yan, and a. Kracher, “Decoupling of the superconducting and magnetic/structural phase transitions in electron-doped BaFe₂As₂,” *Physical Review B*, vol. 80, p. 060501, Aug. 2009.

BIBLIOGRAPHY

- [23] J. Gillett, S. D. Das, P. Syers, A. K. T. Ming, J. I. Espeso, C. M. Petrone, and S. E. Sebastian, “Dimensional Tuning of the Magnetic-Structural Transition in $A(\text{Fe}_{1-x}\text{Co}_x)_2\text{As}_2$ ($A=\text{Sr},\text{Ba}$),” vol. 2, p. 4, May 2010.
- [24] P. C. Chu, A. Koshelev, W. Kwok, I. Mazin, U. Welp, and H.-H. Wen, “Superconductivity in iron-pnictides,” *Physica C: Superconductivity*, vol. 469, p. 313, May 2009.
- [25] D. C. Johnston, “The puzzle of high temperature superconductivity in layered iron pnictides and chalcogenides,” *Advances in Physics*, vol. 59, pp. 803–1061, Nov. 2010.
- [26] W. Hu, Q. Zhang, and N. Wang, “Optical and Raman spectroscopy studies on Fe-based superconductors,” *Physica C: Superconductivity*, vol. 469, no. 9-12, pp. 545–558, 2009.
- [27] D. Basov and A. Chubukov, “Manifesto for a higher T_c —Lessons from pnictides and cuprates,” *Arxiv preprint arXiv:1104.1949*, pp. 1–6, 2011.
- [28] X. H. Chen, T. Wu, G. Wu, R. H. Liu, H. Chen, and D. F. Fang, “Superconductivity at 43 K in $\text{SmFeAsO}_{1-x}\text{Fx}$,” *Nature*, vol. 453, pp. 761–2, June 2008.
- [29] C. Senatore, R. Flükiger, M. Cantoni, G. Wu, R. Liu, and X. Chen, “Upper critical fields well above 100 T for the superconductor $\text{SmFeAsO}_{0.85}\text{F}_{0.15}$ with $T_c=46$ K,” *Physical Review B*, vol. 78, p. 054514, Aug. 2008.
- [30] a. Dubroka, K. Kim, M. Rössle, V. Malik, a. Drew, R. Liu, G. Wu, X. Chen, and C. Bernhard, “Superconducting Energy Gap and c-Axis Plasma Frequency of $(\text{Nd},\text{Sm})\text{FeAsO}_{0.82}\text{F}_{0.18}$ Superconductors from Infrared Ellipsometry,” *Physical Review Letters*, vol. 101, p. 097011, Aug. 2008.
- [31] M. Tanatar, N. Ni, C. Martin, R. Gordon, H. Kim, V. Kogan, G. Samolyuk, S. Budáček, P. Canfield, and R. Prozorov, “Anisotropy of the iron pnictide superconductor $\text{Ba}(\text{Fe}_{1-x}\text{Co}_x)_2\text{As}_2$ ($x=0.074$, $T_c=23$ K),” *Physical Review B*, vol. 79, p. 094507, Mar. 2009.
- [32] S.-L. Drechsler, M. Grobosch, K. Koepf, G. Behr, a. Köhler, J. Werner, a. Kondrat, N. Leps, C. Hess, R. Klingeler, R. Schuster, B. Büchner, and

BIBLIOGRAPHY

- M. Knupfer, “Optical Study of $\text{LaO}_{0.9}\text{F}_{0.1}\text{FeAs}$: Evidence for a Weakly Coupled Superconducting State,” *Physical Review Letters*, vol. 101, p. 257004, Dec. 2008.
- [33] G. F. Chen, Z. Li, D. Wu, G. Li, W. Z. Hu, J. Dong, P. Zheng, J. L. Luo, and N. L. Wang, “Superconductivity at 41 K and Its Competition with Spin-Density-Wave Instability in Layered $\text{CeO}_{1-x}\text{F}_x\text{FeAs}$,” *Physical Review Letters*, vol. 100, p. 247002, June 2008.
- [34] D. Tanner and T. Timusk, “For a review see D. B. Tanner and T. Timusk: Physical Properties of High Temperature Superconductors III, ed. D. M. Ginsberg (World Scientific, Singapore, 1992).,” 1992.
- [35] E. van Heumen, Y. Huang, S. de Jong, A. B. Kuzmenko, M. S. Golden, and D. van der Marel, “Optical properties of $\text{BaFe}_{2-x}\text{Co}_x\text{As}_2$,” *EPL (Europhysics Letters)*, vol. 90, p. 37005, May 2010.
- [36] a. Kuzmenko, N. Tombros, H. Molegraaf, M. Grüninger, D. van der Marel, and S. Uchida, “c-Axis Optical Sum Rule and a Possible New Collective Mode in $\text{La}_{2-x}\text{Sr}_x\text{CuO}_4$,” *Physical Review Letters*, vol. 91, p. 037004, July 2003.
- [37] A. Kuzmenko, F. Mena, H. Molegraaf, D. van der Marel, B. Gorshunov, M. Dressel, I. Mazin, J. Kortus, O. Dolgov, T. Muranaka, and J. Akimitsu, “Manifestation of multiband optical properties of MgB_2 ,” *Solid State Communications*, vol. 121, pp. 479–484, Mar. 2002.
- [38] D. Stroud, “Generalized effective-medium approach to the conductivity of an inhomogeneous material,” *Physical Review B*, vol. 12, pp. 3368–3373, Oct. 1975.
- [39] S. E. Sebastian, J. Gillett, N. Harrison, P. H. C. Lau, D. J. Singh, C. H. Mielke, and G. G. Lonzarich, “Quantum oscillations in the parent magnetic phase of an iron arsenide high temperature superconductor,” *Journal of Physics: Condensed Matter*, vol. 20, p. 422203, Oct. 2008.
- [40] B. Cheng, Z. Chen, C. Zhang, R. Ruan, T. Dong, B. Hu, W. Guo, S. Miao, P. Zheng, J. Luo, G. Xu, P. Dai, and N. Wang, “Three-dimensionality of band structure and a large residual quasiparticle population in $\text{Ba}_{0.67}\text{K}_{0.33}\text{Fe}_2\text{As}_2$ as revealed by c-axis polarized optical measurements,” *Physical Review B*, vol. 83, Apr. 2011.

BIBLIOGRAPHY

- [41] A. B. Kuzmenko, "ReFFIT (software to fit optical spectra)," 2009.
- [42] E. van Heumen, W. Meevasana, A. B. Kuzmenko, H. Eisaki, and D. van der Marel, "Doping-dependent optical properties of Bi2201," *New Journal of Physics*, vol. 11, p. 055067, May 2009.
- [43] S. Li, C. de la Cruz, Q. Huang, Y. Chen, J. W. Lynn, J. Hu, Y.-L. Huang, F.-C. Hsu, K.-W. Yeh, M.-K. Wu, and P. Dai, "First-order magnetic and structural phase transitions in $\text{Fe}_{1+y}\text{Se}_x\text{Te}_{1-x}$," *Physical Review B*, vol. 79, Feb. 2009.
- [44] W. Bao, Y. Qiu, Q. Huang, M. A. Green, P. Zajdel, M. R. Fitzsimmons, M. Zhernenkov, S. Chang, M. Fang, B. Qian, E. K. Vehstedt, J. Yang, H. M. Pham, L. Spinu, and Z. Q. Mao, "Tunable $(\delta\pi, \delta\pi)$ -Type Antiferromagnetic Order in α -Fe(Te,Se) Superconductors," *Physical Review Letters*, vol. 102, June 2009.
- [45] G. F. Chen, Z. G. Chen, J. Dong, W. Z. Hu, G. Li, X. D. Zhang, P. Zheng, J. L. Luo, and N. L. Wang, "Electronic properties of single-crystalline $\text{Fe}_{1.05}\text{Te}$ and $\text{Fe}_{1.03}\text{Se}_{0.30}\text{Te}_{0.70}$," *Physical Review B*, vol. 79, Apr. 2009.
- [46] Q. Huang, Y. Qiu, W. Bao, M. A. Green, J. W. Lynn, Y. C. Gasparovic, T. Wu, G. Wu, and X. H. Chen, "Neutron-Diffraction Measurements of Magnetic Order and a Structural Transition in the Parent BaFe_2As_2 Compound of FeAs-Based High-Temperature Superconductors," *Physical Review Letters*, vol. 101, p. 257003, Dec. 2008.
- [47] F.-C. Hsu, J.-Y. Luo, K.-W. Yeh, T.-K. Chen, T.-W. Huang, P. M. Wu, Y.-C. Lee, Y.-L. Huang, Y.-Y. Chu, D.-C. Yan, and M.-K. Wu, "Superconductivity in the PbO-type structure α -FeSe," *Proceedings of the National Academy of Sciences of the United States of America*, vol. 105, pp. 14262–4, Sept. 2008.
- [48] M. Rotter, M. Tegel, and D. Johrendt, "Superconductivity at 38 K in the Iron Arsenide $(\text{Ba}_{1-x}\text{K}_x)\text{Fe}_2\text{As}_2$," *Physical Review Letters*, vol. 101, Sept. 2008.
- [49] Y. Han, W. Y. Li, L. X. Cao, X. Y. Wang, B. Xu, B. R. Zhao, Y. Q. Guo, and J. L. Yang, "Superconductivity in Iron Telluride Thin Films under Tensile Stress," *Physical Review Letters*, vol. 104, Jan. 2010.

BIBLIOGRAPHY

- [50] A. Subedi, L. Zhang, D. Singh, and M. Du, “Density functional study of FeS, FeSe, and FeTe: Electronic structure, magnetism, phonons, and superconductivity,” *Physical Review B*, vol. 78, Oct. 2008.
- [51] D. J. Singh and M.-H. Du, “Density Functional Study of $\text{LaFeAsO}_{1-x}\text{F}_x$: A Low Carrier Density Superconductor Near Itinerant Magnetism,” *Physical Review Letters*, vol. 100, p. 237003, June 2008.
- [52] I. I. Mazin, D. J. Singh, M. D. Johannes, and M. H. Du, “Unconventional Superconductivity with a Sign Reversal in the Order Parameter of $\text{LaFeAsO}_{1-x}\text{F}_x$,” *Physical Review Letters*, vol. 101, July 2008.
- [53] M. Yi, D. Lu, J. Analytis, J.-H. Chu, S.-K. Mo, R.-H. He, R. Moore, X. Zhou, G. Chen, J. Luo, N. Wang, Z. Hussain, D. Singh, I. Fisher, and Z.-X. Shen, “Electronic structure of the BaFe_2As_2 family of iron-pnictide superconductors,” *Physical Review B*, vol. 80, July 2009.
- [54] Y. Xia, D. Qian, L. Wray, D. Hsieh, G. F. Chen, J. L. Luo, N. L. Wang, and M. Z. Hasan, “Fermi Surface Topology and Low-Lying Quasiparticle Dynamics of Parent $\text{Fe}_{1+x}\text{Te/Se}$ Superconductor,” *Physical Review Letters*, vol. 103, July 2009.
- [55] J. Hancock, S. Mirzaei, J. Gillett, S. Sebastian, J. Teyssier, R. Viennois, E. Giannini, and D. van der Marel, “Strong coupling to magnetic fluctuations in the charge dynamics of iron-based superconductors,” *Physical Review B*, vol. 82, July 2010.
- [56] A. Jesche, N. Caroca-Canales, H. Rosner, H. Borrmann, A. Ormeci, D. Kasinathan, H. Klauss, H. Luetkens, R. Khasanov, A. Amato, A. Hoser, K. Kaneko, C. Krellner, and C. Geibel, “Strong coupling between magnetic and structural order parameters in SrFe_2As_2 ,” *Physical Review B*, vol. 78, p. 180504, Nov. 2008.
- [57] Y. Zhang, F. Chen, C. He, L. Yang, B. Xie, Y. Xie, X. Chen, M. Fang, M. Arita, K. Shimada, H. Namatame, M. Taniguchi, J. Hu, and D. Feng, “Strong correlations and spin-density-wave phase induced by a massive spectral weight redistribution in $\alpha\text{-Fe}_{1.06}\text{Te}$,” *Physical Review B*, vol. 82, p. 165113, Oct. 2010.

BIBLIOGRAPHY

- [58] H. V. Löhneysen and P. Wölfle, “Fermi-liquid instabilities at magnetic quantum phase transitions,” *Reviews of Modern Physics*, vol. 79, pp. 1015–1075, Aug. 2007.
- [59] P. Gegenwart, Q. Si, and F. Steglich, “Quantum criticality in heavy-fermion metals,” *Nature Physics*, vol. 4, pp. 186–197, Mar. 2008.
- [60] Q. Si and F. Steglich, “Heavy fermions and quantum phase transitions.,” *Science (New York, N.Y.)*, vol. 329, pp. 1161–6, Sept. 2010.
- [61] K. Hashimoto, Y. Mizukami, R. Katsumata, H. Shishido, M. Yamashita, H. Ikeda, Y. Matsuda, J. a. Schlueter, J. D. Fletcher, A. Carrington, D. Gnida, D. Kaczorowski, and T. Shibauchi, “Anomalous superfluid density in quantum critical superconductors.,” *Proceedings of the National Academy of Sciences of the United States of America*, vol. 110, pp. 3293–3297, Feb. 2013.
- [62] T. Valla, “Evidence for Quantum Critical Behavior in the Optimally Doped Cuprate $\text{Bi}_2\text{Sr}_2\text{CaCu}_2\text{O}_8+$,” *Science*, vol. 285, pp. 2110–2113, Sept. 1999.
- [63] J. Tallon and J. Loram, “The doping dependence of T^* — what is the real high- T_c phase diagram?,” *Physica C: Superconductivity*, vol. 349, pp. 53–68, Jan. 2001.
- [64] D. van der Marel, H. J. A. Molegraaf, J. Zaanen, Z. Nussinov, F. Carbone, A. Damascelli, H. Eisaki, M. Greven, P. H. Kes, and M. Li, “Quantum critical behaviour in a high- $T(c)$ superconductor.,” *Nature*, vol. 425, pp. 271–4, Sept. 2003.
- [65] M. Gooch, B. Lv, B. Lorenz, A. Guloy, and C.-W. Chu, “Evidence of quantum criticality in the phase diagram of $\text{K}_x\text{Sr}_{1-x}\text{Fe}_2\text{As}_2$ from measurements of transport and thermoelectricity,” *Physical Review B*, vol. 79, p. 104504, Mar. 2009.
- [66] E. Abrahams and Q. Si, “Quantum criticality in the iron pnictides and chalcogenides.,” *Journal of physics. Condensed matter : an Institute of Physics journal*, vol. 23, p. 223201, June 2011.
- [67] T. Shibauchi, A. Carrington, and Y. Matsuda, “Quantum critical point lying beneath the superconducting dome in iron-pnictides,” pp. 1–15, 2013.

BIBLIOGRAPHY

- [68] C. Varma, Z. Nussinov, and W. van Saarloos, “Singular or non-Fermi liquids,” *Physics Reports*, vol. 361, pp. 267–417, May 2002.
- [69] Q. Si, S. Rabello, K. Ingersent, and J. L. Smith, “Locally critical quantum phase transitions in strongly correlated metals.,” *Nature*, vol. 413, pp. 804–8, Oct. 2001.
- [70] S. Sachdev, *Quantum Phase Transitions*. Cambridge University Press, 2 ed., 2011.
- [71] T. Senthil, A. Vishwanath, L. Balents, S. Sachdev, and M. P. a. Fisher, “Deconfined quantum critical points.,” *Science (New York, N.Y.)*, vol. 303, pp. 1490–4, Mar. 2004.
- [72] Z. Ren, Q. Tao, S. Jiang, C. Feng, C. Wang, J. Dai, G. Cao, and Z. Xu, “Superconductivity Induced by Phosphorus Doping and Its Coexistence with Ferromagnetism in $\text{EuFe}_2(\text{As}_{0.7}\text{P}_{0.3})_2$,” *Physical Review Letters*, vol. 102, p. 137002, Apr. 2009.
- [73] S. Jiang, H. Xing, G. Xuan, C. Wang, Z. Ren, C. Feng, J. Dai, Z. Xu, and G. Cao, “Superconductivity up to 30 K in the vicinity of the quantum critical point in $\text{BaFe}_2(\text{As}_{1-x}\text{P}_x)_2$,” *Journal of physics. Condensed matter : an Institute of Physics journal*, vol. 21, p. 382203, Sept. 2009.
- [74] S. Sharma, a. Bharathi, S. Chandra, V. R. Reddy, S. Paulraj, a. T. Satya, V. S. Sastry, A. Gupta, and C. S. Sundar, “Superconductivity in Ru-substituted polycrystalline $\text{BaFe}_{2-x}\text{Ru}_x\text{As}_2$,” *Physical Review B*, vol. 81, p. 174512, May 2010.
- [75] F. Rullier-Albenque, D. Colson, a. Forget, P. Thuéry, and S. Poissonnet, “Hole and electron contributions to the transport properties of $\text{Ba}(\text{Fe}_{1-x}\text{Ru}_x)_2\text{As}_2$ single crystals,” *Physical Review B*, vol. 81, p. 224503, June 2010.
- [76] a. Thaler, N. Ni, a. Kracher, J. Q. Yan, S. L. Budářko, and P. C. Canfield, “Physical and magnetic properties of $\text{Ba}(\text{Fe}_{1-x}\text{Ru}_x)_2\text{As}_2$ single crystals,” *Physical Review B*, vol. 82, p. 014534, July 2010.

BIBLIOGRAPHY

- [77] M. Rotter, C. Hieke, and D. Johrendt, “Different response of the crystal structure to isoelectronic doping in $\text{BaFe}_{2}(\text{As}_{1-x}\text{P}_{x})_{2}$ and $(\text{Ba}_{1-x}\text{Sr}_{x})\text{Fe}_{2}\text{As}_{2}$,” *Physical Review B*, vol. 82, p. 014513, July 2010.
- [78] H. Luo, R. Zhang, M. Laver, Z. Yamani, M. Wang, X. Lu, M. Wang, Y. Chen, S. Li, S. Chang, J. W. Lynn, and P. Dai, “Coexistence and Competition of the Short-Range Incommensurate Antiferromagnetic Order with the Superconducting State of $\text{BaFe}_{2-x}\text{Ni}_{x}\text{As}_{2}$,” *Physical Review Letters*, vol. 108, p. 247002, June 2012.
- [79] W. Malaeb, T. Shimojima, Y. Ishida, K. Okazaki, Y. Ota, K. Ohgushi, K. Kihou, T. Saito, C. H. Lee, S. Ishida, M. Nakajima, S. Uchida, H. Fukazawa, Y. Kohori, a. Iyo, H. Eisaki, C.-T. Chen, S. Watanabe, H. Ikeda, and S. Shin, “Abrupt change in the energy gap of superconducting $\text{Ba}_{1-x}\text{K}_{x}\text{Fe}_{2}\text{As}_{2}$ single crystals with hole doping,” *Physical Review B*, vol. 86, p. 165117, Oct. 2012.
- [80] K. Hashimoto, T. Shibauchi, S. Kasahara, K. Ikada, S. Tonegawa, T. Kato, R. Okazaki, C. J. van der Beek, M. Konczykowski, H. Takeya, K. Hirata, T. Terashima, and Y. Matsuda, “Microwave Surface-Impedance Measurements of the Magnetic Penetration Depth in Single Crystal $\text{Ba}_{1-x}\text{K}_{x}\text{Fe}_{2}\text{As}_{2}$ Superconductors: Evidence for a Disorder-Dependent Superfluid Density,” *Physical Review Letters*, vol. 102, p. 207001, May 2009.
- [81] A. Akrap, J. J. Tu, L. J. Li, G. H. Cao, Z. A. Xu, and C. C. Homes, “Infrared phonon anomaly in $\text{BaFe}_{2}\text{As}_{2}$,” *Physical Review B*, vol. 80, p. 180502, Nov. 2009.
- [82] X. Zhao, G. Yu, Y. Cho, G. Chabot-Couture, N. Barišić, P. Bourges, N. Kaneko, Y. Li, L. Lu, E. M. Motoyama, O. P. Vajk, and M. Greven, “Crystal Growth and Characterization of the Model High-Temperature Superconductor $\text{HgBa}_{2}\text{CuO}_{4+\delta}$,” *Advanced Materials*, vol. 18, pp. 3243–3247, Dec. 2006.
- [83] N. Barišić, Y. Li, X. Zhao, Y.-C. Cho, G. Chabot-Couture, G. Yu, and M. Greven, “Demonstrating the model nature of the high-temperature superconductor $\text{HgBa}_{2}\text{CuO}_{4+\delta}$,” *Physical Review B*, vol. 78, pp. 1–7, Aug. 2008.

BIBLIOGRAPHY

- [84] M. Norman, A. Chubukov, E. van Heumen, A. B. Kuzmenko, and D. van der Marel, "Optical integral in the cuprates and the question of sum-rule violation," *Physical Review B*, vol. 76, Dec. 2007.
- [85] P. Allen, "Electron-Phonon Effects in the Infrared Properties of Metals," *Physical Review B*, vol. 3, pp. 305–320, Jan. 1971.
- [86] E. van Heumen, E. Muhlethaler, A. B. Kuzmenko, H. Eisaki, W. Meevasana, M. Greven, and D. van der Marel, "Optical determination of the relation between the electron-boson coupling function and the critical temperature in high- T_c cuprates," *Physical Review B*, vol. 79, pp. 1–7, May 2009.
- [87] E. Pavarini, I. Dasgupta, T. Saha-Dasgupta, O. Jepsen, and O. Andersen, "Band-Structure Trend in Hole-Doped Cuprates and Correlation with T_c max," *Physical Review Letters*, vol. 87, pp. 1–10, July 2001.
- [88] M. Holcomb, J. Collman, and W. Little, "Optical Evidence of an Electronic Contribution to the Pairing Interaction in Superconducting $Tl_2Ba_2Ca_2Cu_3O_{10}$," *Physical Review Letters*, vol. 73, pp. 2360–2363, Oct. 1994.
- [89] M. Rübhausen, A. Gozar, M. V. Klein, P. Guptasarma, and D. G. Hinks, "Superconductivity-induced optical changes for energies of 100Δ in the cuprates," *Physical Review B*, vol. 63, p. 224514, May 2001.
- [90] H. J. a. Molegraaf, C. Presura, D. van Der Marel, P. H. Kes, and M. Li, "Superconductivity-induced transfer of in-plane spectral weight in $Bi_2Sr_2CaCu_2O_{8+\delta}$," *Science (New York, N.Y.)*, vol. 295, pp. 2239–41, Mar. 2002.
- [91] a. V. Boris, N. N. Kovaleva, O. V. Dolgov, T. Holden, C. T. Lin, B. Keimer, and C. Bernhard, "In-plane spectral weight shift of charge carriers in $YBa_2Cu_3O_{6.9}$," *Science (New York, N.Y.)*, vol. 304, pp. 708–10, Apr. 2004.
- [92] a. Santander-Syro, R. Lobo, N. Bontemps, W. Lopera, D. Giratá, Z. Konstantinovic, Z. Li, and H. Raffy, "In-plane electrodynamics of the superconductivity in $Bi_2Sr_2CaCu_2O_{8+\delta}$: Energy scales and spectral weight distribution," *Physical Review B*, vol. 70, p. 134504, Oct. 2004.

BIBLIOGRAPHY

- [93] F. Marsiglio, “Optical Sum Rule Anomalies in the High-T_c Cuprates,” *Journal of Superconductivity and Novel Magnetism*, vol. 22, pp. 269–273, Jan. 2009.
- [94] C. Giannetti, F. Cilento, S. Dal Conte, G. Coslovich, G. Ferrini, H. J. A. Molegraaf, M. Raichle, R. Liang, H. Eisaki, M. Greven, Others, A. Damascelli, D. van der Marel, and F. Parmigiani, “Revealing the high-energy electronic excitations underlying the onset of high-temperature superconductivity in cuprates.,” *Nature communications*, vol. 2, p. 353, Jan. 2011.
- [95] J. M. WHEATLEY, T. C. HSU, and P. W. ANDERSON, “Interlayer effects in high-T_c superconductors,” *Nature*, vol. 333, pp. 121–121, May 1988.
- [96] J. Hirsch and F. Marsiglio, “Hole superconductivity: Review and some new results,” *Physica C: Superconductivity*, vol. 162-164, pp. 591–598, Dec. 1989.
- [97] F. Marsiglio and J. Hirsch, “Hole superconductivity and the high-T_c oxides,” *Physical Review B*, vol. 41, pp. 6435–6456, Apr. 1990.
- [98] J. Hirsch, “Apparent violation of the conductivity sum rule in certain superconductors,” *Physica C: Superconductivity*, vol. 199, pp. 305–310, Sept. 1992.
- [99] J. Hirsch, “Superconductors that change color when they become superconducting,” *Physica C: Superconductivity*, vol. 201, pp. 347–361, Oct. 1992.
- [100] N. Barišić, Y. Li, G. Yu, X. Zhao, M. Dressel, A. Smontara, and M. Greven, “Universal plaquette resistance of the cuprate superconductors,” pp. 1–33, July 2012.
- [101] a. Santander-Syro, R. Lobo, N. Bontemps, Z. Konstantinovic, Z. Li, and H. Raffy, “Absence of a Loss of In-Plane Infrared Spectral Weight in the Pseudogap Regime of Bi₂Sr₂CaCu₂O_{8+δ},” *Physical Review Letters*, vol. 88, pp. 2–5, Feb. 2002.
- [102] Y. Li, G. Yu, M. K. Chan, V. Balédent, Y. Li, N. Barišić, X. Zhao, K. Hradil, R. a. Mole, Y. Sidis, P. Steffens, P. Bourges, and M. Greven, “Two Ising-like magnetic excitations in a single-layer cuprate superconductor,” *Nature Physics*, vol. 8, pp. 404–410, Mar. 2012.
- [103] C. Varma, “High-temperature superconductivity: Mind the pseudogap.,” *Nature*, vol. 468, pp. 184–5, Nov. 2010.

BIBLIOGRAPHY

- [104] J. Bardeen, L. Cooper, and J. Schrieffer, “Microscopic Theory of Superconductivity,” *Physical Review*, vol. 106, pp. 162–164, Apr. 1957.
- [105] C. Proust, E. Boaknin, R. Hill, L. Taillefer, and a. Mackenzie, “Heat Transport in a Strongly Overdoped Cuprate: Fermi Liquid and a Pure d-Wave BCS Superconductor,” *Physical Review Letters*, vol. 89, p. 147003, Sept. 2002.
- [106] B. Vignolle, a. Carrington, R. a. Cooper, M. M. J. French, a. P. Mackenzie, C. Jaudet, D. Vignolles, C. Proust, and N. E. Hussey, “Quantum oscillations in an overdoped high- T_c superconductor,” *Nature*, vol. 455, pp. 952–955, Oct. 2008.
- [107] M. Platé, J. Mottershead, I. Elfimov, D. Peets, R. Liang, D. Bonn, W. Hardy, S. Chiuzbaian, M. Falub, M. Shi, L. Patthey, and a. Damascelli, “Fermi Surface and Quasiparticle Excitations of Overdoped $Tl_2Ba_2CuO_{6+\delta}$,” *Physical Review Letters*, vol. 95, p. 077001, Aug. 2005.
- [108] T. Valla, A. Fedorov, P. Johnson, Q. Li, G. Gu, and N. Koshizuka, “Temperature dependent scattering rates at the fermi surface of optimally doped $Bi(2)Sr(2)CaCu(2)O(8+\delta)$,” *Physical review letters*, vol. 85, pp. 828–31, July 2000.
- [109] R. W. Hill, C. Proust, L. Taillefer, P. Fournier, and R. L. Greene, “Breakdown of Fermi-liquid theory in a copper-oxide superconductor,” *Nature*, vol. 414, pp. 711–5, Dec. 2001.
- [110] H. Takagi, B. Batlogg, H. Kao, J. Kwo, R. Cava, J. Krajewski, and W. Peck, “Systematic evolution of temperature-dependent resistivity in $La_{2-x}Sr_xCuO_4$,” *Physical Review Letters*, vol. 69, pp. 2975–2978, Nov. 1992.
- [111] C. Renner, B. Revaz, J.-Y. Genoud, K. Kadowaki, and O. Fischer, “Pseudogap Precursor of the Superconducting Gap in Under- and Overdoped $Bi_2Sr_2CaCu_2O_{8+\delta}$,” *Physical Review Letters*, vol. 80, pp. 149–152, Jan. 1998.
- [112] H. Ding, T. Yokoya, J. C. Campuzano, T. Takahashi, M. Randeria, M. R. Norman, T. Mochiku, K. Kadowaki, and J. Giapintzakis, “Spectroscopic evidence

BIBLIOGRAPHY

- for a pseudogap in the normal state of underdoped high-Tc superconductors,” *Nature*, vol. 382, pp. 51–54, July 1996.
- [113] Y. Onose, Y. Taguchi, K. Ishizaka, and Y. Tokura, “Charge dynamics in underdoped Nd_{2-x}Ce_xCuO₄: Pseudogap and related phenomena,” *Physical Review B*, vol. 69, pp. 1–13, Jan. 2004.
- [114] Y. Ando, S. Komiya, K. Segawa, S. Ono, and Y. Kurita, “Electronic Phase Diagram of High-Tc Cuprate Superconductors from a Mapping of the In-Plane Resistivity Curvature,” *Physical Review Letters*, vol. 93, pp. 1–4, Dec. 2004.
- [115] N. Doiron-Leyraud, C. Proust, D. LeBoeuf, J. Levallois, J.-B. Bonnemaïson, R. Liang, D. A. Bonn, W. N. Hardy, and L. Taillefer, “Quantum oscillations and the Fermi surface in an underdoped high-Tc superconductor,” *Nature*, vol. 447, pp. 565–8, May 2007.
- [116] S. I. Mirzaei, D. Stricker, J. N. Hancock, C. Berthod, A. Georges, E. van Heumen, M. K. Chan, X. Zhao, Y. Li, M. Greven, N. Barisic, and D. van der Marel, “Spectroscopic evidence for Fermi liquid-like energy and temperature dependence of the relaxation rate in the pseudogap phase of the cuprates,” *Proceedings of the National Academy of Sciences of the United States of America*, vol. 110, pp. 5774–8, Apr. 2013.
- [117] J. Hwang, J. Yang, T. Timusk, S. Sharapov, J. Carbotte, D. A. Bonn, R. Liang, and W. N. Hardy, “a-axis optical conductivity of detwinned ortho-II YBa₂Cu₃O_{6.50},” *Physical Review B*, vol. 73, pp. 1–12, Jan. 2006.
- [118] H. Eisaki, N. Kaneko, D. Feng, a. Damascelli, P. Mang, K. Shen, Z.-X. Shen, and M. Greven, “Effect of chemical inhomogeneity in bismuth-based copper oxide superconductors,” *Physical Review B*, vol. 69, p. 064512, Feb. 2004.
- [119] E. Gull, M. Ferrero, O. Parcollet, a. Georges, and a. Millis, “Momentum-space anisotropy and pseudogaps: A comparative cluster dynamical mean-field analysis of the doping-driven metal-insulator transition in the two-dimensional Hubbard model,” *Physical Review B*, vol. 82, p. 155101, Oct. 2010.
- [120] B. Shastri, “Extremely Correlated Fermi Liquids,” *Physical Review Letters*, vol. 107, pp. 1–5, July 2011.

BIBLIOGRAPHY

- [121] D. Bergeron, V. Hankevych, B. Kyung, and A.-M. Tremblay, “Optical and dc conductivity of the two-dimensional Hubbard model in the pseudogap regime and across the antiferromagnetic quantum critical point including vertex corrections,” *Physical Review B*, vol. 84, pp. 1–35, Aug. 2011.
- [122] P. Anderson, “Hidden Fermi liquid: The secret of high-Tc cuprates,” *Physical Review B*, vol. 78, pp. 6–11, Nov. 2008.
- [123] L. Ioffe and A. Millis, “Zone-diagonal-dominated transport in high-Tc cuprates,” *Physical Review B*, vol. 58, pp. 11631–11637, Nov. 1998.
- [124] B. P. Stojkovic and D. Pines, “Theory of the longitudinal and Hall conductivities of the cuprate superconductors,” *Physical Review B*, vol. 55, pp. 8576–8595, Apr. 1997.
- [125] D. Basov, R. Averitt, D. van der Marel, M. Dressel, and K. Haule, “Electrodynamics of correlated electron materials,” *Reviews of Modern Physics*, vol. 83, pp. 471–542, June 2011.
- [126] M. Dressel, “Quantum criticality in organic conductors? Fermi liquid versus non-Fermi-liquid behaviour,” *Journal of physics. Condensed matter : an Institute of Physics journal*, vol. 23, p. 293201, July 2011.
- [127] U. Nagel, T. Uleksin, T. Rõõm, R. P. S. M. Lobo, P. Lejay, C. C. Homes, J. Hall, A. W. Kinross, S. Purdy, T. J. Williams, G. M. Luke, and T. Timusk, “The normal state of URu₂Si₂: spectroscopic evidence for an anomalous Fermi liquid,” p. 5, July 2011.
- [128] D. L. Maslov and A. V. Chubukov, “First-Matsubara-frequency rule in a Fermi liquid. Part II: Optical conductivity and comparison to experiment,” p. 18, Aug. 2012.
- [129] V. Barzykin and D. Pines, “Universal behaviour and the two-component character of magnetically underdoped cuprate superconductors,” *Advances in Physics*, vol. 58, pp. 1–65, Jan. 2009.
- [130] A. Chubukov and D. Maslov, “Singular corrections to the Fermi-liquid theory,” *Physical Review B*, vol. 69, pp. 2–5, Mar. 2004.

BIBLIOGRAPHY

- [131] A. Migdal, “Interaction between electrons and lattice vibrations in a normal metal,” *Sov. Phys. JETP*, vol. 7, no. 6, pp. 996–1001, 1958.
- [132] S. Dordevic, C. Homes, J. Tu, T. Valla, M. Strongin, P. Johnson, G. Gu, and D. Basov, “Extracting the electron-boson spectral function $\alpha^2F(\omega)$ from infrared and photoemission data using inverse theory,” *Physical Review B*, vol. 71, p. 104529, Mar. 2005.